MOLECULAR DYNAMICS SIMULATIONS OF SHOCK-INDUCED PORE COLLAPSE IN SINGLE CRYSTAL β-HMX

A Thesis
presented to
the Faculty of the Graduate School
at the University of Missouri-Columbia

In Partial Fulfillment
of the Requirements for the Degree
Master of Science

---

by
DILKI PERERA
Prof. Tommy Sewell, Thesis Supervisor
DECEMBER 2023

The undersigned, appointed by the dean of the Graduate School, have examined the thesis entitled

MOLECULAR DYNAMICS SIMULATIONS OF SHOCK-INDUCED PORE COLLAPSE IN SINGLE CRYSTAL β-HMX

presented by Dilki Perera,
a candidate for the degree of Master of Science in Chemistry,
and hereby certify that, in their opinion, it is worthy of acceptance.

Professor Tommy Sewell

Professor Bernadette Broderick

Professor Michael Greenlief

Professor Matthias Young

To

My mother, Lalitha Karunaratne

My father, Abeykumara Perera

&

My husband, Prasan Anupama

ACKNOWLEDGEMENTS

Throughout this journey there are many people and many opportunities that had a significant impact in both my academics and in life, for which I'm eternally grateful. I extend my acknowledgement here for the people that were with me through my graduate studies at Mizzou.

First and foremost, I would like to extend my gratitude for my mentor, Prof. Thomas (Tommy) Sewell, for the opportunity and introducing this entire new field of study to me. Since day one and until this day, his passion towards 'quality science' motivates me to work hard. His patience and guidance has shaped me to be a better scientist, while his attention to details has immensely supported to produce quality work. His discipline and dedication to do the best, continue to surprise me to date. I consider myself to be fortunate to be mentored by such a person and will be grateful for all my life for this amazing opportunity.

I am forever in debt to Dr. Puhan Zhao for teaching me the basics of coding and laying foundation for my work presented here. She has always been there to support me through my graduate studies. She is extremely patient through all my trivial questions and guide me to find the solution on my own. This exact quality of hers make me feel like she was my second mentor through this journey. I like to thank Dr. Andrey Pereverzev for insightful discussions and all the important questions he never fails to ask. Also, I extend my gratitude to Win Grace as she always welcome me with a big smile and lend an ear to all my problems.

I thank Jerry and Holly for all the administrative help they provided throughout. I acknowledge the RCSS team here at Mizzou for their support with the computers. Especially Asif and Predrag who were always an email away for help.

I would like to thank the research team from University of Iowa lead by Prof. Udaykumar for the opportunity of collaboration during this work.

I thank my thesis committee Dr. Greenlief, Dr. Matthias Young and Dr. Bernedette Broderick for the time from their busy schedules to evaluate my work.

I'm thankful to Ethan, for tolerating me at Schlundt 3^{rd} floor and specially for all the shared lunch times and chit chats that were essential to keep me sane moving forward.

I would also like to thank all my Sri Lankan friends here at Mizzou for helping me survive graduate school and for making the graduate life a memorable one. You guys were the family that I had here and I'm grateful for all the memories we made together.

Most importantly, I'm grateful for my parents as they are the foundation for who I am today. All my success in life is because of their constant belief on me to achieve great things, and all their sacrifices towards my education. I'm thankful to my brother who is always on my side for anything I do and constantly make an effort to understand what I do to provide support when I need it. Most importantly, I'm eternally grateful for my husband for all his sacrifices to be by my side patiently while I continue with my studies. Thank you for being a part of this journey and for the support you provide.

Finally, I express my gratitude to Prof. Sewell for supporting me as a research assistant through his grants by a U.S. Air Force Office of Scientific Research (AFOSR) MURI grant; PI Sewell, federal award FA9550-19-1-0318 and computer resources purchased via an AFOSR-DMI DURIP equipment grant (FA9559-20-1-0205).

TABLE OF CONTENTS

LIST OF TABLES

LIST OF ILLUSTRATIONS

MOLECULAR DYNAMICS SIMULATIONS OF SHOCK-INDUCED PORE COLLAPSE IN SINGLE CRYSTAL β-HMX

Dilki Perera

Prof. Tommy Sewell, Thesis Supervisor

ABSTRACT

This thesis presents all-atom classical molecular dynamics (MD) simulations of shock-wave passage across a pore-type defect in single-crystal β-1,3,5,7-tetranitro-1,3,5,7-tetraocane (β-HMX). The purpose of this study is to understand the anisotropic thermo-mechanical response of HMX during and following shock-induced pore collapse. This thesis is comprised of three studies. The first study is focused on understanding the sensitivity of overall results to: sample thickness in a quasi-2D cell, transverse orientation of the crystal relative to the shock direction, and run-to-run variability. The second and third studies are focused on comparing MD predictions head-to-head against continuum predictions for a shock wave passing through, respectively, a cylindrical pore and an elliptical pore. The first sub-study in chapter 2 focuses on shock-induced pore collapse for two different crystal orientations and two different cell thicknesses, to validate decisions on suitable cell orientations and cell dimensions for the subsequent studies. The second sub-study compares predictions from three different independent realizations of the same simulation scenario, to assess run-to-run variability among results for simulations initiated from different but statistically equivalent initial conditions. This study revealed that cell orientation seems to have a moderate effect on the collapse and that transverse thickness has almost no effect on overall system response. The repeatability study provided confidence that a single simulation for a particular scenario can be interpreted as representative. The conclusions from Chapter 2 were then used to guide the design of the MD systems in the second and third study (Chapter 3 4), where MD is used as "ground truth" against continuum model that can capture the circular pore collapse phenomena. Head-to-head comparisons were done between MD predictions and a systematic hierarchy of five different continuum models, each incorporating increasing physical fidelity and amount of information from MD. Analyzing the simulation data qualitatively and quantitatively revealed that the hydrodynamic pore collapse induced by strong shocks was captured closer to MD predictions using a model that was incorporated with most MD-derived parameters. However, for weaker shocks, differences were still evident even for the "best" continuum model. The "best" continuum model from Chapter 3 was then tested for the case of an elongated pore in Chapter 4, where both the MD and continuum models were identical in cell dimensions and impact conditions. This work confirmed that, for non-trivial pore shapes

at intermediate-strength shock speed, isotropic rate-dependent Johnson-Cook-type elastoplastic continuum models predict pore-collapse mechanisms that are consistent with predictions from MD.

Chapter 1

INTRODUCTION

1.1 Motivation

High Energetic Materials (HEMs) have played important roles in many fields such as mining, military, aerospace, civil engineering, and other industrial fields for centuries [1]. The ability to release large amounts of energy at a rapid rate is a unique property that HEMs possess. However, this unique property increases the menace of handling these materials [2]. Therefore, it is important to understand HEM properties and behaviors under extreme conditions to improve safety measures when handling them. This will also help speed up the development of new materials that are safer, more precise, and more environmentally friendly. Studies to understand the thermal and mechanical responses of the HEMs under perturbations such as compression, impact, shock, or flame environments are prominent in literature [3],[4],[5],[6],[7],[8]. These studies use mathematical descriptions for modelling HEMs [9],[10] at the meso-scale. However, such models require extensive data for their parameterization, much of which is needed under conditions (e.g. $300 \leq T \leq 2500$ K, $0 \leq P \leq 50$ GPa) for which experiments to obtain them are extremely difficult, if not impossible. Computer simulations provide a viable and far safer approach to determining data required in extreme conditions while making the process much more economical as well. MD simulations can provide much of the needed information. MD simulations of shock waves in HEMs can help to understand how the materials behave under extreme conditions by analyzing the dynamic changes in pressure, temperature, and the chemical reactions that occur when a shock wave propagates through the material. The predictions obtained from such simulations can then be used to assess the continuum models and guide their improvement. Once a continuum model has been validated, it can then be used to gain insight into the behavior of the material under extreme conditions, thresholds for their safe handling, or for optimizing or developing more efficient materials for the future.

1.2 High Energetic Materials

The significance of using HEMs came out with the development of Dynamite by Alfred Nobel during [11] 19^{th} century, and was mostly used for mining purposes before that time. Today, HEMs are used for mining, quarrying, transportation-related applications, and as well as military applications [12]. Therefore, understanding the sensitivity and behavior of these materials for safe handling is critical.

HEMs contain high chemical potential energy within the molecules, due to the arrangement of atoms in their structure. More specifically, HEMs include both fuel and oxidizing moieties in the molecular structure, once triggered, chemistry in HEMs can occur very rapidly due to a lack of need for diffusion beyond the molecular scale [13]. The rapid propagation of the initiation process will provide enough energy to overcome activation energy barriers for breaking existing bonds (endothermic reaction) and creating new ones (exothermic reaction). Under appropriate stimulation, detonation can occur (section 1.3.1). The heat energy released during the detonation process is due to the difference in internal energy of the reactants and products.

The most common elements present in HEMs are Carbon, Hydrogen, Oxygen, and Nitrogen [14]. The general structure includes a carbon skeleton and oxygen-rich functional groups attached to it. Out of the many oxygen-rich functional groups present, -NO_2 and -ONO_2 are the most abundant oxygen providers for the detonation process [15].

HEMs can be classified as Propellants, Explosives, and Pyrotechnics. *Propellants* are materials that can expand in volume and provide thrust/force to move or propel in consonance with Newton's 3^{rd} law [16]. Propellants are widely used in ammunition and as rocket fuels as they burn at a controlled and comparatively slow rate. *Explosives* are materials that can release huge amounts of energy at a rapid rate [1]. They are used widely for military applications such as Plastic Bonded eXplosives (PBXs), missiles, and grenades. *Pyrotechnics* are less violent materials that are used for fireworks, safety matches, and provide special effects in movies and television [17].

Explosives can be further categorized as *low explosives* and *high explosives*. *Low explosives* can exhibit subsonic detonations (where the reactant front passes at a speed slower than the speed of sound in the material) with a high degree of impact, while *high explosives* can create supersonic-level detonations (where the reaction front passes at a speed exceeding the speed of sound in the material). High explosives used in PBXs are pressed HE crystal that is 90%-95% by weight and a binder that is 5%-10% by weight [18]. The most common high explosives that are used for military PBX's are HMX (1,3,5,7-tetranitro-1,3,5,7-tetraocane), RDX (1,3,5-trinitroperhydro-1,3,5-triazine), TATB

(2,4,6-trinitrobenzene-1,3,5,triamine), 2,2-Bis[(nitrooxy)methyl]propane-1,3-diyl dinitrate (PETN), and 2,4,6-Trinitrotoluene (TNT).

1.2.1 β-HMX

This study is focused on HMX, which is one of the most common nitramine HEMs used in PBXs [19]. The chemical formula for HMX is $C_4H_8N_8O_8$ and contains a heterocyclic eight-membered ring of alternating Carbon and Nitrogen, with -NO_2 functional groups attached to the Nitrogen. See Fig. 1.1. The molecule is non-planar, and the different polymorphs exhibit different ring conformations. HMX exists in six polymorphic forms denoted $\alpha, \beta, \gamma, \delta, \varepsilon$ and ϕ. Among these, β-polymorph is the most stable form in standard ambient conditions [20],[21],[19] and over most of the existence interval of the solid. Because α, δ polymorphs exist only over a narrow temperature domain and at low pressure states, ε and ϕ are "exotic" and exist only above 12 GPa, and the γ form occurs only in a hydrate form [22].

The molecule in the β-polymorph exhibits a chair conformation with a center of symmetry [23]. This monoclinic crystal ($P2_1/n$ or equivalently $P2_1/c$) [24] is centro-symmetrical overall. β-HMX is a white crystalline solid that has a molecular weight of 296.2 g/mol and a density of 1.94 g/cm^3. This polymorph is the least sensitive to external stimuli and encompasses the highest energy density, making it more interesting for military applications. The high detonation velocity (≈10.0 km s^{-1}) and a high detonation pressure (≈35 GPa) of HMX makes it an outstanding candidate for high-performance PBX. The physical and chemical properties of β-HMX required for an accurate mesoscale model have been studied extensively using both experimental [25],[26] and theoretical [27],[28],[29] approaches.

1.3 Shock waves

Waves are disturbances that propagate through a medium, transferring energy without transporting matter. A non-shock wave travels at constant speed, less than or equal to the sound speed, by vibrations/oscillations in the particles and transfers energy continuously when moving through a medium. In longitudinal waves, the particle movement creates regions of compression and rarefaction alternatively as the wave moves through the medium. This creates a sinusoidal change in pressure for a non-shock wave. Some examples of such longitudinal waves are acoustic waves, vibrations of a spring, and ultrasound waves.

In contrast to non-shock waves, shock waves are created when a disturbance moves through a

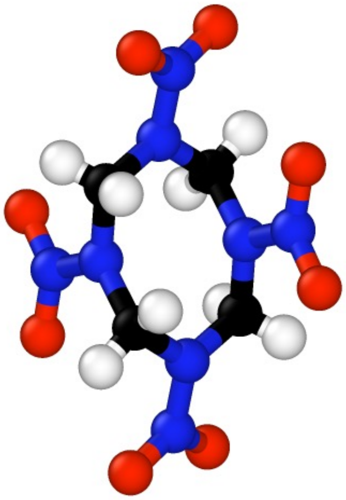

Figure 1.1: 3D structure of β-HMX

medium (plasma, gas, liquid, solid) faster than the ambient speed of sound. This results in a set of distinct characteristics such as abrupt changes in pressure, temperature, and density within a very narrow spacial window of material. Hence, shock waves are highly localized and often related to transient, non-linear events such as lightning, explosions, and supersonic motion.

The speed of sound is the speed at which linear, acoustic pressure disturbances, or sound waves, travel through a medium. When an object or event moves faster than this speed, it compresses the medium in front of it by accumulating air particles resulting in a pressure buildup. This accumulation of pressure creates a shock front (wavefront), marking the boundary between the undisturbed region and the disturbed region of the wave (Fig. 1.2).

Shock waves possess enough energy to cause deformations, changes in temperature and pressure, or damage to the medium in which they moves through. The extent of damage to the medium depends on the material properties and the strength of the shock wave. When a sufficiently strong shock wave passes through HEM, the changes in temperature, and pressure are sufficient to activate the chemistry. This initiation of chemistry using shock waves is elaborated below. The behavior of HEMs under shock waves can be affected by various factors, such as impact speed, angle of impact of the wave, and also due to crystallographic orientation, anisotropy, pre-existing defects in the material. Building a model including all the above-mentioned factors to understand the behavior of a particular HEM when a shock wave passes through, makes it a complicated research problem. Hence, most studies focuses on solving and understanding the effects of one or a few of the above mentioned factors at a time.

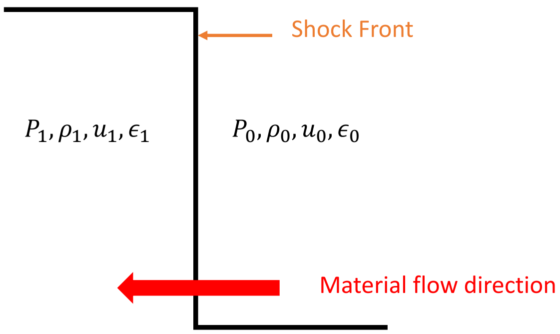

Figure 1.2: Depiction of a single shock wave in a 1D system. The shock front is stationary and material flows from right to left.

1.3.1 Shock Initiation in Energetic Materials

At the microscopic scale, numerous defects such as pores, dislocations, and twin boundaries are present in HEMs. These defects and the anisotropic nature present in their crystal structure [18] lead to local density discontinuities in the material. Shock waves passing through these discontinuities can result in chemical ignition creating energy-localized areas known as "hot spots" [6]. Fig. 1.3 depicts two images (taken from Ref. [30]) from a high-speed gated camera, before and after a shock wave passes through a single crystal of HMX. The red spots in panel (b) indicate high-temperature regions that correspond to hot spots [30]. These hot spots results in an increase in the pressure and temperature in their vicinity. The process by which burning commences at a local site (hot spots) in HEMs due to local thermal conditions is known as *ignition*. The reactive process that follows from ignition that leads to detonation is known as *initiation* [31].

A lot of study has been devoted to understanding shock-induced detonation initiation in PBXs, both experimentally [32],[33],[34] and theoretically [35],[36],[37]. Detailed investigations of material at these extreme conditions are hard to achieve using experimental procedures due to the microscopic scale and short timescales involved in hot spot ignition. Hence, theoretical modeling has been used to study and understand microscopic details of energy localization and dissipation mechanisms that occur in PBXs in the wake of shock passage and during detonation initiation. The theoretical models capable of determining the ignition and growth of hot spots, and the coalescence (initiation) are referred to as "mesoscale" models [20]. Such continuum mesoscale simulations depend on mathematical models that require reliable data for physical parameters to govern the physics behind these simulations [38]. Moreover, the high-level of anisotropy present in HEMs and the absence of a real atomic description in continuum simulations makes them further from reality. By contrast, MD simulations solve the classical Newtonian equations of motion for the atoms in a system, and therefore provide a closer approximation to reality. Even though the computational expense for MD simulations restricts system sizes to the nanoscale, physical parameters obtained from these MD simulations can be used to inform the continuum scale models for better mesoscale predictions [18].

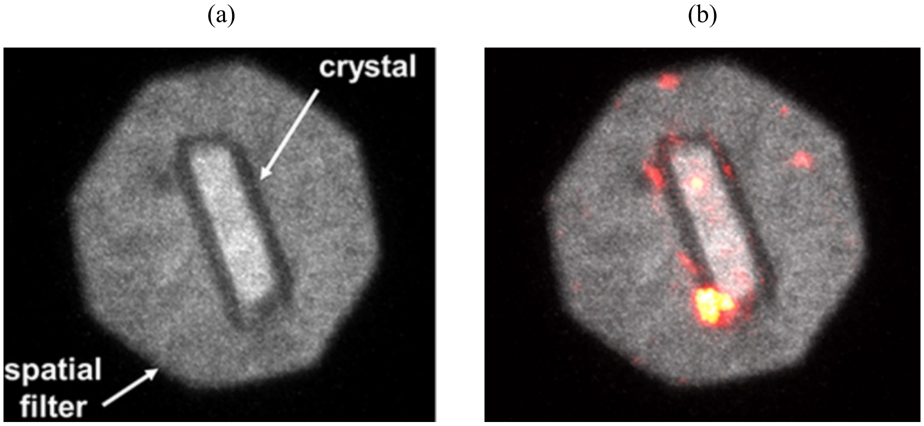

Figure 1.3: Images from a high-speed gated camera. (a) Static image of an HMX single crystal taken prior to the shock wave with an LED lamp as the illumination source. (b) Final superimposed image of "(a)" and thermal emission of "(a)" set to a false-color scheme for enhanced viewing [30].

1.4 Mesoscale Modelling using Continuum Mechanics

Meso-scale modeling using continuum mechanics (CM) is an intermediate step that bridges information from the nanoscale (microscopic data) to the macroscopic domain. CM is a mathematical/numerical description that is used to describe continuous media and allows for intuitive analysis of bulk matter by using partial differential field equations rather than using information about discrete particles. Typical length scales vary from cm to $O(\mu m)$. For the focus of this thesis, we will discuss how continuum scale simulations are performed to understand shock responses in HEMs.

Figure 1.4 shows a flow chart of the basic steps that are involved in CM simulation. Four different aspects need to be fulfilled in order to perform systematic CM simulations. Initially, the material

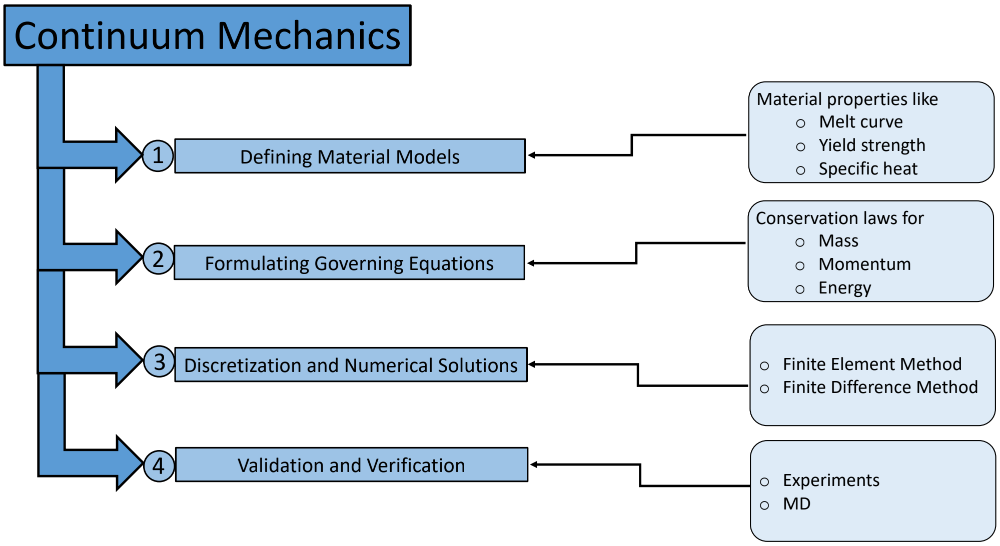

Figure 1.4: Steps to perform a continuum mechanics simulation.

model should be defined with factual data specific to the material of interest, such as the melt curve, specific heat, and yield strength. Material information is critical for understanding the behavior of the material under extreme conditions. Using experimental data is optimal for this purpose. However, due to the limited experimental data at detonation conditions for these HEMs, CM simulations increasingly rely on MD simulations [20] for the required data.

Once the material model is defined, a set of equations known as the Rankine-Hugoniot (jump) conditions that describe the thermodynamic states of material ahead and behind the shock wave is solved for the model. The shock wave is considered a mathematical discontinuity (see Fig. 1.2), they can be expressed as Equation 1.1-1.3 as shown in Fig. 1.2 for a shock wave scenario. In these equations ρ is the density, P is the pressure, u is the particle velocity and ϵ is the internal energy. Equation 1.1 expresses the conservation of mass across the discontinuity. Equation 1.2 is the conservation of momentum, relating the change in momentum (ρu_2) to change in pressure. Equation.1.3 is the conservation of energy, stating a change in internal (ϵ) and kinetic (u_2) energies due to work done by the pressure. The subscript "1" represents the shock-compressed material "behind the shock front" and "0" represents the unshocked material "ahead of the shock front" [39].

$$\rho_1 u_1 = \rho_0 u_0 \tag{1.1}$$

$$p_1 + \rho_1 u_1^2 = p_0 + \rho_0 u_0^2 \tag{1.2}$$

$$\epsilon_1 + \frac{p_1}{\rho_1} + \frac{u_1^2}{2} = \epsilon_0 + \frac{p_0}{\rho_0} + \frac{u_0^2}{2} \tag{1.3}$$

To formulate and numerically solve these equations, there are two popular schemes known as the Finite Difference Method (FDM) and Finite Element Method (FEM). FDM solves differential equations across the boundaries, while in FEM the entire system is divided into small parts creating a mesh in the space dimension of your system. These small parts are known as then finite element discreterization of the system and the formulation of a boundary value problem finally results in a system of algebraic equations. Between the two methods, FEM produces much more accurate results and computationally expensive compared to FDM. The latest CM codes that are being used widely to analyze shock responses at mesoscale are named "hydrodynamics codes" or shortly known as "hydrocodes". These codes are specifically designed to simulate the behavior of fluids under various conditions. For further information on hydrocodes, see Ref. [40].

Once the simulations are complete using CM, the obtained results can be compared using experimental data or MD simulations for validation. Chapters 3 and 4 of this thesis include two studies where MD simulations are used as the "ground truth" to validate CM simulations for shock-induced pore collapse in β-HMX.

1.5 Atomic-Scale Modelling using Molecular Dynamics

Theoretical modeling using MD simulations is a prominent approach for research problems and is extensively used in fields such as material chemistry, electrochemistry, and drug discovery. Simulations in condensed-matter physics involves atomistic data inputs to calculate microscopic data, and then that microscopic data can be transformed into macroscopic data using statistical mechanics. Theoretical studies are particularly useful in determining precise parameters or mechanisms that occur at extreme conditions (high temperature and pressure) where experimental procedures are incapable, too dangerous to perform, or involve large expenses. Even though atomic-scale simulations cannot predict highly accurate quantification due to inhomogeneities present in natural materials on scales inaccessible to MD and other approximations used in the theoretical description, it has been proven over the years that computer simulations complement experimental data (and in favorable cases can be used as a guide for the experiments [41]).

Classical MD simulations use classical mechanics by solving Newtonian equations of motion for a given description of the particle-particle interactions (inter-atomic forces) and thereby determine the trajectory in the phase space of the system [42]. There are key requirements for an MD simulation. All the parametric data that are required for the calculation of the potential energy of the system along with cut-off distances in calculating long/short-range interactions (forces) are present in the Force-Field (FF) used in the simulation. Therefore, the choice of FF that can model the material closest to the experimental data (chemical and physical data) is important. The next requirement is the choice of statistical mechanical ensemble. The ensemble specifies the conditions of the system (constant energy, volume, and temperature) throughout the simulation and can be chosen according to the requirement. The choice of ensemble determines the particular form for the equation of motion to be solved. Then, the initial conditions like the temperature and the pressure state of the system should be decided along with the boundary conditions. Finally, the choice of trajectory integration should be decided. Each of these components is key for an MD simulation and should be chosen carefully to perform an accurate calculation. Details on each of these decisions are described in detail in the sections to follow.

There are limitations associated with these theoretical calculations. Obviously, as the accuracy of the data obtained from such calculations depends on the ability of the FF to represent the material accurately. The spatiotemporal scales (range of nm-μm and ps-ns) that these simulations can be performed is decided upon the computational expense of the calculation.

1.5.1 Force Field

FF for a system in an MD calculation is a collection of mathematical expressions that describes the energy-surface dependence of a system on the positions of its particles (potential energy). The relationship between the force and potential energy can be expressed by Equation 1.4 (where $U_{(r)}$ is the potential of the system with respect to the position). The mathematical expressions present in the FF includes how the particles in the system interact with one another along with their characteristic parameters specific to each system. The interactions between particles are defined using pair potentials or many-body potentials in the FF and exact parameters can be obtained using *ab initio* or semi-empirical quantum chemistry calculations. These parameters can also be obtained using direct experiment data or fits obtained from an experimental and quantum calculation data [43]. The bonded interactions present in the system typically are defined by covalent bonds, three-center angles, dihedral angles, and improper angles. In addition to the bonded interactions, there are non-bonded interactions that are required for the complete description of the potential energy surface. Atoms belonging to different molecules, and atoms separated by three or more covalent bonds inside the same molecule, are considered as non-bonded terms. Thus, the total potential energy of the system is represented by the summation of the bonded and non-bonded terms present in that system.

$$F = -\frac{dU_{(r)}}{dr} = ma \tag{1.4}$$

The following equation (Equation 1.5) represents the mathematical expressions used to define the potential energy of HMX. This equation includes terms for covalent bonds, three-center angles, dihedral angles, improper dihedral angles, and non-bonded terms. Equations 1.6-1.10 presents the detailed descriptions for each of the terms in Equation 1.5.

$$\begin{aligned} U(r,\theta,\phi,\chi) = \sum_{bond} U_{bond}(r) + \sum_{angle} U_{angle}(\theta) + \sum_{dihedral} U_{dihedral}(\phi) \\ + \sum_{improper} U_{improper}(\chi) + \sum_{atomi} \sum_{atomj>i} U_{NB}(R) \end{aligned} \tag{1.5}$$

$$U_{bond} = \frac{1}{2}k_{bond}(r - r_0)^2 \tag{1.6}$$

$$U_{angle} = \frac{1}{2}k_{angle}(\theta - \theta_0)^2 \tag{1.7}$$

$$U_{dihedral} = \frac{1}{2}k_{dihedral}[1 - cos(n\phi)] \tag{1.8}$$

$$U_{improper} = \frac{1}{2}k_{improper}(\chi - \chi_0)^2 \tag{1.9}$$

$$U_{NB} = Ae^{-BR} - \frac{C}{R^6} + \frac{q_i q_j}{4\pi\epsilon_0 R} \tag{1.10}$$

This study implements a modified version [21] of a FF field originally developed by Smith and Bharadwaj (S-B-FF) [44],[45]. This is a non-reactive, all-atom FF with flexible molecules. The original S-B FF implements harmonic functions to model potential energies for covalent bonds, three-center angles, and wag angles; a truncated cosine series to model dihedral angles; implementation of a three-term expression comprised of exponential repulsion, R^{-6} dispersion, and R^{-1} Coulomb interaction (Buckingham-plus-Coulomb terms) to model non-bonded interactions. This FF is well-validated and has been employed in various previous studies [24],[45],[46],[47],[48],[49].

The modifications done to the original S-B FF include; adjustments of N-O and C-O covalent bond-stretching force constants to yield better agreement with the vibrational spectrum of HMX [48]; addition of a very short-range non-bonded R^{-12} repulsion term to the non-bonded interactions to prevent ‘overtopping’ the barrier in Eq. 1.10 under the extreme conditions generated due to shocks [21],[50]; and incorporation of particle-particle particle-mesh (PPPM) k-space technique for computing long-range Coulomb forces with the relative error in forces set to 10 $^{-6}$ [51].

As identified in the S-B FF, a single molecule of HMX contains 28 atoms with 4 elements and 5 different atom types (two Nitrogen atoms, one attached to the -NO_2, and the other that is in -NO_2, are considered as distinct atom types due to their different chemical environments in the molecule), 28 bonds (e.g., atoms C2 and N3 define a single covalent bond) with 4 different bond types, 48 angles (e.g., atoms C2, N3, and N12 define a three-center angle) with 7 angle types, 40 different dihedral angles (e.g., atoms C2, N3, N12, and O23 define a dihedral angle) with 3 dihedral angle types, and 8 improper angles (improper dihedral angles are measured between two planes defined by different groups of atoms; For example, atoms C2, N3, and N12 define one plane, C2, N3, and C4 define another plane and the two planes together define an improper dihedral angle) with 2 improper angle types (see figure 1.5 for reference). Data for one molecule from the exact data file used in the study below corresponds to one molecule at 298 K and 1 atm pressure is given in the Appendix (A.0.1).

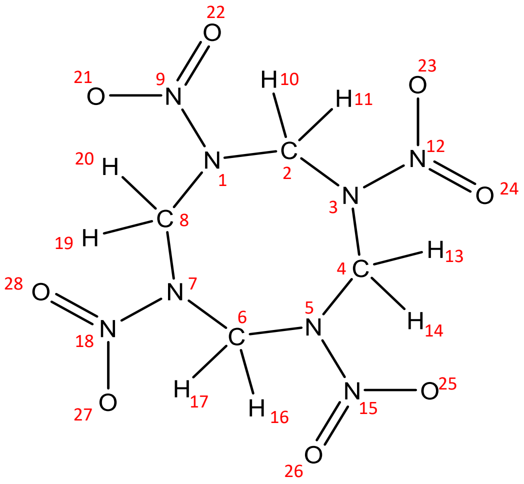

Figure 1.5: 2D planar chemical structure of β-HMX

1.5.2 Initial Conditions

The initial conditions of the simulation are defined prior to carrying out the simulation of interest. This makes MD simulations an initial-value problem. In order to build a simulation cell consisting of an atomic/molecular crystals, crystallographic unit cell data of the material of interest can be replicated along the crystal axes as required. (Unit cell data used for this study are given in the appendices A.0.1). The resulting cell from such replication of unit cell is called the “supercell”.

Often, orthorhombic simulation cells are implemented for the simplicity on cell construction and data analysis.

For a shock wave simulation, the order of 10^3 Å is required along the shock direction in order to allow the material to evolve behind the shock wave. Nonetheless, this length is not enough to analyse any defects that propagate from the material. This demands larger simulation cells that can be too expensive to handle with MD. In order to overcome this problem, simulation cells are often implemented with Periodic Boundary Conditions (PBC). However, great caution should be used when handling the boundaries to avoid unrealistic artifacts that can arise due to the periodicity of the cell.

Once the supercell is built, the entire system can be equilibrated/thermalized to achieve the initial conditions (temperature and pressure state) of the system prior to the simulation. This can be achieved by choosing an appropriate statistical ensemble and assigning appropriate velocities to the atoms. The most commonly used ensembles are microcanonical (NVE), canonical (NVT), and isothermal-isobaric (NPT) ensembles. The letters in the parenthesis are the parameters held constant during the simulation. The individual letters correspond as follows; N is the total number of particles in the system, V is the total volume of the system, E is the total energy of the system, T is the total temperature of the system, and P is the total pressure of the system. Assigning initial velocities can be done based on the appropriate energy requirement and choosing velocities at random based on a Maxwell distribution. Once the system is built and equilibrated appropriately, it will serve as the initial phase space point for the intended production simulation.

1.5.3 Trajectory Integration

The trajectory for each particle in the system is solved using the appropriate set of Newtonian equations of motion, which relate to the potential energy function as shown in Equation (1.4). The trajectory analysis is done at particular timesteps of interest. The timestep is the time interval at which the system is updated during the simulation, and it is imperative to choose an appropriate timestep. The smaller the timestep, the better predictions can be obtained for shorter-time scale phenomena but it can be computationally too expensive for a long simulation. Larger timesteps can fail to conserve the energy of the system to a higher accuracy. In general, a proper timestep can be calculated by dividing the fastest bond frequency present in the system by 100.

A variety of algorithms cen be used to perform the trajectory integration, and care should always be exercised with regard to the accuracy and long-time numerical stability of the results that the integrators produce when choosing one. Commonly used integrators are Runge-Kutta-Gill [52] and various forms of the Verlet integrator [53]. During this work, the velocity Verlet integrator [54] was used due to its high accuracy and efficiency. The equations that have been used to update the positions and velocities using the velocity Verlet algorithm are given below in Equations 1.11 and 1.12 respectively. In these equations, r=position, v=velocity, a=acceleration, δ=timestep t_0=instance at t=0.

$$r_{(t_0+\delta)} = r_{(t_0)} + v_{(t_0)}\delta + \frac{1}{2}a_{(t_0)}\delta^2 \tag{1.11}$$

$$v_{(t_0+\delta)} = v_{(t_0)} + \frac{1}{2}[a_{(t_0)} + a_{(t_0+\delta)}]\delta \tag{1.12}$$

1.5.4 Data Analysis

All the data obtained by Large-scale Atomic/Molecular Massively Parallel Simulator (LAMMPS) [55] simulations were analyzed using home-written Fortran 90 codes. Visualization of the simulations were carried out using OVITO software [56]. Due to the large system size on these simulations, some data were analyzed based on the center-of-mass positions instead of individual atomic data. Spatially resolved properties at a given time were calculated using a grid-based method. Two-dimensional maps of system properties were created by mapping the system space into a virtual Eulerian (Cartesian) grid. Specific details on how the data were analyzed are explained in detail in their respective chapters.

1.6 Thesis Outline

The thesis is constructed as follows: Chapter 2 discusses the effects of sample thickness, transverse orientation, and run-to-run variability on these large-scale pore-collapse simulations. Chapter 3 is focused on building a continuum-scale model that best captures the MD pore-collapse phenomena. In Chapter 4, the "best" model developed in Chapter 3 is tested with a different pore shape and different cell dimensions. Finally, Chapter 5 will conclude the current work and discuss possible future directions.

The work presented in the last two chapters was a collaboration with the University of Iowa research team lead by, Prof. Udaykumar where they performed the CM simulations in comparison to the MD simulations we performed here at Mizzou.

Chapter 2

EFFECTS OF SAMPLE THICKNESS AND TRANSVERSE ORIENTATION, AND RUN-TO-RUN VARIABILITY ON PORE-COLLAPSE SIMULATIONS

2.1 Abstract

Using shock-induced quasi-2D pore collapse in β-HMX as a specific case study, we address three practical questions that arise when designing and interpreting molecular dynamics (MD) simulations of explicit shock wave propagation in crystals. How sensitive are the overall results to sample thickness perpendicular to the (quasi) plane of the problem? For impacts on a given crystal surface, how much does the transverse orientation of the sample matter? And, for a given sample size and orientation, how much run-to-run variability exists among results for independent but statistically equivalent realizations of the shock? The first and second questions are interrelated but pertain individually to assessing the roles of finite-size and crystal anisotropy effects, respectively, on the simulated collapse mechanisms and associated local thermo-mechanical states in the sample during and after collapse. The third addresses the confidence with which the results of individual simulations can be regarded as representative. All three questions become particularly important if the MD predictions are intended to serve as "ground truth" for validation of continuum mesoscale models. Here, quasi-2D samples of (010)-oriented single-crystal β-HMX (β-1,3,5,7-tetranitro-1,3,5,7-tetrazocane) containing a cylindrical pore were subjected to reverse-ballistic impacts, resulting in explicit, supported shock propagation initially along [010], for impact speeds u_p=1.0 and 0.5 km s^{-1}. The individual samples differed in either the thickness perpendicular to the sample plane or the transverse crystal orientation normal to [010] in the quasi-2D cell. Three independent realizations of the shock were performed for a selected case to assess run-to-run variability. Comparisons of qualitative features of the collapse, temperature

and pressure distributions in the samples, and time scales for pore collapse suggest that there is little sensitivity to sample thickness for the same crystal orientation and moderate sensitivity to transverse crystal orientation for samples of the same thickness. Run-to-run variability is evident to the eye in side-by-side system observations. However, overall mechanisms of collapse, distributions for temperature and pressure in the samples, and time scales for collapse are in near-quantitative agreement among the realizations.

2.2 Introduction

Molecular dynamics (MD) simulations are widely used to interrogate the nanoscale physical and chemical properties of energetic materials (EMs) under static and dynamic loading conditions. Given a method for obtaining accurate forces, and assuming the validity of the classical approximation to quantum mechanics, MD can provide quantitative information concerning the pressure-volume-temperature (P-V-T) equation of state including phase boundaries [21],[57],[58],[59],[60],[61],[62],[63],[64] thermal and elastic properties [21],[28],[24],[46],[49],[64],[65],[66],[67] fundamental plastic deformation processes [36],[68],[69],[70],[71],[72],[73],[74],[75],[76],[77] transport properties [28],[47],[49],[60],[64], and thermal chemical reaction rates and mechanisms [78],[79],[80],[81],[82] among others [83]. In many cases, MD predictions agree with data to within experimental uncertainty. Indeed, when data from different sources are inconsistent, MD can sometimes help resolve the source of discrepancy or at least inform the decision as to which data to trust [46],[64]. Moreover, whereas most EM property data are only available for thermodynamic states close to standard ambient conditions or along one or a few isotherms, MD can provide information across wide intervals of P-V-T space relevant to EM initiation and detonation including general constitutive states. This information is needed for quantitative determination of the material sub-models used in physics-based continuum mesoscale simulations wherein the individual constituents and interfaces in a sample are spatially resolved, [18],[20],[50],[63],[84],[85],[86].

Molecular dynamics is increasingly used to simulate transient processes in EMs; for example, shock loading [50],[87],[88],[89],[90],[91],[92],[93] thermal or other non-shock thermo-mechanical stimulation [94],[95],[96], and spectroscopic relaxation phenomena [97],[98],[99]. Focusing on shock waves, MD can provide exquisitely detailed information about how a sample responds to shock passage. Common scenarios include shocks in oriented single crystals [92],[100],[101],[102],[103],[104], across interfaces [105],[106],[107], for initially defect-free samples or ones with pre-existing defects such as grain boundaries [105],[106], and in samples containing larger-scale defects such as pores

[18],[6],[50],[80],[84],[93],[108]. In cases for which the shocked sample is treated as an isolated system, as is the case here, both fundamental and 'bulk' thermo-mechanical and chemical processes occurring during and after shock passage can be determined [109],[110]. The results of such simulations are useful for guiding the formulation (not merely parameterization) of mesoscale physics models, for example by identifying which aspects of the nanoscale physics should be included in the mesoscale material description [84]. Further, by direct head-to-head comparison of mesoscale predictions to MD results obtained for 'identical' sample configurations and impact conditions, MD can provide a 'ground-truth' basis for validation and assessment of mesoscale models [18],[50],[63],[84],[111]. The main concerns with this approach center around the accuracy of the force field used, potential sample finite-size and orientation effects, and the degree to which physics that is inaccessible on the MD scale affects the material behavior at larger scales.

Molecular dynamics simulations of explicit shock wave propagation in three-dimensionally (3D) periodic primary simulation cells (samples) containing tens of millions of atoms are now routine if chemistry is neglected [50],[84]. (Because of the increased cost of force evaluations when chemistry is included, reactive simulations are practically limited to a few million atoms in the case of empirical reactive force fields [80],[81], and several orders of magnitude fewer still if the forces are obtained from a good electronic-structure calculation [79],[112],[113]). However, the samples are still quite small: For β-HMX (ρ=1900 kg m^{-3} and molecular stoichiometry $C_4N_8O_8H_8$), a sample containing 2.5×10^{-7} atoms has a cube-equivalent edge length of only 61.4 nm; that is, ≈0.06 micron. A billion atoms yield a cube with ≈0.2-micron edge length.

In many cases, particularly those involving shock-induced pore collapse or shock interactions with extended defects such as dislocations, a periodic quasi-two-dimensional (quasi-2D) simulation domain is employed in which the sample is 'large' in the (quasi) plane of the problem but thin' in the third direction [18],[6],[50],[84],[108],[111]. If one of the 61.4 nm to 5.0 nm with volume-conserving adjustments to the other two, the square-equivalent edge length in the plane of the problem becomes ≈215.0 nm. This increase in in-plane sample size is important: Using shock-induced collapse of a cylindrical pore as an example, along with the loose rule of thumb that the maximum circle-equivalent diameter of the pore should not exceed one-third of the smallest in-plane sample dimension, a cylindrical pore in the cubic sample would be limited to diameter D≈20 nm; whereas the corresponding quasi-2D sample accommodates D≈70 nm; and for the analogous billion-atom quasi-2D sample, D≈0.45 micron.

Unfortunately, use of the quasi-2D sample geometry increases the likelihood that the MD predictions will be contaminated by finite-size effects in the thin direction. The use of periodic boundary conditions inherently imposes limits on the physics that can occur. For example, the maximum wavelength of phonons supported along some primary-cell lattice vector of length L is L. Of more direct relevance here are the effects of cell-size-related geometric constraints on the evolution of extended defects such as dislocations and nanoscale shear bands. This was discussed by Cawkwell *et al.* in connection with MD simulations of shock propagation in periodic (100)-oriented α-RDX (α-1,3,5-trinitro-1,3,5-triazinane) single crystals. They found that reverse-ballistic shock compression along [100] with impact speed u_p 1.0 km s^{-1} leads to formation of shear bands that propagate in the ([100], [001]) crystal plane at an angle of $\approx \pm 45^\circ$ with respect to [100], filling the [010] crystal zone. When the shear band crosses a periodic face normal to [001], it re-enters the cell at the opposite face. Therefore, the spacing of the shear bands along [100] in the primary cell is simply $L_{(001)} tan(45^\circ)$ where $L_{(001)}$ is the supercell length along [001]. If $L_{(001)}$ is doubled, the shear-band spacing will also increase by a factor of two. While the implications of this for the mechanical state of the material behind the shock are relatively obvious in the case studied by Cawkwell *et al.* [87], the situation in a sample/orientation for which post-shock stress relaxation involves significant dislocation-mediated plasticity will be far more complicated and more subject to sample-size effects, especially in the case of periodic quasi-2D samples.

Finally, conclusions from large-scale MD studies of shock waves in EMs are almost always based on the results of single simulations. We are not aware of any reports of large-scale MD studies of explicit shock waves in EM wherein multiple realizations of the same system set-up and shock conditions were simulated starting from independent but statistically equivalent initial positions and velocities. Ensembles of simulations were, however, employed by Kroonblawd and Goldman in a study of chemistry in graphite subjected to high-rate uniaxial strain. Forces were obtained using density functional tight-binding (DFTB) semi-empirical electronic-structure theory and therefore were computationally demanding. Rather than attempt a single, monumental simulation, Kroonblawd and Goldman [112] chose to perform ensembles of simulations for smaller systems at a given strain rate. Although the individual samples were small, containing only 288 atoms with an initial sample edge length of 19.845 Å along the compression direction, the results revealed a wide variety of operative chemical mechanisms and outcomes from one realization to the next, and these were combined to yield a relatively comprehensive analysis and interpretation of the physics and chemistry. Whereas the run-to-run variability reported by Kroonblawd and Goldman is not surprising given the small system sizes studied, one might anticipate that independent but statistically equivalent realizations of millions-of-atoms MD shocks would yield fundamentally similar outcomes.

In this study, we investigate the effects of simulation cell thickness and transverse crystal orientation in periodic, quasi-2D samples of (010)-oriented β-HMX. For a selected case, we report the results of three independent realizations of the same system to assess run-to-run variability. Details of the MD simulation setups and analyses are described in Sec. 2.3. Results and a brief discussion are presented in Secs. 2.4 and 2.5, respectively, with concluding remarks in Sec. 2.6.

2.3 Methods

2.3.1 Force Field

A variant [21] of the all-atom, fully flexible, non-reactive force field originally developed by Smith and Bharadwaj (S-B) [44],[45] was used. The potential energies for covalent bonds, three-center angles, and improper dihedrals in the S-B force field are modeled as harmonic oscillators, and dihedral-angle potentials as truncated cosine series. Forces between atoms belonging to different molecules, and between atoms separated by three or more successive covalent bonds within a molecule, are described by a three-term expression comprising exponential repulsion, R^{-6} dispersion, and R^{-1} Coulomb interactions (*i.e.*, Buckingham plus Coulomb). The harmonic force constants for the N-O and C-H bonds were adjusted to better reproduce experimental vibrational spectra [48]. Also, because the Buckingham-plus-Coulomb potential exhibits a maximum at distances $R\approx0.1$ nm, with a divergence to $-\infty$ for shorter distances, a very-short-range R^{-12} pairwise repulsion was added that prevents 'overtopping' the barrier under the extreme conditions generated by the shocks [21],[50]. A real-space non-bonded cut-off distance of 1.1 nm was used for the repulsion, dispersion, and short-range Coulomb terms. Long-range ($R>1.1$ nm) Coulomb interactions were computed in k-space using the particle-particle particle-mesh (PPPM) method [51] with the relative error in forces set to 10^{-6}.

2.3.2 Simulation Cell Setup and Preparation

2.3.2.1 Overview and Model Definition

The overall simulation setup is shown in Fig. 2.1(a). We consider three different quasi-2D primary simulation cells (models) for β-HMX in the $P2_1/n$ space group setting. Each is $\approx$150 nm$\times\approx$150 nm along the two 'large' directions—which define the quasi-planes for the models—and contains an initially 50 nm diameter cylindrical pore positioned at the center. The $\boldsymbol{b}$ crystal lattice vector is always parallel to $+\hat{y}$ in the Cartesian frame and all three models have a free-surface normal vector that is precisely parallel to [010]; that is, (010)-oriented crystals. The models differ in (1) thickness along the thin direction and (2) orientation and shape perpendicular to $\boldsymbol{b}$. The thickness is ≈5 nm for Model 1 and ≈10 nm for Models 2 and 3.

Models 1 and 2 are built from simple replications of the P2_1/n unit cell, by factors of 8$\boldsymbol{a}$ x 146$\boldsymbol{b}$ x 198$\boldsymbol{c}$ and 16$\boldsymbol{a}$ × 146$\boldsymbol{b}$ × 198$\boldsymbol{c}$ respectively. The mapping between the monoclinic crystal frame and the Cartesian lab frame is $\boldsymbol{a}||\hat{\boldsymbol{x}}$, $\boldsymbol{b}||\hat{\boldsymbol{y}}$ and $\boldsymbol{c}$ in the $+\hat{\boldsymbol{z}}$ half space of the x–z plane. See Fig. 2.1(b). The pore axis direction is parallel to [100] ($||\boldsymbol{a}$). We will refer to the orientation used in Models 1 and 2 as the natural orientation. An interesting feature of Models 1 and 2 is that, based on MD studies due to Picu and co-workers [114] which used effectively the same force field as here, Models 1 and 2 might reflect a "simplest" limiting case.

For Model 3, a *generalized* unit cell was generated using the Generalized Crystal-Cutting Method (GCCM) [48], subject only to the restrictions that the cell has (a) a cell-face normal vector exactly parallel to [010], (b) an edge length of ≈10 nm along one of the other lattice vectors, and (c) an overall shape that is close to orthorhombic. The resulting generalized unit cell [see Fig. 2.1(c)] was replicated in 3D space (1 × 160 × 90) to yield a supercell with edge lengths approximately the same as for Model 2. The pore-axis direction in Model 3 is parallel to $\hat{\boldsymbol{x}}$. The crystal-frame spatial relationship between the two models is shown in Fig. 1(d) where, for both the natural (red) and GCCM (blue) orientation, the [010] direction which is parallel to the initial lead shock direction points into the plane of the page. The Cartesian basis vectors shown in Fig. 1(d) correspond to the natural orientation, with $\hat{\boldsymbol{x}}$ || [100] || $\boldsymbol{a}$. The GCCM model is rotated in the x-z plane, and translated slightly along $\hat{\boldsymbol{y}}$ || [010], so that molecules in the two models overlap precisely. Yellow arrows identify the pore-axis directions for the two samples. The acute angle between the two pore-axis directions, both of which are parallel to the plane of the page, is approximately 60°. Details of the simulation cell dimensions, numbers of molecules, and crystal orientations for all three models are provided in Table 2.1.

Shock waves were simulated using a reverse-ballistic geometry in which the sample consisting of flexible molecules strikes a rigid, stationary piston with impact velocity $\boldsymbol{u}_p$. The piston is ≈3 nm thick and is composed of rigid β-HMX with the same orientation as the sample. The result is a shock wave that prior to encountering the pore propagates through the sample anti-parallel to $\boldsymbol{u}_p$, with speed $\boldsymbol{u}_w$ in the frame of the stationary piston; see Fig. 2.1(a). The shock speed $\boldsymbol{u}_s$ in the Galilean-related moving-piston frame is $\boldsymbol{u}_s$=$\boldsymbol{u}_w$+$\boldsymbol{u}_p$. Three-dimensional periodic boundary conditions were applied in all cases. A 10.0 nm long vacuum region was added to one end of the simulation domain along the shock direction [i.e., the "top" in Fig. 2.1(a)] to minimize long-range electrostatic interactions across the associated periodic boundary. For all three models, impact occurs on (010)

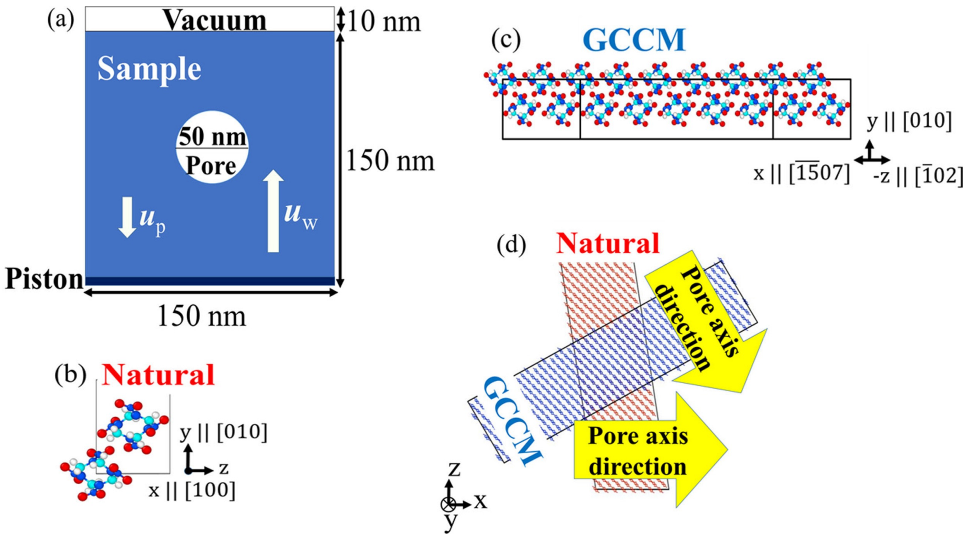

Figure 2.1: (a) Schematic diagram of the cell setup for shock simulations. (b) and (c): Depictions of β-HMX unit cells for (b) Models 1 and 2 and (c) Model 3. Carbon atoms are shown in cyan, nitrogen in navy, oxygen in red, and hydrogen in white. (d) Spatial relationship between the quasi-2D sample orientations/shapes in Model 2 (red) and Model 3 (blue), looking down the [010] axis (which is common to all three models); the Cartesian axes shown correspond to the lab-frame orientation of the natural unit cell.

planes, with velocity $\boldsymbol{u}_p$=(0, $-u_p$, 0) and u_p=0.5 or 1.0 km s^{-1}. Therefore, the initial shock direction is always [010]. The shock wave is supported until it reaches the free surface of the sample.

Model	L_x(nm)	L_y(nm)^a	L_z(nm)	Number of molecules^b	Crystal Orientation
1	5.3	162.6 (150.5)	150.4	422,960 (413,456)	[100]|| $\hat{\boldsymbol{x}}$ [010]|| $\hat{\boldsymbol{y}}$ [001] in +z halfspace
2	10.5	162.6 (148.9)	150.4	845,920 (826,912)	As for Model 1
3	10.5	167.0 (156.5)	158.7	920,274 (903,624)	[-15,0,7]|| $\hat{\boldsymbol{x}}$ [010]|| $\hat{\boldsymbol{y}}$ [1,0,-21]|| $\mathbf{z}$

Table 2.1: Simulation domain and sample dimensions, numbers of molecules, and crystal orientations.

^{a} *Top entry:primary cell domain length along the shock direction. The domain comprises the ≈3 nm piston, the sample with pore, and the 10 nm vacuum region. Parenthetic entry: sample length at t=0 of the shock simulation.* ^{b} *Top entry: total number of HMX molecules in the system. Parenthetic entry: number of molecules in the sample.*

2.3.2.2 Equilibration Details

The simulations were performed using the LAMMPS [55],[115] code with velocity Verlet [53] integration. The periodic systems comprising the piston, sample containing the pore, and the 10 nm gap were thermalized at 300 K using a two-step procedure. Molecules belonging to the piston were treated as fully flexible during the equilibration. First, an isochoric-isoenergetic (NVE) simulation was performed for 1.0 ps using a 0.1 fs time step. The system kinetic temperature T, referred to hereafter as temperature, was computed every 10.0 fs and atomic velocities were rescaled to 300 K if the unsigned difference between the instantaneous system temperature and the target temperature was greater than 10 K. This was followed by 5.0 ps of isochoric-isothermal (NVT) integration at 300 K using the Nose-Hoover thermostat [116],[117]. The NVT time step was 0.2 fs and the thermostat coupling parameter was set to 1000 fs. New atomic velocities were selected from the 300 K Maxwell distribution every 1.0 ps during the NVT integration. This was done to partially depopulate ‘breathing modes’ in the sample that are excited by instantaneous creation of the pore and the vacuum region at the top of the sample. It was confirmed that this protocol yielded a well-defined thermodynamic temperature with the desired value.

2.3.3 Shock Simulation Details

To generate the reverse-ballistic shocks, starting from the phase-space points at the ends of the equilibration trajectories atomic velocities and forces for atoms belonging to the piston were set to and maintained at zero, and the impact velocity vector $\boldsymbol{u}_p$ was added to the instantaneous thermal velocities of atoms in the sample. Shocks were simulated in the NVE ensemble using a 0.1 fs time step and were continued until the sample length, measured using the center-of-mass position of the layer of molecules at the free surface of the sample, passed through a minimum and increased to 110% of the value at maximum compression. Atomic Cartesian positions, velocities, and per-atom stress tensor components were recorded at 0.1 ps intervals for post-processing.

2.3.4 Trajectory Analysis

Details of the analyses used are available in Ref.[84] so are only briefly summarized here. A virtual tetragonal Eulerian grid, with a grid-cell edge length of 1.50 nm in the plane of the problem and extending through the entire sample along the thin direction, was superposed onto the computational domain. Atoms not molecules were assigned to a grid cell based on their instantaneous positions as the simulation progressed. The instantaneous temperature and pressure in a given grid cell were calculated using the atomic velocities and per-atom stress tensor components for that set of atoms. The shock front location and speed were determined using the maximum kinetic-energy gradient criterion [101],[103]. Note that in the calculation of pressure, we do not correct the kinetic contribution to the per-atom stress to account for the whole-body translation of sample material ahead of the shock front. This will be mentioned again in Sec. 2.4.2.1.

Field data calculated as described just above were used to generate 2D snapshots of temperature T and pressure P as functions of time. Those same data were used to calculate time-dependent probability distribution functions (PDFs) T and P For constructing the PDFs, instantaneous field data were sorted into histogram bins. The bin widths are 12.5 K and 0.17 GPa for the 1.0 km s^{-1} impacts and 5 K and 0.075 GPa for u_p=0.5 km s^{-1}. Each histogram was independently normalized to unity at each instant of analysis.

The scaled pore area A/A_o was monitored as a function of dimensionless time t/t^*, where A_o is the area of the pore at t=0 and $t^* = D/u_s$ is the time required for the shock to traverse a distance through bulk material equal to the initial pore diameter, D=50 nm; t^* is determined independently for each simulation. The same Eulerian grid mentioned above was used to determine the area of the pore at a given instant. Any cell containing 10 or fewer atoms is said to be unoccupied and therefore contributes 1.5 nm x 1.5 nm=2.25 nm^2 to both the numerator and denominator in A/A_o. For reference, in bulk β-HMX crystal at standard ambient conditions, an occupied grid cell for Model 1 would contain over 1,200 atoms.

Although the bulk shock speeds for a given impact speed are essentially identical across the three models (see Table 2.2), the time scales for collapse are somewhat different for Models 1 and 2 vs. Model 3 due to the different pore-axis directions. Therefore, in some of the analyses below for which the objective is comparisons at equivalent times in the temporal frame of the collapsing pore, we present results at times t_c+$\Delta^{\pm}$, where t_c is the instant of maximal pore closure in each simulation and $\Delta^{\pm}$ is a time offset with negative and positive values for pre- and post-collapse times, respectively. For the 1.0 km s^{-1} impacts, the pores collapse completely and t_c is defined as the first instant when A/A_o reaches zero. The pores do not collapse completely for u_p=0.5 km s^{-1} but A/A_o exhibits a steady-fluctuating plateau value; t_c in these cases is taken to be the instant when A/A_o reaches the first local minimum within the plateau region. Values of t_c for all three models and both impact speeds are provided in Table 2.2.

2.4 Results

The results are organized as follows. Overall comparisons among predictions for temperature and pressure in the samples are provided in Sec. 2.4.1. Section 2.4.2.1 compares results for PDFs for temperature and pressure for Models 1 and 2; that is, the thickness study. Section 2.4.2.2 compares analogous results for Models 2 and 3; that is, the orientation study. Section2.4.3 presents an assessment of run-to-run variability among three independent realizations of Model 1 for the case u_p=1.0 km s^{-1}.

In the following, results for Models 1, 2, and 3 are consistently plotted in black, cyan, and magenta, respectively, using a solid line style for u_p=1.0 km s^{-1} and dashed for 0.5 km s^{-1}. Intervals and ranges are consistent across all figures, with different values for the two impact speeds. For clarity and continuity of presentation, some of the results for Model 2 appear in multiple figures, and similarly for Trial 1 of 3 for Model 1 at u_p=1.0 km s^{-1}. Animations of the HMX molecular center-of-mass positions for all eight simulations are available in the online supporting information in [118].

u_p (km s^{-1})		Model 1^b	Model 2	Model 3
1.0	u_s	5.94 ±0.03^a	5.91 ±0.03	5.88 ±0.03
	t_c	26.8	26.6	27.7
0.5	u_s	4.86 ±0.03^a	4.87 ±0.03	4.84 ±0.03
	t_c	55.3^c	55.5^c	55.5^c

Table 2.2: Shock speeds u_s (km s^{-1}) and instants of pore closure t_c (ps) for Models 1, 2, and 3.

[a] *Trial 1 among the three discussed in Sec. 2.4.3.* [b] *Uncertainties are standard errors of regression.* [c] *The value of t_c is taken as the time at which plateaus at ≈0.01 for Models 1 and 2 and ≈0.12 for Model 3. See Figure 2.6(b) and discussion thereof.*

2.4.1 Overall Comparison (Figures 2.2-2.4)

Figures 2.2 contain sequences of snapshots for temperature and pressure, respectively, for all three models for the case u_p=1.0 km s^{-1}. Left to right, the columns correspond to Models 1, 2, and 3. From top to bottom, the rows correspond to times t=t_c-8.0 ps, t_c, and t_c+5.0 ps. Fig. 2.3 are exactly analogous to Fig. 2.2 except that the results are for u_p=0.5 km s^{-1} at times t=t_c-24.0 ps, t_c, and t_c+5.0 ps. Overall, for a given u_p all three models predict qualitatively similar results. Material flow

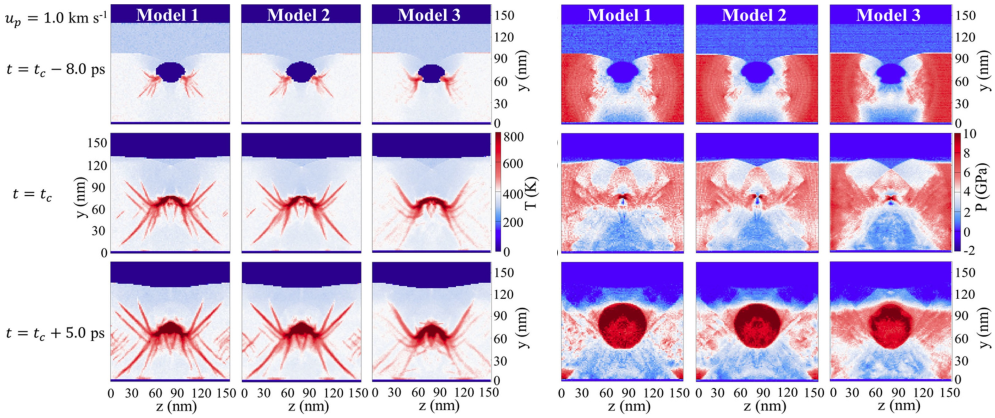

Figure 2.2: Instantaneous local temperature (9 panels at the left) and pressure (9 panels at the right) at three times for u_p=1.0 km s^{-1}.

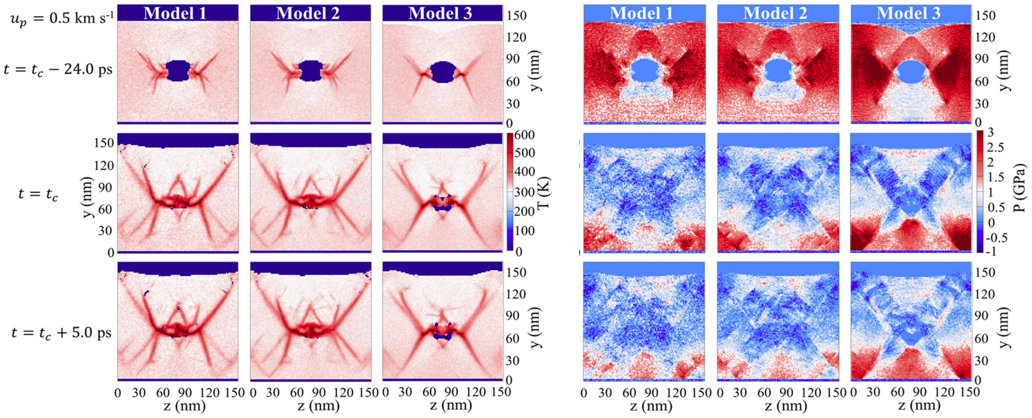

Figure 2.3: Instantaneous local temperature (9 panels at the left) and pressure (9 panels at the right) at three times for u_p=0.5 km s^{-1}.

into the pore occurs from all sides in the wake of lead shock passage across the pore region, with non-homogeneous flow ('extrusion') into the pore cavity. (See Figs. 2.2 and 2.3.) Shear localization occurs at the pore surface and propagates into the sample at a small set of characteristic angles and with some degree of branching. Based on the HMX molecular center-of-mass animations in the supporting information, the shear bands for Models 1 and 2 evolve from regions of 'molecularly thin' dislocation slip.

For all three models at u_p=1.0 km s^{-1}, both shear localization in the sample and inhomogeneous flow into the cavity commence from the pore wall at locations approximately 45° below the equator of the pore, which is approximately oval shaped at the time. Subsequent extrusive flow occurs along roughly the same directions (Fig. 2.2). From the animations, both natural-orientation samples (Models 1 and 2) exhibit clear dislocation nucleation at the pore wall followed by initially molecularly thin regions of dislocation slip that subsequently broaden into narrow shear bands as the dislocations propagate into the sample. Although the final shear-band patterns are quite similar, the effects of sample thickness manifest in the projected thicknesses of the shear bands for the two cases, with Model 2 exhibiting thicker features than Model 1. Shear localization is also apparent for the GCCM orientation (Model 3) but with a final shear-band pattern that differs from Models 1 and 2 in terms of spatial distribution and orientation, and with significantly greater projected shear-band thickness for Model 3.

For u_p=0.5 km s^{-1}, shear localization and extrusion commence in a fashion similar to that described just above for u_p=1.0 km s^{-1}. However, for this weaker impact the transverse extrusive flow propagates almost horizontally inward toward the vertical centerline of the pore, for all three models (Fig. 2.3). The natural orientation samples (Models 1 and 2) exhibit narrower shear bands than are obtained for the GCCM sample (Model 3), and also greater extents of coherent fracture and subsequent crystallite entrainment in the extrusive flow. Interestingly, Model 3 exhibits extrusive flow parallel and anti-parallel to both in-plane cardinal Cartesian directions, that is, from both sides of the equator and from both poles. The horizontal flow toward the vertical centerline is essentially symmetric, whereas flow is faster from the top pole than from the bottom. By the end of the simulation for Model 3, at which time the sample length has increased under shock release from the free surface by 10% relative to the value at maximum compression, the zones of inward horizontal flow have just touched; neither region of flow from the poles has reached the equatorial stagnation zone by that time.

Flow also leads to a reduction in pressure in the vicinity of the pore relative to the bulk shock pressure away from the pore region. The highest temperatures are obtained near the collapse site at and shortly after collapse time t_c (Figs. 2.2 and 2.3 panels to the left). Collapse for u_p=1.0 km s^{-1} results in a distinct collapse-induced shock wave (CSW) that propagates radially outward from the collapse site (Fig. 2.2 right panels). For u_p=0.5 km s^{-1} (Fig. 2.3 right panels), the collapse is so weak that essentially no CSW is produced. Indeed, the pressure in the collapse zone is significantly lower than the bulk post-shock pressure away from the collapse zone. Animations depicting the time evolution of radial pressure profiles in the CSWs for Model 2 at both impact speeds are provided in the supporting information[118].

2.4.1.1 Effect of Sample Thickness

For both T and P, the results for Models 1 and 2 both natural orientation, differing only in sample thickness are very similar for a given u_p and time relative to t_c. Although the shear-band patterns for Models 1 and 2 in Figs. 2.2 and 2.3 differ slightly for the two sample thicknesses, the differences are qualitatively similar to those obtained among trials in the run-to-run variability study for Model 1, discussed below in Sec. 2.4.3. The results for pressure are even more similar than for temperature.

2.4.1.2 Effect of Transverse Sample Orientation

Comparison between predictions for Models 2 and 3 natural and GCCM orientations, respectively, both 10 nm thick among Figs. 2.2 and 2.3 reveals a greater dependence of the qualitative features of collapse with respect to quasi-2D transverse crystal orientation than to sample thickness. The most apparent difference is that whereas the pore in Model 2 collapses almost completely (plateau $A/A_o \approx 0.01$) for u_p=0.5 km s^{-1}, it does not do so for Model 3 ($A/A_o \approx 0.12$); see Fig. 2.3(left panels). The shear-band patterns for Models 2 and 3 also differ noticeably, particularly for u_p=1.0 km s^{-1} (Fig. 2.2 left panels), with fewer and less-branched bands overall and fewer intense downward-growing ones observed for the GCCM orientation. The post-collapse hot-spot cores for the two Models exhibit similar but distinguishable shapes. Pressure contours (Figs. 2.2 and 2.3 right panels) for Models 2 and 3 are more different than was the case for Models 1 and 2.

2.4.1.3 Pore Areas vs Time

Figure 2.4 contains plots of scaled pore area A/A_o vs. scaled time t/t^* for all cases studied. Panels (a) and (b) compare Models 1 and 2, and Models 2 and 3, respectively, for both impact speeds. Panel (c) compares results for the three independent realizations of Model 1 with u_p= 1.0 km s^{-1}. The time origin for each curve in Fig. 2.4 corresponds to the instant when the lead shock wave first reaches the pore wall in a given simulation. Sample thickness has essentially no effect for the natural orientation and impact speeds studied [panel (a)]. Results for Models 2 and 3 [panel (b)] show that the transverse orientation does affect the collapse profile. The rate of collapse for u_p= 1.0 km s^{-1} is slightly faster for Model 2 than for Model 3. For Model 2 (and Model 1) at u_p=0.5 km s^{-1}, collapse occurs at $t/t^* \approx 4.5$. By contrast, and as noted above in connection with Fig. 2.3, for that same u_p the pore in Model 3 does not collapse completely but achieves a plateau value at approximately the same time for which maximal closure occurs for Models 1 and 2. The profiles for the three realizations of Model 1 with u_p=1.0 km s^{-1} are 'identical' to within the line weights of the curves [panel (c)].

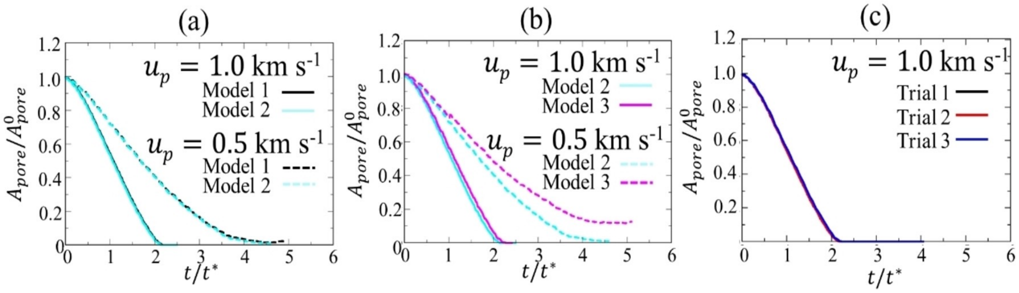

Figure 2.4: Comparisons of scaled pore area A/A_o vs. scaled time t/t^* for (a) Models 1 and 2, (b) Models 2 and 3, and (c) among three independent realizations for Model 1.

2.4.2 PDF Analysis of T and P (Figures 2.5-2.8)

2.4.2.1 Effect of Sample Thickness

Probability distribution functions of system temperature and pressure for Models 1 and 2, which only differ in thickness, are compared in Figs. 2.5 and 2.6 for impact speeds u_p=1.0 and 0.5 km s^{-1}, respectively. Rows correspond to temperature (top row) and pressure (bottom). The two columns at left contain time-dependent PDFs (TD-PDFs) for Models 1 and 2, respectively, and the two to the right superposed instantaneous PDFs for the two models at relative times t=t_c+$\Delta^{\pm}$. Probabilities in the TD-PDFs are colored based on a log$_{10}$ scale; purple and green horizontal lines denote the pre- and post-collapse instants shown in the two columns at right in Figs. 2.5 and 2.6.

For the 1.0 km s^{-1} impact (Fig. 2.5), prior to lead shock arrival at the pore at t≈9.0 ps the temperature distributions for both Model 1 [panel (a)] and Model 2 [panel (b)] are sharply peaked at T=300 and 400 K, indicating a 100 K jump in temperature across the shock front in bulk material. The corresponding values for pressure are P=0.5 and 8 GPa [(e) and (f)]. The reason for 'non-zero' pressure for material ahead of the shock was explained in Sec. 2.3.4. The pressure in material ahead of the shocks is in fact 0 GPa and therefore the bulk pressure jump across the shock front in Fig. 2.5

is actually 8 GPa. Calculated pressures are, however, accurate for material behind the lead shock.

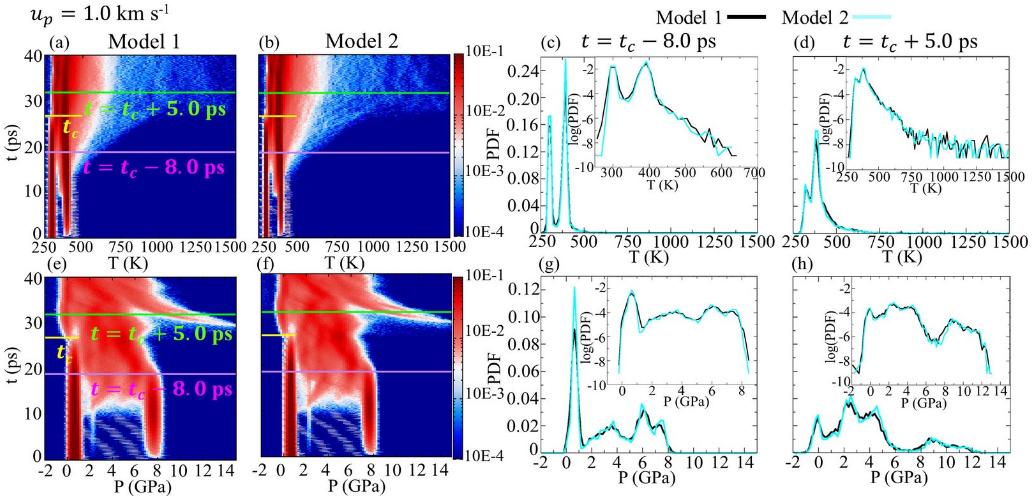

Figure 2.5: For Models 1 and 2 with u_p=1.0 km s^{-1}, PDFs for temperature (top row) and pressure (bottom). Columns at left: TD-PDFs. Columns at right: PDFs at the relative instants t=t_c+$\Delta^{\pm}$ indicated by horizontal lines in the TD-PDFs; insets show the same results but on a $\log_{10}$-linear scale.

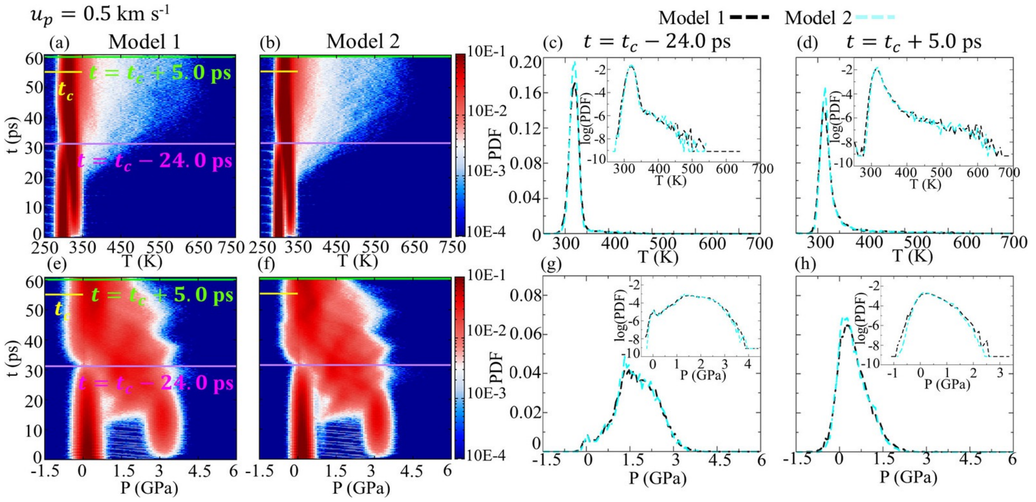

Figure 2.6: As in Figure 2.5 but for u_p=0.5 km s^{-1}

As shown in Figs. 2.2 and 2.3, shock arrival at the pore surface results in material flow into the cavity and a rarefaction wave that travels toward the piston. These processes cause a decrease in temperature ($\Delta T \approx$ 20 K) for already shock-compressed material in the vicinity of the pore, as is apparent in Figs. 2.5(a) and 2.5(b) where the probability for T=380 K increases at $t\approx$9.0 ps. After the lead shock passes the equator of the pore ($t \approx 14.0$ ps), material in the vicinity of the pore surface is extruded into the cavity. This leads to strain localization in the form of shear bands that grow outward into the shocked material at angles of approximately 45° from horizontal and approximately symmetrically about the vertical centerline of the pore; see also Fig. 3(a) of Ref.[84]. These processes are accompanied by increased probability for temperatures between 400 and 1000 K from $t \approx 14.0$ ps until the time of pore closure ($t \approx 27.0$ ps). Pore closure and abrupt stagnation of flow results in a hotspot with $T > 1000$ K at the collapse site, leading to a sudden increase of amplitude in the high-temperature tails of the PDFs.

Similar features are present in the TD-PDFs for pressure for the two models [Figs. 2.5(e) and 2.5(f)]. The rarefaction wave generated at $t \approx 10.0$ ps causes an increase in probability for pressure values between 0.5 and 8 GPa. The CSW emanating from the collapse zone is clearly evident as intense, abruptly formed high-pressure tails in the TD-PDFs after $t \approx 27.0$ ps. It is interesting to note, and intuitively obvious upon reflection, that whereas the local temperatures in Figs. 2.5(a) and 2.5(b) increase gradually above the bulk shock temperature during the entire collapse process, and then rapidly upon pore closure, pressures during pore collapse [panels (e) and (f)] are essentially bounded by the values in unshocked and shocked bulk material until the final instants before final collapse. (The seemingly increased probabilities for $P = 4$ and 6 GPa prior to shock arrival are 'artifacts' caused by the 1.5 nm in-plane spatial resolution of the Eulerian grid used for the analysis: the width of the lead shock wave is smaller than the grid spacing, and this leads to "mixed cells" containing both unshocked and shocked material.)

The TD-PDFs for Models 1 and 2 at $u_p = 1.0$ km s^{-1} are quite similar. Superposed instantaneous PDFs for T [Figs. 2.5(c) and (d)] and P [2.5(g) and (h)], evaluated at the respective instants $t = t_c$-8.0 ps and $t = t_c + 5.0$ ps, provide a quantitative comparison. As expected based on the TD-PDF results, the two models yield very similar results for both temperature and pressure. (The peak at $P = 0.5$ GPa in Fig. 2.5(g) and in subsequent analogous figure panels below where instantaneous PDFs for pressure at pre-collapse instants for cases with $u_p = 1.0$ km s^{-1} are shown corresponds mainly to material ahead of the shock that is actually at zero pressure.)

Figure 2.6 contains results exactly analogous to those in Fig. 2.5, but for the 0.5 km s^{-1} impact. As expected, the shock-induced temperature and pressure jumps in bulk material are smaller ($\Delta T \approx 40$ K and $\Delta P \approx 3$ GPa) compared to those for $u_p = 1.0$ km s^{-1}, and the time scales are longer. Otherwise, the most significant difference for the two impact speeds is the absence of an apparent CSW for the weaker impact, as already noted in Sec. 2.4.1. As for the $u_p = 1.0$ km s^{-1} impact, the probability time slices for both T and P at $t = t_c$-24.0 ps and $t = t_c + 5.0$ ps are almost identical for Models 1 and 2.

2.4.2.2 Effect of Pore-Axis Direction

Figure 2.7 and 2.8 contain comparisons of results for Models 2 and 3, both of which are 10 nm thick but differ in the direction of the pore axis in the quasi-2D sample (see Table 2.1).

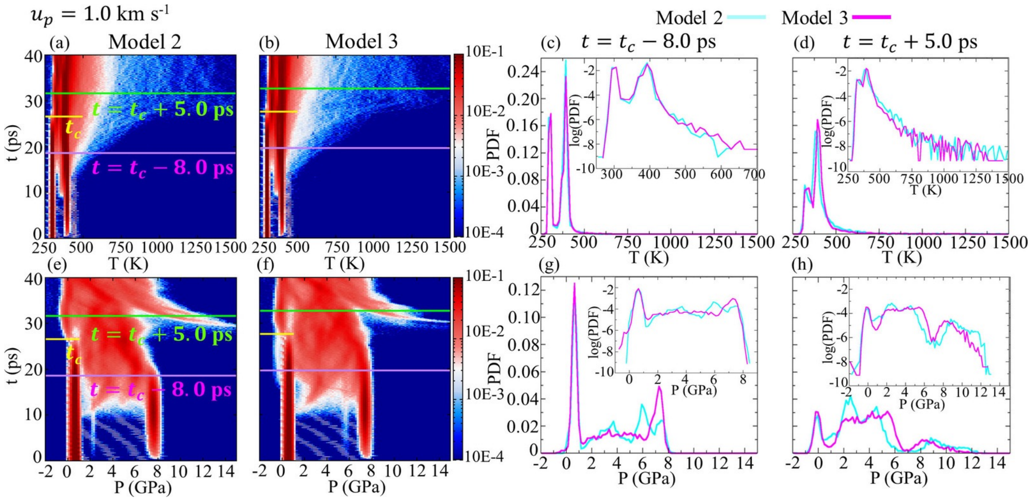

Figure 2.7: For Models 2 and 3 with u_p=1.0 km s^{-1}, PDFs for temperature (top row) and pressure (bottom). Columns at left: TD-PDFs. Columns at right: PDFs at the relative instants t=t_c+$\Delta^{\pm}$ indicated by horizontal lines in the TD-PDFs; insets show the same results but on a log$_{10}$-linear scale.

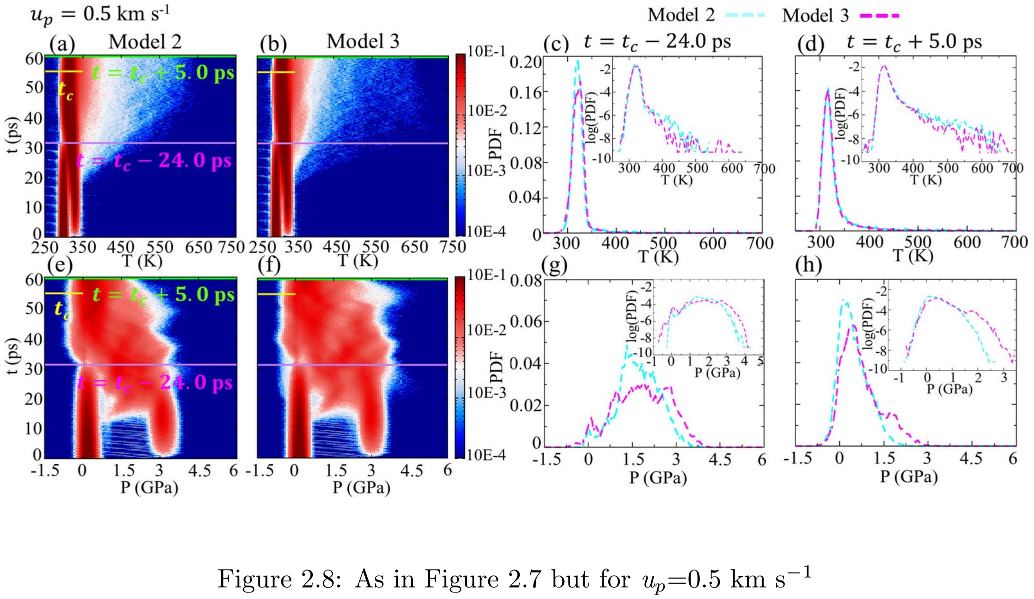

Figure 2.8: As in Figure 2.7 but for u_p=0.5 km s^{-1}

For u_p=1.0 km s^{-1} (Fig. 2.7), the TD-PDFs for temperature and pressure for the two models exhibit similar features. The bulk shock jumps in T and P are approximately 100 K and 8 GPa. One distinct feature in the temperature TD-PDFs for the two models is that the probability for T>400 K is greater for Model 2 [Fig. 2.7(a)] than for Model 3 [Fig. 2.7(b)] after the lead wave passes the equator of the pore at t≈14.0 ps. This is consistent with the earlier observation of more shear bands for Model 2 compared to Model 3. Increased probability in the high-pressure tail is observed for Model 2 [panel (e)] compared to Model 3 [panel (f)], indicating that the natural orientation yields a stronger CSW compared to the GCCM sample.

The instantaneous PDFs for T for Models 2 and 3 exhibit similar features [Figs. 2.7(c) and 2.7(d)]. The instantaneous PDFs for P are in less good agreement than for T. Prior to maximal pore collapse [Fig. 2.7(g)], the pressure away from the pore is higher for Model 3 (≈7 GPa) than for Model 2 (≈6 GPa). Also, a stronger CSW results for Model 2, as can be seen by the higher probability for pressure P>9 GPa for Model 2 than for Model 3 [Fig. 2.79(h)]. These results are consistent with observations drawn from the top and bottom rows of Fig. 2.2.

The TD-PDFs for Models 2 and 3 are more similar for u_p=0.5 km s^{-1} (Fig. 2.8) than for the 1.0 km s^{-1} impact (Fig. 2.7). The more intense shear band formation predicted for Model 2 vs. Model 3 correlates with higher probability for T>400 K, pre- [Fig. 2.8(c)] and post-collapse [Fig. 2.8(d)]. No apparent CSW (*i.e.*, high-pressure tail) is observed for either model [Figs. 2.8(e) and 2.8(f)]. The pressure away from the pore (P>2.5 GPa) is higher for Model 3 than for Model 2 at the corresponding instants [panels (g) and (h)].

2.4.3 Run-To-Run Variability (Figures 2.9-2.11)

Three independent realizations of Model 1 were simulated for the case u_p=1.0 km s^{-1}. Independent but statistically equivalent initial conditions were obtained by extracting atomic positions from instantaneous system observations separated by 0.5 ps at the end of the final equilibration trajectory and selecting for each sample new atomic velocities drawn from the P=300 K Maxwell distribution. The shock speeds u_s and collapse times t_c obtained for the three realizations (trials) are collected in Table 2.3.

Figure 2.9 presents three spatially resolved statistical measures of instantaneous run-to-run variability among the three trials, all evaluated at the instant t=t_c+5.0 ps. The top and bottom rows contain results for temperature and pressure, respectively. The left-hand column contains the mean values of local T or P among the three trials at a given location (y,z) in the samples. The center column shows the associated standard deviations,

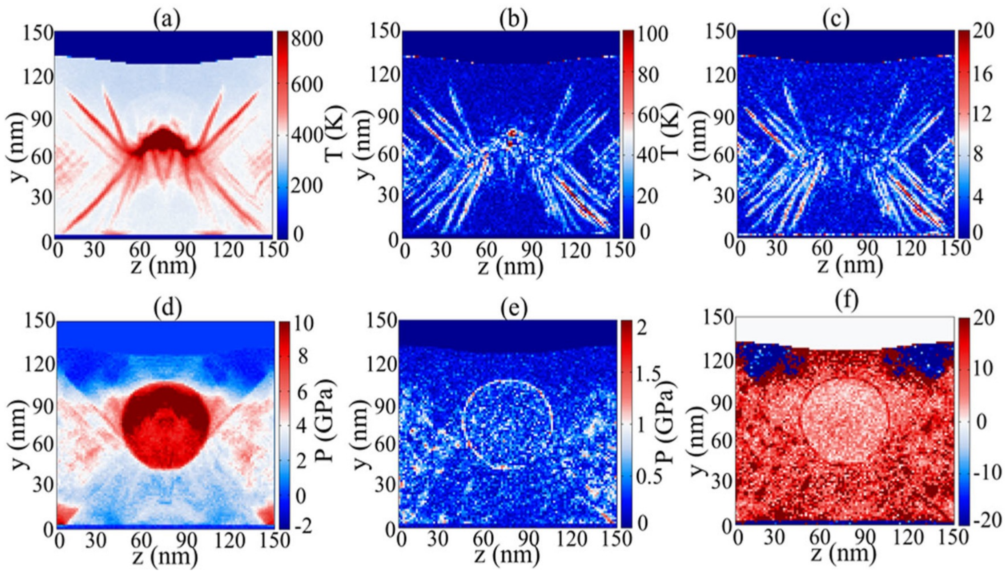

Figure 2.9: For Model 1 and u_p=1.0 km s^{-1} at t=t_c+5.0 ps, mean (left), standard deviation (center), and PRSD (right) among the three trials. Top: temperature. Bottom: pressure.

$$\sigma_\zeta(y,z) = \left\{ \frac{1}{3} \sum_{i=1}^{3} [\zeta_i(y,z) - \tilde{\zeta}(y,z)]^2 \right\}^{1/2} \tag{2.1}$$

where ζ= T or P and ζ is the associated mean value. The right-hand column presents percentage relative standard deviations (PRSDs), $[\sigma_\zeta(y,z)/\tilde{\zeta}(y,z)] \times 100\%$. Regions of large σ_ζ in the center column indicate locations where the local ζ-states differ most from one trial to the next. In the σ_ζ result for temperature [panel (b)], large ($\approx$100 K) σ_T values highlight different detailed shear-band patterns among the samples. With the exception of the distinct narrow ring of large σ_P (one to several GPa) corresponding to the instantaneous CSW radius, the result for pressure [panel (e)] is relatively featureless, mainly exhibiting fluctuations of magnitude $\sigma_P \approx$1 GPa. Note that the PRSDs weight the localσ_ζ values by the local mean values ζ. We observe that for both T [panel (c)] and P [panel (f)] the maximum PRSD values anywhere in the sample domain are less than $\approx$20%, and much smaller over most of it for T.

	Trial 1	Trial 2	Trial 3
u_s	5.94 $\pm$0.03^a	5.93 $\pm$0.06	6.01 $\pm$0.06
t_c	26.8	27.0	27.0

Table 2.3: Shock speeds u_s (km s^{-1}) and instants of maximal pore closure t_c (ps) for three independent realizations of Model 1 with u_p=1.0 km s^{-1}.

---

[a] *standard error of regression.*

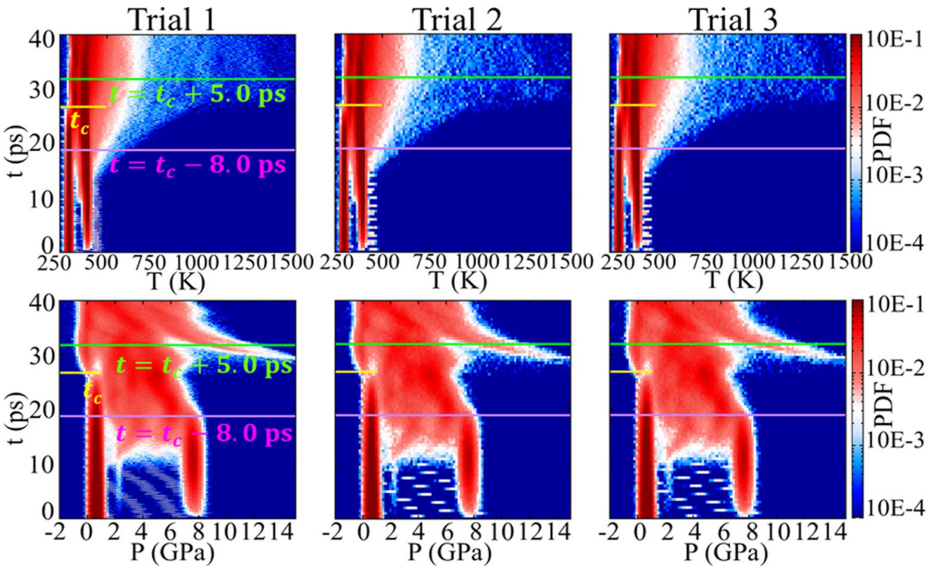

Figure 2.10: For three trials of Model 1 with u_p=1.0 km s^{-1}, TD-PDFs for temperature (top row) and pressure (bottom). Times for the instantaneous PDFs in Figure 2.11 are indicated by horizontal lines.

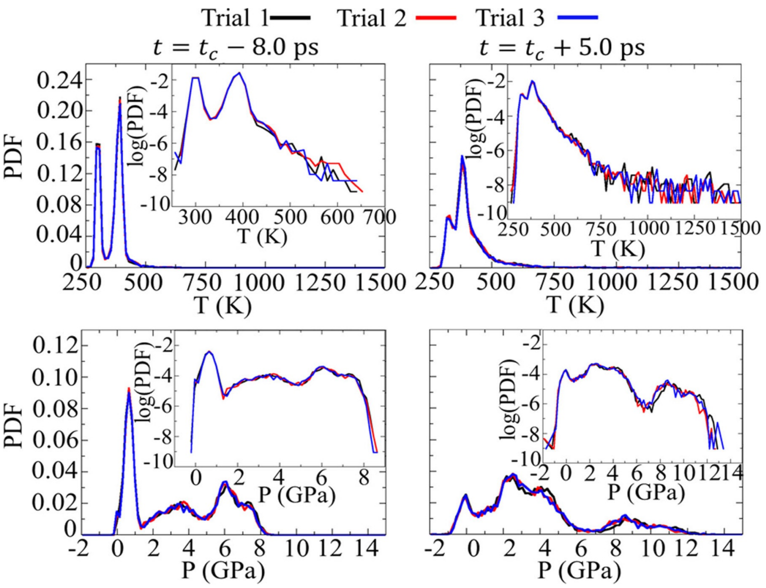

Figure 2.10 presents TD-PDFs for temperature (top row) and pressure (bottom) for the three trials (left-to-right). The results among the trials are almost indistinguishable. Fig. 2.11 presents instantaneous PDFs for temperature (top row) and pressure (bottom), with all three trials superposed, at the times t=t_c-8.0 ps (left) and t_c+5.0 ps (right). In all four cases, the superposed distributions are practically identical across the entire intervals.

2.5 Discussion

We observe little sensitivity to sample thickness for the natural orientation, as shown in Secs. 2.4.1 and 2.4.2.1. The bulk shock speeds and maximal pore-closure times for Models 1 (5 nm) and 2 (10 nm) in Table 2 are almost identical for the two cases, as are the pore area vs. time results for them in Fig. 2.4(a), for both impact speeds u_p. Snapshots of spatial distributions of local temperatures and pressures for Models 1 and 2 in the samples during and after pore collapse, shown in the first two columns of Figs. 2.2 and 2.3, reinforce this conclusion; the results for the thin and thick samples are so similar as to be practically indistinguishable, although the supporting animations suggest some subtle cell-thickness effects in the wake of shock passage. Analysis of the TD-PDFs for T and P, and probability slices extracted from them at selected instants, in Figs. 2.5 and 2.6 further support this conclusion.

By contrast, for 10 nm thick samples with differing quasi-2D transverse orientations (Models 2 and 3) discussed in Secs. 2.4.1 and 2.4.2.2, differences are apparent. Although the shocks speeds agree to within uncertainty (Table 2), differences in collapse mechanism, shear-band patterns, and CSW properties are evident in the snapshots for spatial distributions of local T and P in the samples during and after collapse (cf. the two rightmost columns in Figs. 2.2 and 2.3), and even more so in the supporting animations. It is unsurprising that the collapse of pores, oriented differently in the anisotropic crystal structure, would occur somewhat differently. However, the most salient difference is that whereas Model 2 collapses almost completely for u_p=0.5 km s^{-1}, Model 3 does not [Figs. 2.2, 2.3 and 2.4(b)]. Differences are also visible in the TD-PDFs and especially the instantaneous PDFs in Figs. 2.7 and 2.8.

The assessment of run-to-run variability for Model 1 impacted at u_p=1.0 km s^{-1} largely confirms the anticipated outcome for samples of the sizes considered here (≈11.6 million atoms for Model 1, see Table 1). Although the detailed shear-band patterns in the samples differ from one realization to the next, the overall behaviors are, in fact, very similar among them. The results for pore area vs. time for the three trials are identical to within the thickness of the line style used to plot them [Fig. 2.4(c)]. Results for both the TD-PDFs in Fig. 2.10 and the probability slices extracted from them in Fig. 2.11 are equivalent across the trials. Collectively, these results lead us to conclude a single large-scale MD simulation can be analyzed and interpreted with good confidence, in the sense that an otherwise identical simulation started from a different random-number seed would not yield a practically different result.

Some caveats are required. Although designed systematically, our thickness and orientation study only considers two sample thicknesses for a single transverse quasi-2D sample orientation (Models 1 and 2) and a single sample thickness for two transverse orientations (Models 2 and 3).

As noted in Sec. 2.3.2.1, the natural orientation chosen for the thickness study may represent a "simplest" case with respect to anticipated 3D effects, based on recent MD studies of dislocation slip systems and energetics in β-HMX by Picu and co-workers [114] which used effectively the same force field as here. It is also possible that simulations for much thicker samples would yield notably different collapse behaviors, perhaps more so away from the collapse zone and with increasing effects at longer times.

Although the natural and GCCM orientations studied are "very different", they yield field-level results for pore collapse that are not drastically different. It is however possible that simulations of pore collapse based on other, approximately constant-thickness (010)-oriented, GCCM-discovered generalized unit cells would identify transverse orientations (and therefore pore-axis directions) for which analogous quasi-2D pore-collapse behaviors are quite different from those for the two orientations studied here.

All of the preceding begs the question: What are the practical implications of the present study for head-to-head comparisons between MD and continuum mesoscale predictions for pore collapse? Sewell, Udaykumar, and co-workers have performed such comparisons for the case of shock-induced collapse of cylindrical pores (quasi-2D for MD, circular in the continuum calculations) for TATB [50] (1,3,5-triamino-2,4,6-trinitrobenzene) and β-HMX [84] and for an ellipse-shape pore in β-HMX [119]. All of these studies employed isotropic continuum material descriptions that were informed by MD to varying degrees. For the case of β-HMX with a circular pore, Das *et al.* [84] considered a systematic hierarchy of five continuum models with increasing levels of fidelity to MD. The limiting cases were an elastic-perfectly plastic strength model with the oft-used Kraut-Kennedy melting curve T_{melt}=$T_{melt}(P)$ and constant shear modulus (in essence, the material model from Refs.[20], and [120]); and a strain-, strain-rate, and temperature-dependent Johnson-Cook J2 (JC-J2) strength model due to Springer [121], with a (much steeper) melting curve due to Kroonblawd and Austin[63] obtained from MD using effectively the same force field as in the present study and a pressure-dependent shear modulus due to Pereverzev and Sewell [21] also obtained from MD using precisely the same force field as here. The MD simulations were performed using Model 1 from the present study; (010)-oriented shocks in a 5-nm thick sample with the natural orientation and pore axis parallel to $\boldsymbol{a}$. (In fact, the analyses shown here for Model 1 were performed using data generated in connection with the Das *et al.* study.) Successive replacement of the elastic-perfectly plastic strength model with the JCJ2 form and of the Kraut-Kennedy melt curve with the Kroonblawd-Austin prediction led to drastic changes in the continuum pore-collapse behavior. The MD-continuum comparison based on the "best" continuum model was closest for u_p=2.0 km s^{-1}, "good" for 1.0 km s^{-1}, and "reasonable" for u_p=0.5 km s^{-1}. This trend is unsurprising; accurately capturing the detailed, anisotropic material physics in the continuum description becomes increasingly important as the shock strength decreases. However, the fact that results for a single quasi-2D MD transverse sample orientation were treated as 'ground truth' against which the continuum predictions were assessed was a point of abiding concern. Comparing the sensitivity of the continuum predictions of Das *et al.*. with respect to material model with the differences that arise among MD predictions in the present study suggests, provisionally, that uncertainties in continuum mesoscale material model form and parameterization outweigh those arising due to choice of quasi-2D MD sample thickness and transverse crystal orientation, and certainly outweigh those arising from run-to-run variability among independent but statistically equivalent realizations of the shock in the MD.

2.6 Conclusion

We report all-atom non-reactive MD simulations of shock-induced pore collapse in quasi-2D samples of (010)-oriented β-HMX containing an initially 50nm diameter cylindrical pore at the center. The simulations were performed using a reverse-ballistic geometry for impact speeds u_p=1.0 and 0.5 km s^{-1} and were designed as a platform for determining the sensitivity of the predictions to (1) sample thickness along the thin direction in the periodic sample and (2) sample crystallographic orientation transverse to the shock direction in the quasi-2D domain. This was accomplished by comparing results obtained for three system setups (Models 1–3) that differ systematically with respect to these parameters. The focus is on field-level results, to assess the practical effects of the underlying molecular- and crystal-scale differences among the models on temperature and pressure distributions in the samples during and after pore collapse.

Models 1 and 2 correspond to the same transverse crystal orientation but differ in thickness (5nm vs. 10nm). The results for the 'natural' orientation studied are highly insensitive to the sample thickness at both impact speeds.

Models 2 and 3 both employ 10nm thick samples but differ significantly in transverse crystal orientation. The results reveal a minor effect on the shock speed and modest effects on spatio-temporal distributions of local temperature and pressure in the sample during and after collapse, with greater differences for the lower impact speed u_p=0.5 km s^{-1}. Although the collapse mechanisms for the two models are broadly similar, a significant qualitative difference is that whereas the pore in Model 2 (and 1) collapses nearly completely under the 0.5 km s^{-1} impact, for Model 3 it does not. Although not a goal of the present study, it is of interest to understand the molecular-scale fundamentals that underlie the difference.

For the case of Model 1 with u_p=1.0 km s^{-1}, simulations were performed for three independent but statistically equivalent realizations of the system, to assess run-to-run variability. Although each trial yielded slightly different shear-band patterns emanating from the collapse zone, the underlying phenomenology of the collapse events is clearly consistent among them. Results for the time-dependent probability distributions for temperature and pressure are, for all practical intents, identical across the trials.

Chapter 3

MOLECULAR DYNAMICS-GUIDED MATERIAL MODEL FOR THE SIMULATION OF SHOCK-INDUCED PORE COLLAPSE IN β-1,3,5,7-TETRANITRO-1,3,5,7-TETRAZOCANE (β-HMX)

3.1 Abstract

Material models for single-crystal β-HMX are systematically examined in the context of continuum pore-collapse simulations. Continuum predictions using five different isotropic material models are compared head-to-head with molecular dynamics (MD) predictions for a 50 nm cylindrical pore in β-HMX subject to a range of shock strengths. Shock waves were generated using a reverse-ballistic configuration, propagating along [010] in the MD simulations. The continuum models are improved hierarchically, drawing on temperature- and pressure-dependent MD-derived material parameters. This procedure reveals the sensitivity of the continuum predictions of pore collapse to the underlying thermophysical models. The study culminates in an MD-calibrated isotropic rate- and temperature-dependent strength model, which includes appropriate submodels for the temperature-dependent melting point of β-HMX [63], pressure-dependent shear modulus [21], and temperature-dependent specific heat, that produces continuum pore-collapse results similar to those predicted by MD. The resulting MD-informed model should improve the fidelity of simulations to predict the detonation initiation of HMX-based energetic materials containing micrometer-scale pores.

3.2 Introduction

Detonation initiation in energetic materials (EMs) depends on physical processes at spatiotemporal scales ranging from molecular (nm, fs–ps) through microstructural (μm, ns) to macroscale (mm,μs). A predictive computational model for the shock response of an EM therefore needs to incorporate key thermal-mechanical-chemical mechanisms active across these scales. A key requirement for a physically correct continuum model is that it implicitly captures the thermophysical processes leading to the ignition of chemical reactions at hotspots, which are localized regions of high temperature, pressure, and possibly strain rate [122],[123] in the microstructure of the material (i.e., at the mesoscale). Hotspot ignition and growth rates are key inputs in the development of meso-informed multi-scale models for ignition and the initiation of detonation in energetic materials [124],[125],[126],[127],[128]. Among various candidate hotspot formation mechanisms, the shock-induced collapse of pores is thought to be one of the more important routes under moderate to high shock-strength conditions [123],[129],[130]. Recently, the evolution of hotspots due to pore collapse has been simulated and meso-informed surrogate models for reaction rates have been obtained [131],[132],[133]. For hotspot models to correctly capture the mesoscale physics in condensed-phase heterogeneous EMs, the mechanics of crystal deformation and chemical reaction rates need to be correctly represented across wide intervals of pressure, temperature, and strain rate. In this work, material models for one widely studied EM, 1,3,5,7- tetranitro-1,3,5,7-tetrazocane (HMX), are refined using results of tandem molecular dynamics (MD) and continuum simulations of pore collapse.

HMX is the energetic component in several plastic-bonded explosives (PBXs) [134]. It exhibits three pure crystal polymorphs α, β, and γ among which the β polymorph is the thermodynamically stable form (monoclinic, P2_1/n space group, two molecules per unit cell) at standard ambient conditions [135],[136]. The physical and chemical properties of β-HMX required for an accurate mesoscale model have been studied extensively using both experimental [46],[49],[63],[76],[114],[134],[135],[136],[137], [138],[139],[140],[124],[58],[141],[142], and theoretical [24],[38],[47],[73],[109],[143],[144],[145],[146],[147], [148],[149],[150],[151] approaches. A review of the recent literature for pore collapse in HMX suggests that the most commonly used material models are an elastic-perfectly plastic model [123],[152] with parameters drawn from Menikoff and Sewell; [120],[153], a rate-dependent isotropic plasticity model [121] based on the experiments of Dick and co-workers; [154],[155] and anisotropic crystal plasticity models by Austin *et al.* [156],[157] Kroonblawd and Austin [63], and Koslowski and co-workers [18], with model parameters informed by MD simulations. Material models used in continuum calculations need to take into consideration not only the accuracy of predicted material dynamics, but also the length and time scales involved and the desired quantities of interest.

Selection of material models for pore-collapse and energy-localization studies, particularly for the construction of chemical reaction models based on large ensembles of pore-collapse simulations [131],[158], must be made with care. Material models must yield accurate measures of pore collapse and hotspot ignition and growth in reactive, highly resolved mesoscale simulations while keeping those simulations computationally feasible. Although crystal plasticity models [18] are computationally intensive, isotropic J2-plasticity models [121],[159],[160] are straightforward to implement and computationally economical. Provided that such models are shown to correctly predict the pore-collapse dynamics and the resulting temperature and pressure fields, they can be useful for constructing homogenized reaction rate models from ensembles of high-resolution pore-collapse simulations [131],[158]. In the present study, we seek to examine several isotropic J2-based elastic-plastic strength model variants for β-HMX and arrive at a baseline model that correctly describes the physics of pore collapse over a range of shock strengths. In determining how well continuum models capture the physics of pore collapse and hot spot formation, the key challenges are to (1) obtain a benchmark that can be compared to continuum predictions of pore collapse over a range of shock strengths and (2) determine model coefficients that produce physically realistic pore-collapse modes, including temperature and pressure fields during and following collapse.

Material models for β-HMX can be derived from physical experiments [18],[26],[136],[153],[154],[161],[162],[163],[164],[165]. However, visualization of pore collapse and extraction of spatially resolved fields of important quantities such as temperature from experiments remains challenging [164],[165],[166]. Visualization and quantitative comparisons between simulations and experiments can be accomplished only under specific conditions and for limited materials. For example, in recent work [167], a head-to-head comparison between experimentally visualized pore collapse and analogous mesoscale continuum predictions was per- formed for PMMA (polymethylmethacrylate), a non-reactive and transparent polymeric material. The continuum calculations were performed using an isotropic rate-dependent plasticity model. Good agreement between experimental and simulation results was obtained for the collapse rate and spatial features of the collapsing pore. However, even for a "simple" material such as PMMA, it is still difficult to measure the temperature and pressure fields from experiments due to equipment limitations [167].

An alternative approach that allows for a more comprehensive head-to-head comparison is to assess continuum simulations of pore collapse against MD predictions, treating MD as ground truth. This has been done recently by several authors for energetic crystals including 1,3,5-triamino-

2,4,6-trinitrobenzene (TATB) [50],[111] and HMX [18],[63]. Head-to-head comparisons between continuum and MD predictions due to Zhao *et al.* [50] for TATB brought to light the extent to which traditional continuum models replicated the pore-collapse modes and property fields obtained from MD simulations. Although MD provides detailed (atomically resolved) information about the evolution of the system in space and time, treating MD predictions as ground truth for benchmarking continuum predictions requires some justification and attention to *caveats*. Fundamentally, MD relies on the classical approximation. That is, the time evolution of the system through phase space is governed by the Newtonian equations of motion rather than the time-dependent Schrödinger equation. The implication is that inherently quantum mechanical phenomena such as zero-point energy constraints and tunneling are absent. Similarly, the specific heat in an isochoric-isoenergetic (NVE) MD simulation will be practically independent of temperature and density (classical equipartitioning), whereas quantum mechanically it will be a strong function of both of those intensive variables, with a value of zero at 0 K and approaching the classical limit from below only as the temperature becomes large (i.e., temperatures on the order of 2000 K for organic substances containing large numbers of C–H, N–H, or O–H covalent bonds). Therefore, except in the case of very strong shocks, the shock temperature predicted using NVE-MD will be lower than would obtain in the corresponding quantum mechanical system. Given the exponential dependence of reaction rates on temperature, MD predictions for chemically reactive systems must be interpreted with particular caution. Another concern is the accuracy of forces used to propagate the equations of motion. Empirical force fields, and even approaches for which the forces are calculated using electronic-structure methods [168], are imperfect. In addition, MD simulations are severely limited in terms of practically accessible system sizes (sub-micrometer) and simulated times (sub-nanosecond for large systems). All-atom MD simulations of molecular substances containing more than a few tens of millions of atoms are rare, meaning that MD simulations of pore collapse are typically limited to quasi-two-dimensional (quasi-2D) domains of sub-micrometer edge lengths in the plane of the problem and only several nanometers in the thin direction. This limits the pore sizes that can be studied "routinely" to ≈100 nm diameter or less. Analogous remarks apply to the spatial density of other defects, such as dislocations, that can be modelled explicitly. Despite these concerns, MD results can provide reasonably adequate benchmark information if care is taken to restrict both the molecular and continuum setup conditions to physical settings and spatiotemporal scales for which MD is deemed to be reliable.

In the present study, we perform simulations of pore collapse in β-HMX, comparing continuum predictions obtained using SCIMITAR3D [167],[169],[159],[170],[126] to MD results obtained using

LAMMPS [55]. The objective is to develop continuum material models that closely capture the physics of pore collapse as obtained from, and on the same spatiotemporal scale as, MD. Chemistry is excluded in all cases. Starting with a baseline elastic-perfectly plastic material model for β-HMX, with model forms and parameters taken from Menikoff and Sewell [120],[153], we systematically "upgrade" the model toward an improved description that captures rate-dependent plasticity, thermal softening, pressure-dependent melting temperature from MD [63], and pressure-dependent mechanical properties also informed by MD [21],[63]. This hierarchy of material models provides insights into which aspects of the physics are captured (or not) by the separate sub-model forms and parameter values that together comprise a material model. Differences among predictions using different material models also indicate the sensitivity of the physics of pore collapse to variations in specific properties of the material. The end point of the current study is the development of an isotropic continuum material model that produces physically realistic qualitative and quantitative results for pore collapse in HMX.

The remainder of the article is structured as follows. In Sec. 3.3, the continuum and MD models and formulations are described. Section 3.4 presents the results of the study; a systematic and hierarchical upgrade path starting from the baseline material model is adopted to examine the sensitivity of the continuum results to various aspects of the material model. Finally, in Sec. 3.5, we present conclusions from the study and point to directions for future investigations.

3.3 Methods

3.3.1 Continuum Model

The continuum model used to compute high-velocity impact-induced pore collapse in β-HMX, implemented in the Eulerian multi-material dynamics code SCIMITAR3D, is presented briefly in this section; further details can be obtained from previous works [126],[169],[171]. The mass, momentum, and energy conservation equations were cast in the Eulerian framework. The interface between solid HMX and the pore (treated as vacuum in both the continuum and MD simulations) was embedded in the Cartesian grid and tracked using the levelset method [172]. The ghost-fluid method [169] was used to impose appropriate boundary conditions at the material–pore interface. The conservation laws and the material models for HMX are described in Secs. 3.3.1.2 and 3.3.1.3, respectively.

3.3.1.1 Physical scenario and boundary conditions

The overall simulation scenario is shown in Fig. 3.1. The MD and continuum calculations were performed for nearly identical setups. Although the MD calculations were quasi-2D (see Sec. 3.3.2.2 below), the continuum calculations were fully 2D; that is, planar under plane-strain assumption. Based on a mesh-resolution sensitivity study, which is available in the appendix, the mesh spacing used for all of the continuum simulations reported below is 0.125 nm, corresponding to 400 mesh points across the initial 50 nm pore diameter. The boundary conditions in the MD and continuum simulations were also similar but not identical. The MD simulations employed standard three-dimensional (3D) periodic boundary conditions in which atoms that exit one face of the monoclinic shape primary simulation cell re-enter the cell at the opposite face without modification of the velocities. In continuum simulations, reflective boundary conditions were applied at all edges and corners of the rectilinear computational domain. A reflective boundary condition at y=2.8 nm emulates the rigid and stationary piston in the MD. The reflective boundary condition used at the left and right boundaries approximates the periodic boundary condition used in MD simulations due to the symmetry of the computational domain with respect to the vertical centerline. Preliminary computations were performed to establish that the differences between the continuum and MD setups did not lead to substantial differences in behavior on the time scale of the calculations.

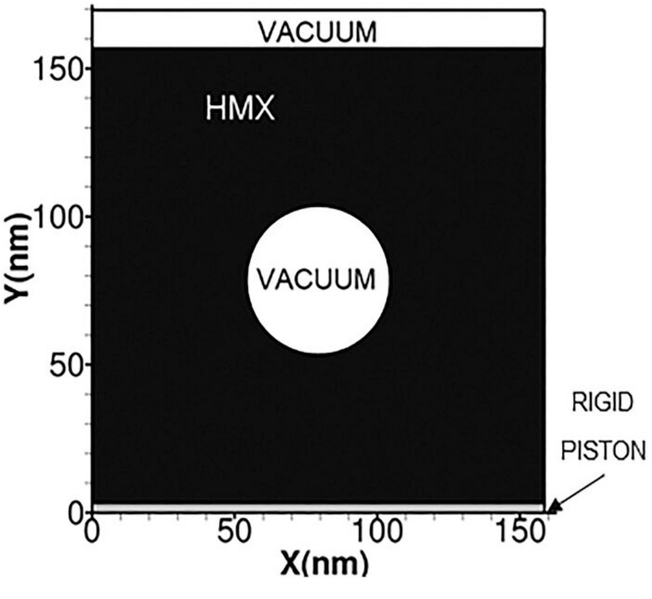

Figure 3.1: Geometric setup for MD and continuum simulations. A square sample of HMX containing an initially circular pore (cylindrical in the case of MD) at the center undergoes reverse-ballistic impact with impact speed u_p onto a rigid, stationary piston at the bottom of the sample.

3.3.1.2 Conservation laws

In the continuum treatment, the mass, momentum, and energy conservation equations, cast in the following Eulerian form, were solved,

$$\frac{\partial \rho}{\partial t} + \frac{\partial(\rho u_i)}{\partial x_i} = 0 \tag{3.1}$$

$$\frac{\partial(\rho u_i)}{\partial t} + \frac{\partial(\rho u_i u_j - \sigma_{ij})}{\partial x_j} = 0 \tag{3.2}$$

$$\frac{\partial(\rho E)}{\partial t} + \frac{\partial(\rho E u_j - \sigma_{ij} u_{ij})}{\partial x_j} = 0 \tag{3.3}$$

where ρ and u_i denote, respectively, density and velocity components; $E{=}e{+}\frac{1}{2}u_i u_i$ is the specific total energy; and e is the specific internal energy. The Cauchy stress tensor σ_{ij} is of the following form:

$$\sigma_{ij} = S_{ij} - p\delta_{ij} \tag{3.4}$$

where S_{ij} is the deviatoric stress tensor and p is the pressure.

3.3.1.3 Material models

Pressure was obtained from a Mie–Grüneisen equation of state (EOS) for HMX of the following form (Ref. [153]):

$$p = p_c(V) + \frac{\Gamma}{V}[e - e_c(V)], \tag{3.5}$$

where Γ is the Grüneisen coefficient and V is specific volume. The pressure p_c on the cold curve was fit to the third-order Birch–Murnaghan EOS [120],[173],

$$p_c = \frac{3}{2}K_0\left[\left(\frac{V}{V_0}\right)^{-\frac{7}{3}} - \left(\frac{V}{V_0}\right)^{-\frac{5}{3}}\right] \times \left[1 + \frac{3}{4}(K_0^{'} - 4)\left(\frac{V}{V_0}\right)^{-\frac{2}{3}} - 1\right], \tag{3.6}$$

where the coefficients K_0 and $K_0^{'}$ are the calibrated isothermal bulk modulus and its initial pressure derivative [122],[174], respectively, and v_0 is a reference volume.

The internal energy corresponding to the isothermal state was obtained from

$$e_c(V) = e_0 - \int_{V_0}^{V} p_c(V)dV, \tag{3.7}$$

where e_0 is a reference internal energy. The Grüneisen coefficient was represented as

$$\Gamma(V) = a + b\left(\frac{V}{V_0}\right), \tag{3.8}$$

where the coefficients a and b were calculated from the calibration factor Z [175] and zero-pressure Grüneisen parameter Γ_0 [176].

$$a = \Gamma_0 + b, \tag{3.9}$$

$$b = -Z. \tag{3.10}$$

The EOS parameters K_0, $K_0^{'}$, a, and b are given in Table 3.1 [153],[120].

The temperature, T, was obtained from

$$T(V, e) = T_0\left(\frac{V}{V_0}\right)^{\Gamma} + \frac{e - e_c(v)}{c_v}, \tag{3.11}$$

where T_0 is the reference temperature (298 K) and c_v is isochoric specific heat.

Parameter	Value
V_0	$\frac{1}{1900}$ m^3 kg^{-1}
K_0	16.5 G Pa
$K_0^{'}$	8.7
a	1.1
b	-0.2
c_0	5.265×10^{-7} K kg J^{-1}
c_1	3.073×10^{-4} K kg J^{-1}
c_2	1.831×10^{-1} K kg J^{-1}
c_3	4.194×10^{-4} K kg J^{-1}
θ	1

Table 3.1: EOS parameters used in continuum calculations.

The specific heat c_v in Eq. (3.11) is a key thermophysical quantity for hotspot formation, as the temperature reached after pore collapse is influenced by its value. In MD calculations, due to the underlying classical approximation, the effective c_v in the system is practically constant. On the other hand, in continuum calculations, a temperature-dependent c_v [120] is commonly used. To assess the suitability of these two different treatments of specific heat in continuum calculations, two different models for c_v were examined: a constant c_v (2359 J kg^1 K^1) corresponding to the value implicit in the MD simulations and a temperature-dependent form based on quantum chemistry calculations for HMX [120]. The temperature-dependent c_v is given by

$$c_v = \frac{\tilde{T}^3}{c_0 + c_1\tilde{T} + c_2\tilde{T}^2 + c_3\tilde{T}^3} \tag{3.12}$$

where $\tilde{T}$=T/θ(V). Here, $\theta(V)$ is the Debye temperature and has the following form:

$$\theta(V) = \theta_0\left(\frac{V_0}{V}\right)^a exp\left[\frac{b(V_0 - V)}{V}\right] \tag{3.13}$$

The constants c_0, c_1, c_2, and c_3 are given in Table 3.1 [120]. The functional forms for the two models for c_v are compared in Fig. 3.2(c).

The deviatoric stress components S_{ij} of solid HMX are evolved using the following equation:

$$\frac{\partial(\rho S_{ij})}{\partial t} + \frac{\partial(\rho S_{ij}u_k)}{\partial x_k} + \rho S_{ik}\Omega_{kj} - \rho\Omega_{ik}S_{kj} = \rho G(D^d_{ij} - D^{d,p}_{ij}), \tag{3.14}$$

where D^d_{ij} is the deviatoric component of the strain-rate tensor, Ω_{ij} is the spin tensor, $D^{d,p}_{ij}$ is the plastic component of the deviatoric strain-rate tensor, and G is the shear modulus of the material. Molten HMX is modelled as an inviscid liquid by setting S_{ij}=0 in any cell for which the temperature in HMX exceeds the melting point, based on the two melting curve models described four paragraphs below and depicted in Fig. 3.2(a). Eq. (3.14) was solved using a two-step operator-splitting algorithm [177]. First, the deviatoric stress was evolved assuming purely elastic deformation [i.e., setting $D^{d,p}_{ij}=0$ in Eq. (3.14)] in a predictor step. This was followed by a correction step to remap the predicted stress onto the yield surface using the radial return algorithm [178].

Two different representations of G were examined in the current calculations; a constant G (10 GPa) and an MD-based [21] pressure-dependent model given by the following equation:

$$G = -2.0543 \times 10^{-20}p^2 + 1.7531 \times 10^{-9}p + 7.89GPa. \tag{3.15}$$

The constant and pressure-dependent models for G are illustrated in Fig. 3.2(b), which also includes recent MD predictions [21] from which the pressure dependence was obtained.

The Johnson–Cook flow rule was employed, and the yield surface is defined as

$$f = S_e - \sigma_Y = 0 \tag{3.16}$$

where $S_e=\sqrt{\frac{3}{2}tr(S_{ij}S_{ji})}$ is the effective plastic stress and σ_Y is the yield strength of the material.

Two different isotropic models for yield strength were examined: a rate-independent elastic-perfectly plastic model and a rate-dependent Johnson–Cook model. Under the elastic-perfectly plastic assumption, σ_Y was set to a constant value of 0.26 GPa [153]. The rate-dependent Johnson–Cook model given in the following form (Ref. [121]) was used to capture the effects of strain hardening, strain-rate hardening, and thermal softening on the yield strength,

Parameter	Value
A	100.0 MPa
B	100.0 MPa
C	1.086
n	0.1
M	3
$\dot{\varepsilon_0}$	10^{-3} μs^{-1}
T_{ref}	298 K

Table 3.2: Johnson–Cook model parameters.

Here, ε_p is the equivalent plastic strain and $\dot{\varepsilon^*}{=}\dot{\varepsilon}/\dot{\varepsilon_0}$, where ε is the plastic strain rate and $\dot{\varepsilon_0}$ is a reference plastic strain rate; T is the temperature and T_{ref} is the reference temperature of the material; and A, B, n, C, and M are Johnson–Cook model coefficients. Values of these parameters are provided in Table 3.2 [121].

The parameter T_m in Eq. (3.17) is the melting point of HMX at a given pressure. The effects of two separate models for T_m on the results were examined. In one model, we used the Kraut–Kennedy relation [153],

$$T_m = T_{m0}\left(1+\alpha\frac{\rho-\rho_{ref}}{\rho}\right), \tag{3.17}$$

where the reference melting temperature is T_{m0}=551K. The constant α=1.533 was estimated based on the Lindemann law, and the reference density was set to ρ_{ref}=1900 kg m^3. The second model for T_m is due to Kroonblawd and Austin [63] based on MD simulations of the melt curve. It is of Simon–Glatzel form (Ref. [179]),

$$T_m = T_{m0}\left(1+\frac{\rho-\rho_{ref}}{a'}\right)^{(1/c')}, \tag{3.18}$$

where the reference pressure is p_{ref}=0. The quantities a' and c' are fitting parameters with values 0.305 GPa and 3.27, respectively [63]. Comparison of the melt-curve models for β-HMX in Fig. 3.2(a) shows that the MD-calibrated model due to Kroonblawd and Austin [63] predicts significantly higher T_m values than the Kraut–Kennedy model. The impact of this difference on predictions of pore collapse and hot spot formation is revealed in Sec. 3.4.

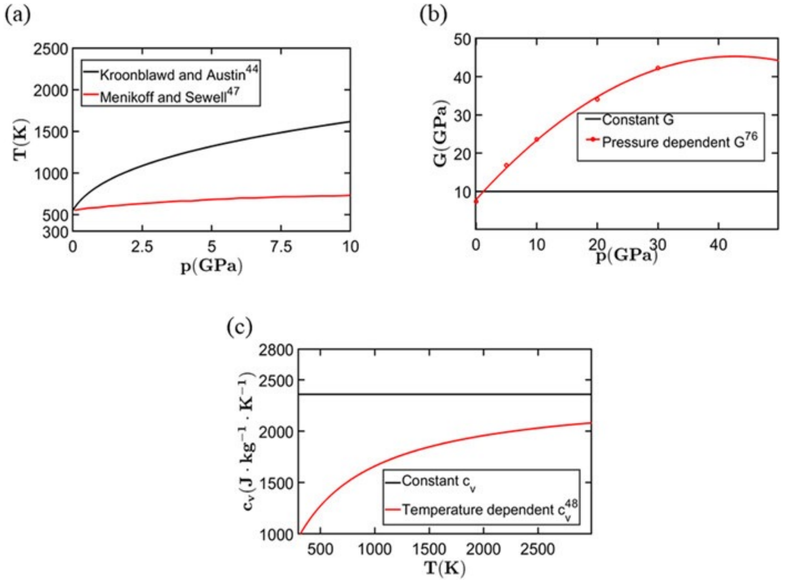

Figure 3.2: Models for (a) melting temperature T_m, (b) shear modulus G, and (c) specific heat c_v used in the continuum calculations.

3.3.1.4 Numerical algorithms and interfacial conditions

The conservation laws for mass, momentum, and energy [Eqs.(3.1)–(3.3)], along with the evolution of deviatoric stresses [Eq.(3.14)], were spatially discretized using a third-order essentially non-oscillatory shock-capturing scheme [180]. The time integration was performed using a third-order total-variation-diminishing Runge–Kutta scheme [181]. Narrow-band level set-based tracking [172] was used to sharply define and evolve material interfaces. The use of a level set function allows for the handling of large deformation of interfaces that occurs during pore-collapse events. The interfacial conditions between HMX and the pore surface were modeled by applying the free-surface conditions at the interface using a modified ghost-fluid method [169],[182]. Detailed descriptions of the numerical algorithms, level set implementation, and interface treatment are available in previous publications [169],[159].

3.3.2 MD Model

3.3.2.1 Force-Field

A variant of the nonreactive, fully flexible, all-atom force field originally developed by Smith and Bharadwaj [47],[44] was used in which covalent bonds, three-center angles, and wag angles are described using harmonic functions; dihedral angles are modeled as truncated cosine series; and non-bonded interactions between atoms in different molecules and between atoms in the same molecule but separated by three or more covalent bonds are modeled using the Buckingham-plus-Coulomb form. In addition to adjustments of N–O and C–H covalent bond-stretching force constants [46],[49],[48], a short-range non-bonded repulsion was added to the non-bonded interaction; see Ref. [50] for more details. A cut-off distance of 11.0 Å was used for repulsion, dispersion, and short-range Coulombic interactions. Long-range Coulombic interactions were computed using the particle–particle particle–mesh (PPPM) k-space method [51],[183] with the relative error in forces set to 10^{-6}.

3.3.2.2 Simulation cell setup and equilibration

The MD sample comprises a 5.3×152.6×150.4 nm^3 ($8\boldsymbol{a}\times146\boldsymbol{b}\times198\boldsymbol{c}$) quasi-2D monoclinic-shape primary cell with a 50 nm diameter cylindrical pore located at the center. Here, $\boldsymbol{a}$, $\boldsymbol{b}$, and $\boldsymbol{c}$ are the $P2_1/n$ lattice vectors predicted by the force field at 300 K and 10^{-4} GPa. The cylinder axis is parallel to the thin direction of the cell (i.e., parallel to $\boldsymbol{a}$). This particular orientation was selected to [73],[114] minimize 3D effects based on known β-HMX slip systems. The overall system contained 422,960 β-HMX molecules. A 10.0 nm vacuum region was added to one end of the primary-cell simulation domain along the shock direction ([010]) to reduce electrostatic inter- actions across the periodic boundaries. The mapping of the crystal frame to the Cartesian lab frame is $\boldsymbol{a}\|$x, $\boldsymbol{b}\|$y, and $\boldsymbol{c}$ in the +z space.

All MD simulations were performed using the LAMMPS [55] code with the velocity Verlet integrator [53]. The system was thermalized at T = 300 K in two steps. First, an isochoric-isoenergetic (NVE) simulation was performed for 1.0ps using a 0.1fs time step. During this stage, the system kinetic temperature T was computed every 10.0 fs and atomic velocities were rescaled to 300 K if $|T(t)\text{-}300\ \mathrm{K}| > 10$ K, that is, if the absolute difference between the instantaneous kinetic temperature (hereafter, temperature) and the target temperature was greater than 10 K. This was followed by 5.0 ps of isochoric-isothermal (NVT) simulation using the Nose–Hoover thermostat [116],[117] with a 0.2 fs time step and the thermostat coupling parameter set to 100.0fs; new atomic velocities were selected from the 300K Maxwell distribution every 1.0ps during the NVE integration to damp out acoustic waves emanating from the pore surface and the added vacuum region. Three-dimensional periodic boundary conditions were implemented in all simulations.

3.3.2.3 Shock Simulations

Shocks were generated using a reverse-ballistic configuration wherein a flexible sample containing 413456 β-HMX molecules impacted a rigid, infinitely massive piston composed of the same material. Molecules in the first three unit cells along $\boldsymbol{b}$ from the bottom of the cell (i.e., from y=0) were assigned to the piston, which consisted of 9504 molecules. Atomic velocities and forces for atoms in the piston were maintained at zero throughout the simulation. Three impact speeds, $\boldsymbol{u}_p$=0.5, 1.0, and 2.0 km s^1, were studied. The corresponding velocity vectors were added to the instantaneous thermal velocities of atoms in the flexible sample at the end of equilibration, resulting in a supported shock wave that traveled with velocity $\boldsymbol{u}_w$ parallel to the +y direction in the lab frame, that is, parallel to the [010] crystallographic direction. The shock velocity is $\boldsymbol{u}_s$=$\boldsymbol{u}_w$+$|\boldsymbol{u}_p|$ due to the reverse-ballistic configuration. Each shock simulation was continued until the sample length, measured along the vertical center line of the pore and expanding during shock release, increased to 110% of its value at maximum compression. The simulations ranged in length from 30 to 60 ps depending on impact speed. Atomic Cartesian positions, velocities, and stress tensor components were recorded at 100 fs intervals for post-processing.

3.3.2.4 Trajectory Analysis

Two-dimensional maps of system properties were computed following an approach similar to the one described in Ref. [50]. A virtual Eulerian (Cartesian) grid, with an edge length of 1.50 nm in the plane of the sample and extending all the way through the sample in the thin direction (5.3 nm), was superposed on the full computational domain taking proper account of periodic boundaries. Spatially resolved properties at a given time were calculated as described in Ref. [50] by assigning atoms to the appropriate cell in the grid and computing those properties based on the atoms in that cell. The reference timescale for non-dimensionalization, t^*, in both the continuum and MD calculations is

$$t^* = \frac{D}{u_s}, \tag{3.19}$$

where D is the initial pore diameter and u_s is the shock speed. The area of the pore as a function of dimensionless time t/t^* was calculated using the approach described in Ref. [50]. The shock speed in the MD calculations was determined using the method described in Refs. [93] and [184]. Specific equations used to compute the various MD system properties are described in Refs [93],[101],[184].

3.4 Results and Discussion

In this section, we systematically evaluate material models employed in the continuum calculations by comparing pore-collapse results head-to-head with MD predictions. The common aspects of the material models studied are that they are cast in the Eulerian isotropic J2-plasticity framework and employ the MD-derived Mie–Grüneisen EOS specified in Eq.(3.5). However, they differ in the models used to determine the yield condition Y in the plasticity model, the melting temperature T_m, the shear modulus G, and the specific heat c_v. The points of distinction among the five continuum models examined are summarized in Table 3.3 and are discussed below:

Model	Yield strength	Melt Curve	Shear Modulus	Specific heat
1	Constant	Kraut-Kennedy	Constant	Temperature dependent
2	**Strain rate and temperature dependent**[a]	Kraut-Kennedy	Constant	Temperature dependent
3	Strain rate and temperature dependent	**Kroonblawd-Austin**	Constant	Temperature dependent
4	Strain rate and temperature dependent	Kroonblawd-Austin	**Pressure dependent**	Temperature dependent
5	Strain rate and temperature dependent	Kroonblawd-Austin	Pressure dependent	**Constant (*classical*)**

Table 3.3: Distinctions among the continuum models.

[a] *The model component changed relative to the preceding row in the table is denoted using* ***bold-italic*** *font.*

- Model 1 is a simple elastic-perfectly plastic model. It conforms to model constants and forms that have been widely used. Discussion of the models and constants thereof can be found in Menikoff and Sewell [120],[153].
- Model 2 replaces the perfectly plastic flow assumption for Y with a strain-, strain-rate-, and temperature-dependent Johnson– Cook model [121].
- Model 3 is upgraded from model 2 by replacing the Kraut– Kennedy melt curve from Ref. [153] with the recently published MD-based melt curve due to Kroonblawd and Austin [63], based on (essentially) the same force field employed in the present study.
- Model 4 builds on model 3 by replacing the constant shear modulus in models 1–3 with a pressure-dependent form based on recently published MD results [21].
- Model 5 is the same as model 4 except the quantum-based temperature-dependent specific heat is replaced by the constant value corresponding to MD.

An important point to note is that submodel parameters not directly associated with passage from one model to the next were left unchanged. For example, when progressing from model 4 to model

5, only the specific-heat model was simplified from a quantum-based temperature-dependent form to a constant value corresponding to MD; numerical values of the parameters in the rate- and temperature-dependent yield model [Eq. (3.17)] were left unchanged. Results for all five models are compared to MD predictions for the case of the 1.0 km s^{-1} impact in Sec. 3.4.1. Results for models 1 and 4 are subsequently compared to MD predictions for the cases of 2.0 and 0.5 km s^{-1} impacts in Sec. 3.4.2.

3.4.1 Pore Collapse for the 1.0 km s^{-1} Impact

3.4.1.1 MD-based collapse

Molecular dynamics results for the 1.0 km s^{-1} impact are shown in Fig. 3.3. Panels (a) and (b) contain 2D maps (*contours*) of temperature and panels (c) and (d) show pressure, at two instants (t=23.0 and 35.0 ps) during and approximately 8 ps after pore closure. Panels (e) and (f) contain time-dependent probability distributions of temperature and pressure, respectively, in the sample.

The incident shock first reaches the upstream (i.e., bottom) pore surface at t=9.0 ps. After the wave passes the equator of the pore, the material in the vicinity of the pore surface and near the equator is extruded. The extruded material later forms two "proto-jets" [Fig. 3.3(a)] that flow symmetrically toward the downstream (i.e., top) pore surface at an angle of approximately |45°| relative to the horizontal. Finally, after reaching the downstream pore surface, the extruded material is deflected horizontally inward and collides at the vertical centerline of the pore, leading to complete collapse [panel (b)]. The observed non-smooth pore surface during collapse is due to the anisotropy of the β-HMX crystal, which is captured implicitly in MD simulations.

Intense shearing occurs in the extruded material in the vicinity of the pore, and "shear bands" grow into the shocked region symmetrically toward both the bottom and top of the sample at an angle of approximately |45°| from the horizontal. These shear effects are evident from the regions of elevated temperature ($\approx$1000 K) recorded in the shear bands in Figs. 3.3(a) and 3.3(b). A hotspot at approximately 2000 K forms when the pore collapses completely [panel (b)]. In addition, more shear bands develop independently in the material behind the shock [panel (b)] away from those that initiated at the pore surface.

Two-dimensional maps of pressure from the MD calculations are shown in Figs. 3.3(c) and 3.3(d). Prior to shock arrival at the pore, the "bulk" shock pressure is approximately 7.4 GPa. As the shock traverses the pore region, material between the piston and pore exhibits a drop in pressure due to material flow into the pore, and a rarefaction wave propagates into that region back toward the piston. While the extruded material flows into the pore, the rarefaction wave strikes the piston, leading to a weak reflected wave that propagates back into the shocked region [panel (c)]. Later, the pore collapse leads to a strong, approximately circular re-shock wave (*blast wave*) with a peak pressure of ≈20 GPa, located near the pore center, that subsequently expands outward [panel (d)].

Figures 3.3(e) and 3.3(f) contain, respectively, time-dependent probability distributions of temperature and pressure in the sample. These figures are useful to compare the MD results with continuum calculations as they provide a composite picture of the evolution of temperature and pressure fields as a result of pore collapse and its aftermath. Note that the probabilities are plotted using a logarithmic scale. The probabilities were calculated by imposing a virtual "Eulerian" 3D rectilinear grid onto the computational domain and assigning atoms to a particular grid cell at a given instant of analysis based on their locations at that time. The temperature and pressure for the set of atoms in the cell were calculated using atomic velocities and atomic stress tensor. The instantaneous center-of-mass motion of atoms in a given cell was removed from the atomic velocities prior to the temperature calculation. The cell edge lengths are 1.50×1.50 nm^2 in the plane of the problem and extend through the entire thickness of the computational domain (5.3 nm) in the thin direction. The resulting instantaneous temperatures and pressures at a given instant were coarse-grained into histogram bins of widths 20 K and 0.1 GPa, respectively, with normalization of the resulting distributions to unity at each instant of analysis. The numbers of bins in the histograms vary from one impact speed to another, due to the different intervals of temperature and pressure associated with different shock strengths.

The two vertical red strips at early times in Fig. 3.3(e) correspond to the initial bulk temperature (300 K) and the temperature of the material behind the shock but prior to the lead shock wave reaching the upstream pore surface (≈400 K). The formation and growth of the shear bands are indicated by the increasing probability of temperature values ranging from 400 to 1000 K beginning at t=13 ps. The probability of temperature greater than 1000 K becomes prominent starting from t=26 ps, corresponding to the complete collapse of the pore.

The probability distribution for pressure [Fig. 3.3(f)] exhibits features qualitatively similar to those for temperature. Note that the initially non-zero pressure of the material ahead of shock is due to the kinetic term included in the atomic stress tensor, which was not corrected for the mass flow. The pressure increases abruptly to 7.4 GPa behind the shock but prior to shock arrival at the upstream pore wall. The broadened probability of the two pressure values and the noticeable probability of p=3 and 5 GPa before t=10 ps are artifacts of the spatial resolution (i.e., the Eulerian grid size used for property calculation is wider than the shock-front width). At t=10 ps, the wave front has reached the upstream pore surface, causing an increase in probability of pressure values between 2 and 8 GPa. The analogous feature is also observed in Fig. 3.3(e), where the probability of temperature values between 300 and 400 K increases upon shock arrival at the upstream pore surface. The collision of the extruded material at t=26 ps causes a jump in pressure and hence the probability of high-pressure values, which is later relieved by the blast wave.

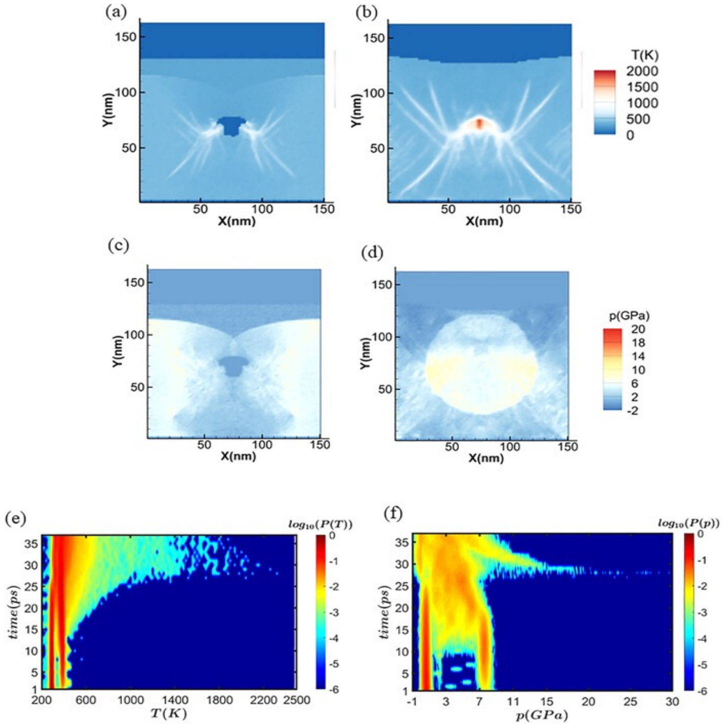

Figure 3.3: For the 1.0 km s^{-1} impact, MD predictions of temperature (top row) and pressure (middle row) contours at two instants during and after pore collapse. From left to right, the columns correspond to t=23.0 ps [panels (a) and (c)] and t=35.0 ps [panels (b) and (d)]. Panels (e) and (f) contain time-dependent probability distributions for temperature and pressure, respectively, with probabilities shown on a logarithmic scale.

3.4.1.2 Continuum-based collapse

In this section, we compare, for the 1.0 km s^{-1} impact, the pore collapse and thermo-mechanical energy localization results for continuum models 1–5 against the MD predictions presented just above. Figures 3.4 and 3.5 contain contours of temperature and pres- sure, respectively, for the five continuum models; and Fig. 3.6 shows the corresponding time-dependent probability distributions of tem- perature and pressure in the (continuum) computational domain. These figures are counterparts to MD predictions shown in Fig. 3.3.

Columns in Figs. 3.4 and 3.5 correspond to time instants t=23 and 35 ps and the rows to models

1 (top row) through 5 (bottom row). Note that the time instants for the plots in Figs. 3.4 and 3.5 are identical to those used in the MD analysis, allowing for a head-to-head comparison with Fig. 3.3. The performance of the continuum models can be assessed against the corresponding MD results from different standpoints, viz., material dynamics around the pore during and following collapse, the pore-collapse profile, the rate of pore collapse as measured by the pore area, and the resulting hotspot temperature and pressure fields following collapse. Each of these aspects is discussed below.

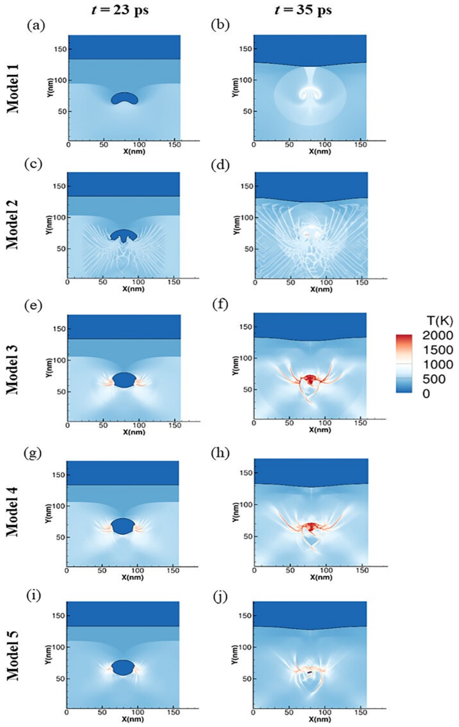

Figure 3.4: (a)–(j) For the 1.0 km s^{-1} impact, contours of temperature at two instants during and after pore collapse for the five continuum models.

As seen in Table 3.4, differences in material properties cause continuum shock speeds to differ slightly from the MD value and indeed from one continuum model to the next. For example, model 1 underpredicts the lead shock speed slightly compared to MD. Models 2–5 show better agreement with MD for shock velocities, with models 3–5 providing the closest match. For all models, the rarefaction wave emanating from the pore surface as the lead shock wraps around it during collapse (Fig. 3.5, left column) and the strong blast wave slightly after pore closure (right column) are evident in the pressure contours. The wave-front positions and patterns resulting from the continuum models show progressive improvement, compared to MD, from model 1 to model 4. It can be seen that model 5, which employs a constant specific heat in place of the temperature-dependent specific heat used in models 1–4, yields results for temperature and pressure that are in lesser agreement with MD than observed for model 4.

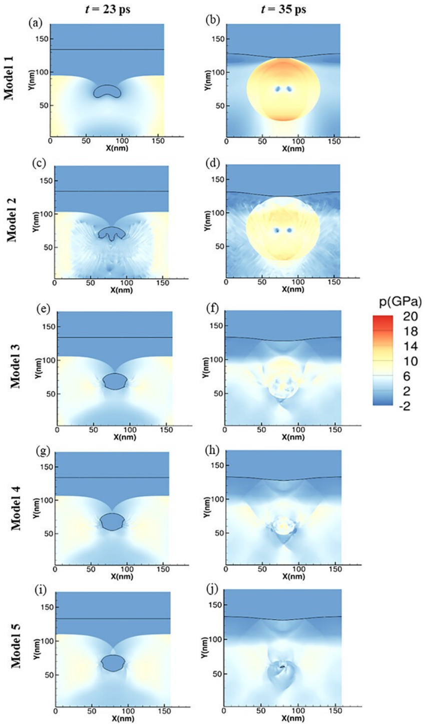

Figure 3.5: (a)–(j) For the 1.0 km s^{-1} impact, contours of pressure at two instants during and after pore collapse for the five continuum models.

In general, the results indicate that the shock dynamics are quite different across the models, particularly with regard to the blast wave following pore collapse (right-hand column of Fig. 3.5). The hotspot temperature fields are also quite different across the models, as seen from the right-hand column in Fig. 3.4.

Figures 3.4(a) and 3.5(a) show that model 1 predicts the formation of a distinct material jet at the lower end of the pore as the shock travels across the pore. This general behavior has been reported in several previous studies [167],[126],[185] and is indicative of a pore-collapse mechanism dominated by hydrodynamic forces. Model 2 (second row) relaxes the perfectly plastic deformation constraint. It predicts the formation of two jets at the bottom prior to the collapse of the pore [Fig. 3.4(c)], in contrast to the single jet seen in Fig. 3.4(a) for model 1. The strain- and strain-rate-dependent hardening of the material in model 2 prevents the formation of a single high-speed jet from the bottom of the pore. Rather, shear bands are nucleated at the surface of the pore and cause shear localization at the expected 45° orientation, leading to shear- induced heating of the material; this shear localization is completely absent for the elastic-perfectly plastic description of model 1. Thermal softening effects weaken the material in the regions of localized plastic heating. The combined effect is

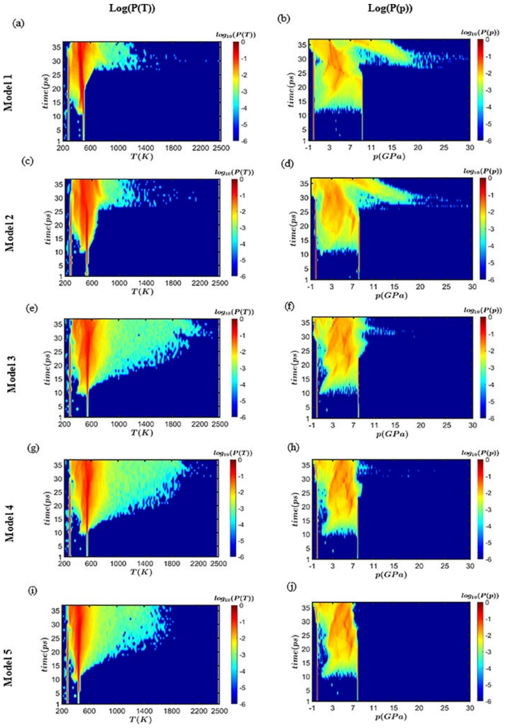

Figure 3.6: (a)–(j) For the 1.0 km s^{-1} impact, time-dependent probability distributions of temperature (left column) and pressure (right) for the five continuum models, with probabilities shown on a logarithmic scale.

an involution of material in regions of shear localization leading to two re-entrant jets observed in Fig. 3.4(c). The thermal softening effects are dominant in model 2 due to the use of the Kraut–Kennedy model [153] for the melting curve of HMX, which predicts that the melting point only increases by ≈150 K (from ≈550 to ≈700 K) as the pressure is increased from 0 to 10 GPa [see Fig. 3.2(a)]. This enhances thermal softening in the strain-rate- and temperature-dependent plasticity model used in model 2 (and also models 3–5, albeit with the much steeper Kroonblawd–Austin [63] melt curve). The enhanced thermal softening in the material, and its interplay with the strain/strain-rate hardening [186],[187], leads to the development of the network of shear-bands observed in Figs. 3.4(c) and 3.4(d). However, shear-localization increases the temperature of HMX beyond the melting point in model 2 and the material within the shear band undergoes a phase transition to an inviscid liquid, which inhibits further shear localization. Consequently, the temperatures within the shear bands predicted by model 2 [Fig. 3.4(d)] are significantly lower than for model 3 [Fig. 3.4(f)] and model 4 [Fig. 3.4(h)], for which the melting temperature is much higher. Further discussion of the overall thermo-mechanical behavior of the models and their impact on the observed pore profiles during collapse and the post-collapse temperature and pressure fields for the 1 km s^{-1} impact can be found in Sec. 3.4.1.3.

Model 3 (third row) replaces the Kraut–Kennedy melt curve with the MD-based model due to Kroonblawd and Austin [63]. The salient difference between the two melt curves is a decidedly stronger pressure dependence in the Kroonblawd–Austin model when compared to the often-used Kraut–Kennedy relation, as seen in Fig. 3.2(a). In comparison to model 2, the contour plots for temperature and pressure for model 3, Figs. 3.4(e) and 3.5(e), respectively, show that with model 3 the material at the bottom of the pore resists jet formation. Instead, two proto-jets form on the sides of the pore after the lead shock has traveled across the pore. Model 3 predicts a pore-collapse mechanism similar to the corresponding MD case; the pore-collapse profile is remarkably different from model 2 indicating that the model for melting temperature has a strong effect on the collapse process. In particular, the spatial density of shear bands is significantly lower in model 3 [compare Figs. 3.4(f) and 3.4(d)], but the extent of heating in the shear bands that do form is greatly increased in the case of model 3. The implication is that the model for the melt curve has a significant influence on the intensity of hot spots in the HMX material.

Model 4 (fourth row) employs the pressure-dependent shear modulus [Eq. (3.15)] obtained from MD simulations [21] in place of the constant value (G=10 GPa) used in models 1–3; cf. Fig. 3.2(b). Predictions from model 4 for the pore-collapse profile, the hot spot temperature field, and the post-collapse pressure field are qualitatively similar to those for model 3. Comparison of Figs. 3.5(f) and 3.5(h) shows that model 4 results in a slightly lower post-collapse pressure relative to predictions from model 3. Thus, the pressure dependence of G does not appear to significantly influence the pore collapse and hot spot behavior.

Model 5 (fifth row) implements the constant specific heat value, c_v=2359 J kg^{-1} K^{-1}, corresponding to classical mechanics (as in MD) instead of the temperature-dependent model [cf. Fig. 3.2(c)]. Consequently, the bulk temperature behind the shock predicted by model 5 is lower ($\approx$459 K) compared to model 4 ($\approx$550 K). The lower post-shock temperature obtained from model 5 implies that the thermal softening of HMX is lower in this case; therefore, the yield strength calculated from the rate-dependent model [Eq. (3.17)] is higher. This results in different shear-banding patterns predicted by models 4 and 5, as can be observed in Figs. 3.4(h) and 3.4(j). In addition, Figs. 3.4(h) and 3.4(j) show that the temperature in the shear bands is lower for model 5 than for model 4.

The pressure fields obtained from model 5 are shown in Figs. 3.5(i) and 3.5(j). Midway through the collapse event (at t=23 ps), the distribution and magnitude of pressure predicted by models 4 and 5 are in good agreement [Figs. 3.5(g) and 3.5(i)]. However, the post-collapse pressures predicted by model 5 [panel (j)] are lower than the values predicted by model 4 [panel (h)].

Interestingly, post-collapse temperatures for model 5 are also significantly different from those obtained using MD. In particular, model 5 fails to capture the high temperatures (≈2000 K) predicted by the MD calculation. This may seem counter-intuitive, as model 5 employs a specific-heat model that corresponds to MD. However, the parameterization of Eq. (3.17)—i.e., the strain-, strain-rate-, and temperature-dependent yield stress model—was performed in conjunction with temperature-dependent specific heat. This under-scores the importance of an internally consistent parameterization to achieve optimal agreement between the continuum simulations and experimental or MD data; one should not exchange one sub-model for another without careful consideration of the indirect effects associated with doing so. For example, although the replacement of the Kraut–Kennedy melt-curve model with the Kroonblawd–Austin model upon passing from model 2 to model 3 also leads to a significant difference in the predictions, the melt-curve model does not directly affect the calculated temperature field as the specific-heat model clearly does. The melt-curve model only affects the yield-stress value indirectly by determining the temperature at which the strength drops abruptly to zero. Therefore, the effects of the specific heat [compare Figs. 3.4(h) and 3.4(j)] and the melt curve [compare Figs. 3.4(d) and 3.4(f)] on the predicted pore collapse and hot spot temperature are quite different, reflecting their different influences on the strength of the material.

Figure 3.6 contains time-dependent probability distributions of temperature and pressure for the five continuum models. The left-hand column is for temperature and the right-hand column for pressure; vertically from top to bottom, the rows correspond to model 1 through model 5. To compute probability distributions, high-resolution field data from the continuum calculations were first interpolated to a coarser 2D Eulerian grid of cell size 1.50×1.50 nm^2, as done for the MD calculation. The same histogram bin widths as for the MD analysis—20 K and 0.1 GPa—were used to compute the normalized distributions of temperature and pressure from the interpolated field data. Thus, these plots can be compared directly with the corresponding MD results in Figs. 3.3(e) and 3.3(f).

Comparison of the sequences of temperature and pressure contours in Figs. 3.4 and 3.5, respectively, shows that both models 1 and 2 predict similar *magnitudes* of temperature and pressure, albeit with strikingly different mechanisms of collapse as discussed above. This observation is further supported by the time-dependent probability distributions of temperature and pressure for models 1 and 2, as shown in Figs. 3.6(a)–3.6(d). Although the distributions are distinguishable for model 2 vs model 1, they are qualitatively similar. Prior to pore closure, the maximum pressure for model 1 is approximately 1 GPa higher than for model 2. The highest post- collapse pressure is ≈30 GPa for both models; and, for temperature, 2500 K for model 1 and 2200 K for model 2, both of which occur momentarily at the time of collapse in a small region.

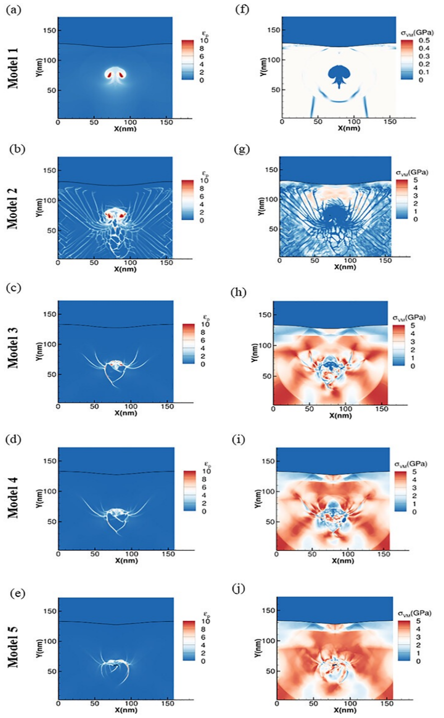

Figure 3.7: (a)–(j) For the 1.0 km s^{-1} impact, contours of post-collapse effective plastic strain (left column) and von Mises stress (right column) for the five continuum models at t=35 ps. .

Comparison of the time evolution of the probability distributions of the temperature and pressure obtained from MD and model 1, in Figs. 3.3(e) and 3.3(f) and Figs. 3.6(a) and 3.6(b), respectively, further delineates the differences in the results obtained from these two descriptions. Figures 3.3(f) and 3.6(b) show that model 1 predicts a greater probability of high post-collapse pressures compared to MD; this is due to the stronger post-collapse blast wave that results from the near-hydrodynamic pore collapse for model 1. The probability distributions for model 2 [Figs. 3.6(c) and 3.6(d)] are quite similar to model 1, save for some small differences on the high- temperature and high-pressure tails of the distributions, particularly at post-collapse times (i.e., after 25 ps).

The evolution of the distributions of temperature in MD [Fig. 3.3(e)] and the continuum calculation for model 2 [Fig. 3.6(c)] shows that model 2 fails to capture much of the heating of HMX above ≈1400K predicted by MD. Despite the rate-dependent plasticity model and accompanying shear-band formation, model 2 produces temperature distributions quite similar to the hydrodynamics-dominated behavior obtained using model 1.

This is due to the greater thermal softening of the material for model 2, resulting from the combination of the Johnson–Cook model for yield stress and the Kraut–Kennedy model for the melt curve. As seen in Fig. 3.2(a), the Kraut–Kennedy model yields low values of melting temperature, leading to the majority of the post-shock HMX being in the liquid phase and therefore displaying a nearly hydrodynamic response during pore collapse. A qualitative comparison of the sequence of temperature contours obtained from MD in Figs. 3.3(a) and 3.3(b) and the continuum model 2 in Figs. 3.4(c) and 3.4(d) shows that the network of shear bands predicted by MD calculations and model 2 are significantly different. Model 2 yields a larger number of shear bands, but the temperatures within them are lower than seen in MD. The large number of shear bands may lead to weaker localization due to shear, whereas, as observed below [Fig. 3.4(f)], model 3 results in fewer but stronger shear bands with higher temperatures, in better agreement with MD.

As seen in Figs. 3.4(e) and 3.4(f), in the case of model 3 there is a remarkable change in the pore-collapse profile and post-collapse temperature distributions. The contour plot for temperature at t=35.0 ps in Fig. 3.4(f) shows that model 3 predicts significantly higher temperatures within the shear bands compared to model 2 [Fig. 3.4(d)]. The time evolution of the temperature distribution in Fig. 6(e) shows that model 3 yields a significantly larger area of the material with higher temperatures (T>1400 K) than models 1 and 2; also, these high-temperature regions appear at earlier times (≈20 ps) in the case of model 3. On the other hand, the pressure contour at t=35.0 ps presented in Fig. 3.5(f) shows that model 3 predicts a weaker post-collapse blast wave than models 1 and 2. This is because model 3 predicts a lower velocity of the material jets in the collapse region than models 1 and 2 for reasons elaborated in Sec. 3.4.1.3. The results obtained from model 3 are found to be in better agreement with the MD results; in particular, Figs. 3.4(e) and 3.4(f) show that model 3 predicts the emergence and growth of shear bands that are similar to the MD results in Figs. 3.3(a) and 3.3(b). In addition, the time-dependent probability distribution of temperature obtained from model 3 [Fig. 3.6(e)] is found to match the MD results in Fig. 3.3(e).

Model 4 yields time-dependent temperature distributions that are statistically similar to those for Model 3, Figs. 3.6(e) and 3.6(g), both during and after pore collapse. However, small differences are observed between the patterns of the shear bands produced by model 4 [Fig. 3.4(h)] when compared to model 3 [Fig.,3.4(f)]. The contour plots for pressure in Figs. 3.5(e)–3.5(h) and probability distribution functions for pressure in Figs. 3.6(f) and 3.6(h) show that models 3 and 4 produce similar pressure distributions. Thus, in passing from model 3 to model 4 i.e., changing the model for shear modulus from a constant value to an MD-derived pressure- dependent function the results for pore-collapse mechanisms and energy localization are not altered significantly.

Changing the specific heat model from the temperature-dependent description to the constant, classical value i.e., model 5 leads to temperature and pressure distributions that deviate significantly from MD predictions, especially in the high-temperature and high-pressure regions, as can be seen by comparing Figs. 3.3(e) and 3.3(f) with Figs. 3.6(i) and 3.6(j).

Fewer shear bands are predicted for continuum models 3–5 compared to model 2 because of the reduced thermal softening effects in the latter. The Kroonblawd–Austin [63] melt curve [Eq. (3.19)] used in models 3–5 predicts much higher melting points for HMX away from p=1 atm than does the Kraut–Kennedy [153] relation [Eq. (3.18)] used in models 1 and 2 [see Fig. 3.2(a)]. Specifically, strain/strain-rate hardening of the solid material persists to higher temperatures (>600 K) in models 3–5 compared to model 2 due to the steeper melting curve in the former which increases the temperature at which the material transforms from a solid with strength to an inviscid liquid with a shear modulus of zero. This interplay among the strength and melting sub-models explains, at least in part, the observed differences in shear banding between model 2 and model 3.

The above observations regarding the pore-collapse profiles and temperature and pressure fields resulting from the five different continuum models can be explained in terms of the evolution of the strength of the material associated with different models. Understanding of the deformation of HMX under applied shock loading is facilitated by examining the effective plastic strain (ε_p) and von Mises stress (σ_{VM}) contours shown in Fig. 3.7 at a time instant following void collapse, viz., t=35 ps. As seen in the figure, the strain and stress fields change noticeably as the material models are changed. The perfectly plastic model 1 [Figs. 3.7(a) and 3.7(f)] yields only limited regions of large plastic strains. The fluid material in the vicinity of the pore undergoes rapid deformation, registering large values of ε_p close to the pore-collapse site [Fig. 3.7(a)]. This is expected, as the constant yield strength (0.26 GPa) in model 1 is significantly lower than the ambient post-shock pressure (≈9 GPa). Contours of σ_{VM} in Fig. 3.7(f) show that the deviatoric stresses rise to the yield stress of the material (0.26 GPa) nearly everywhere in the shocked HMX. The same figure panel indicates nearly zero deviatoric stress in the pore-collapse region and small, approximately constant (0.26 GPa) deviatoric stresses throughout the rest of the domain. Thus, model 1 produces a predominantly hydrodynamic response of the material as reflected by the jetting mechanism of void collapse. In contrast to model 1, inclusion of rate dependency in model 2 produces melt cracks in which the bulk of plastic deformation is concentrated [Fig. 3.7(b)]. The strength of the material in this network of melt cracks falls to zero as indicated by the network of low σ_{VM} regions in Fig. 3.7(g).

Comparison of the σ_{VM} contours obtained from models 1, 2, and 3 [Figs. 3.7(f)–3.7(h), respectively] shows that model 3 predicts significantly higher deviatoric stresses in the shocked material compared to models 1 and 2. This is because models 1 and 2, which use the Kraut–Kennedy melt curve, produce extensive post-shock regions that exceed the melting temperature, leading to a loss of mechanical strength in the network of shear bands (melt cracks). By contrast, in model 3, which uses the Kroonblawd–Austin melt curve for which the melting temperatures lie well above the Kraut–Kennedy curve [Fig. 3.2(a)], the compressed material is strain-hardened and resists rapid deformation. This can be seen by comparing the contours of ε_p for models 1, 2, and 3 in Figs. 3.7(a)–3.7(c), respectively. Note also that, because of the higher yield stresses in model 3, the accumulation of plastic strain occurs within a smaller number of shear bands (compared to model 2) emanating from the sides of the pore. Subsequently, the thermally softened material on the sides of the pore undergoes plastic deformation and "flow" into the pore. Therefore, in contrast to models 1 and 2, model 3 results in the formation of involutions from the sides of the pore, in agreement with the pore-collapse profile seen in the MD calculations. Thus, the higher melting temperatures obtained from the Kroonblawd–Austin model [Fig. 3.2(a)], combined with the rate- dependent plasticity model, lead to higher values of deviatoric stresses [Fig. 3.7(h)] and more confined regions of melting in the material. This inhibits the deformation of the material and causes the departure from the near-hydrodynamic behavior displayed by models 1 and 2. Finally, as shown by the strain and stress contours in Figs. 3.7(d) and 3.7(i), respectively, the pressure-dependent shear modulus used in model 4 has little effect on strain and stress localization relative to model 3. Similarly, the change in specific heat model [model 5, Fig. 3.7(j)] results in only modest changes in the magnitude and distribution of deviatoric stresses. In summary, the primary factors influencing the deformability, the mode of void collapse, and shear localization are the rate-dependent plasticity model and the Kroonblawd–Austin melt curve.

To illustrate the influence of the material models on the rate of pore collapse, Fig.3.8 shows plots of variation of the scaled pore area A/A_0 with scaled time t/t^* [see Eq. (3.20)] for different continuum models (solid curves) and compares them to MD predictions (open circles). The time evolution of A/A_0 in Fig. 3.8 shows that models 1 and 2 predict similar rates of pore collapse, despite significant differences in pore-collapse profiles and shear-banding behavior. The best agreement with MD is obtained using model 3.

3.4.1.3 Summative discussion for the 1.0 km s^{-1} impact

The preceding discussions in connection with Figs. 3.3–3.8, all for the case of 1.0 km s^{-1} impact, provide a variety of measures to evaluate the five continuum models tested in this work. Although the pore-area time histories in Fig. 3.8 are "similar" for five different continuum models and are in fair agreement with the MD prediction, the pore-collapse rate alone does not reveal the hotspot characteristics predicted by a particular material model. Examining the temperature and pressure

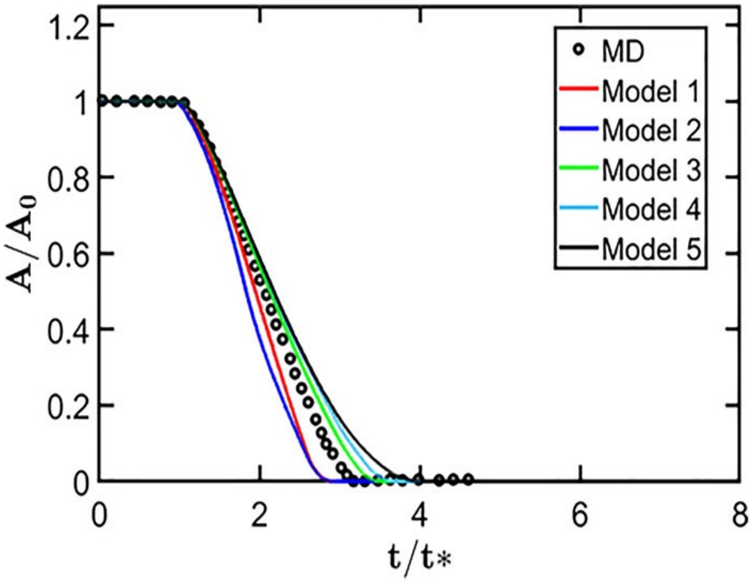

Figure 3.8: For the 1.0 km s^{-1} impact, scaled pore area vs scaled time (t/t^{*}) during pore collapse, calculated using MD and the five continuum models.

fields during and following pore collapse allows for a better assessment of the mechanics of collapse, as well as the nature and intensity of the hotspot. In this regard, the assessment of the models is better performed by collective inspection of Figs. 3.4–3.6 and 3.8 and comparing them with the MD counterparts in Figs. 3.3 and 3.8. Collectively, the temperature and pressure fields, time-dependent probability distributions, evolution of pore-collapse profiles, and qualitative modes of pore collapse (i.e., hydrodynamic jetting vs lateral proto-jet closure) are useful for assessing the accuracy of the physics predicted by a given material model. The presence or absence of shear bands and the associated energy localization are also significant, as the hotspots evolve in distinct patterns due to the presence of such shear bands. Taking all of these factors into consideration, models 3 and 4 most closely reproduce the pore-collapse and hotspot behavior observed in MD calculations. Although model 4 produces the best agreement with MD in terms of pore-collapse profiles and mode, shear-band patterns, and temperature and pressure fields, it predicts a slower pore-collapse rate compared to MD and model 3 (which yields the collapse rate closest to the MD prediction). However, because model 4 includes the same physics as model 3 but with the addition of MD-derived pressure-dependent shear modulus, we deem model 4 as the one that is most representative of the physics of pore collapse displayed in the “ground truth” MD predictions.

3.4.2 Pore Collapse for 2.0 and 0.5 km s^{-1} Impacts

Having established above that model 4 yields pore-collapse profiles, instantaneous temperature and pressure fields, time-dependent probability distributions for temperature and pressure, and pore-area time histories that are in closest overall agreement with MD predictions, we now examine the differences in performance between MD and continuum models 1 and 4 for stronger (2.0 km s^{-1}) and weaker (0.5 km s^{-1}) impacts.

3.4.2.1 2.0 km s^{-1} impact

For the strong impact case, contour plots of temperature and pressure, obtained from the MD and continuum models at t=16 and 22 ps, are presented in Figs. 3.9 and 3.10, respectively. The bulk temperature and pressure of shocked HMX computed from MD and continuum models are tabulated in Table 3.4. For the 2.0 km s^{-1} impact, the post-shock pressure is ≈23 GPa. It is expected that in this case pressure dominates the deviatoric stresses. Figures 3.9(a) and 13.0(a) show that, for MD, as the shock wave travels past the pore, the material near the upstream pore surface is accelerated into the pore due to the high pressure behind the shock, and two proto jets form prior to pore collapse. The MD calculations reveal a collapse profile that is approaching that of a hydrodynamic jetting mode. However, even at this high impact velocity, there is evidence of heating in regions of localized shear that emanates from the vicinity of the pore surface back into the compressed material, as seen in Figs. 3.9(a) and 3.9(b). The temperature field around the pore-collapse region shows a maximum of ≈2500 K and an extensive surrounding region with compressed material at a lower temperature (≈1000 K) in the areas that have undergone heating due to localized shear. The pressure contours in Fig. 3.10(b) show that a strong blast wave (≈25 GPa) emanates from the location of collapse, as expected for a pore-collapse mode dominated by hydrodynamic jetting.

We now examine the differences between continuum predictions based on model 1 and model 4 for the high-velocity impact scenario to contrast the behaviors of a rate-independent elastic-perfectly plastic model and a rate-dependent model in this regime. Figures 3.9(c) and 3.10(c) show that model 1 predicts the formation of a classical single jet at the upstream surface of the pore as the shock wave travels past it. As seen in the contour plot of temperature in Fig. 3.9(d), model 1 predicts a high temperature (≈2500 K) within a small region at the downstream pore surface after the collapse of the pore, similar to the MD results in Fig. 3.9(b). The pressure contour in Fig. 3.10(d) exhibits a post-collapse blast wave predicted by model 1 that is reasonably similar to the MD prediction in Fig. 3.10(b). However, model 1 fails to predict shear localization and heating near the pore-collapse

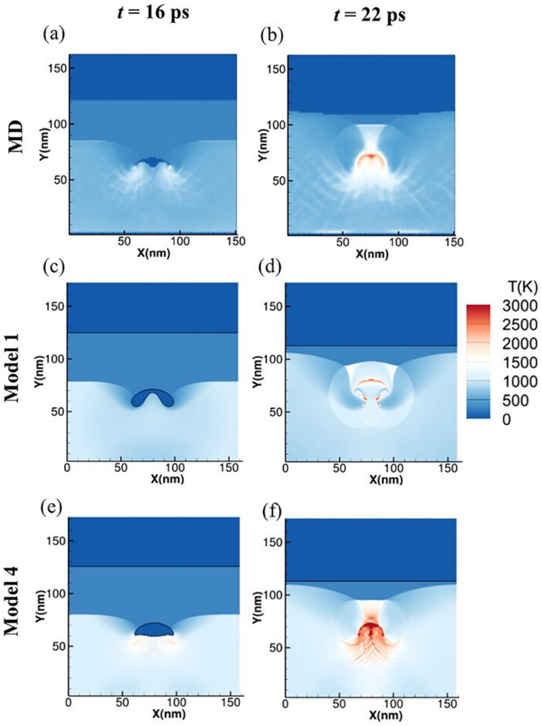

Figure 3.9: (a)–(f) For the 2.0 km s^{-1} impact, contours of temperature at two instants during and after pore collapse. From top to bottom, the rows correspond to MD, continuum model 1, and continuum model 4.

site [Fig. 3.9(d)] observed in MD simulations [Fig. 3.9(b)]. The strength of the post-collapse blast wave predicted by model 1 [Fig. 3.10(d)] is also stronger than that obtained in MD [Fig. 3.10(b)], whereas model 4 predicts a blast wave [Fig. 3.10(f)] that is in better agreement with MD. Figure 3.9(e) shows that, as for MD, continuum model 4 predicts the formation of two proto-jets during pore collapse and heating of HMX in regions of localized shear [Figs. 3.9(e) and 3.9(f)]. However, the overall temperature predicted by model 4 is higher compared to MD, both in the pore-collapse region (≈3000 K) and in the shear bands (≈2300 K).

Time-dependent probability distributions of temperature and pressure for MD and continuum simulations are compared in Fig. 3.11. Overall, the distributions of temperature and pressure predicted by both continuum models resemble the MD results. However, a careful comparison of Figs. 3.11(a) and 3.11(c) shows that model 1 predicts a lower probability for temperatures of >1000 K than observed from the MD calculations. This is because model 1 fails to capture the heating in shear bands. By contrast, model 4 predicts a higher probability for reaching temperatures of >1000 K compared to MD [Fig. 3.11(e)]. This is likely due to the higher stiffness of model 4, such that visco-plastic dissipation is over-represented by model 4. However, as shown in Fig. 11, the pressure field obtained from model 4 [Fig. 3.11(f)] agrees better with the distribution obtained from MD [Fig.

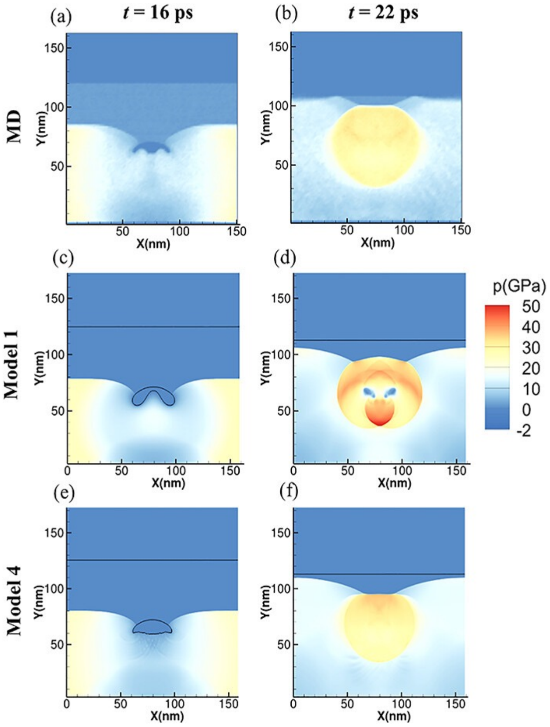

Figure 3.10: (a)–(f) For the 2.0 km s^{-1} impact, contours of pressure at two instants during and after pore collapse for MD, continuum model 1, and continuum model 4.

3.11(b)] than does model 1 [Fig. 3.11(d)].

3.4.2.2 0.5 km s^{-1} impact

Results for temperature contours at times t=32 ps and t=42 ps resulting from 0.5 km s^{-1} impact are shown in Fig. 3.12 for MD and continuum models 1 and 4. Figs. 3.12(a) and 3.12(b) show that the MD pore-collapse mechanism is dominated by visco-plastic behavior, with localized shear bands that originate near the pore surface and extend laterally into the bulk material. The pore- collapse rate is much slower compared to the 1.0 and 2.0 km s^{-1} impact cases. Unlike for higher impact-velocity cases, the pore closes through the formation of involutions at the equator of the pore. Elevated temperatures (≈500 K) are observed only within the shear bands.

The temperature contours obtained from models 1 and 4 are presented in Figs. 3.12(c) and 3.12(d) and Figs. 3.12(e) and 3.12(f), respectively. Model 1 predicts that the upstream pore surface undergoes rapid deformation under compression and leads to the complete collapse of the pore in 40 ps. Therefore, even at this low impact velocity, model 1 predicts a weakly hydrodynamic (jet) mode of pore collapse and fails to capture the influence of plastic dissipation. Even at 0.5 km s^{-1}, the shock pressure, ≈3 GPa, is significantly higher than the constant yield stress value

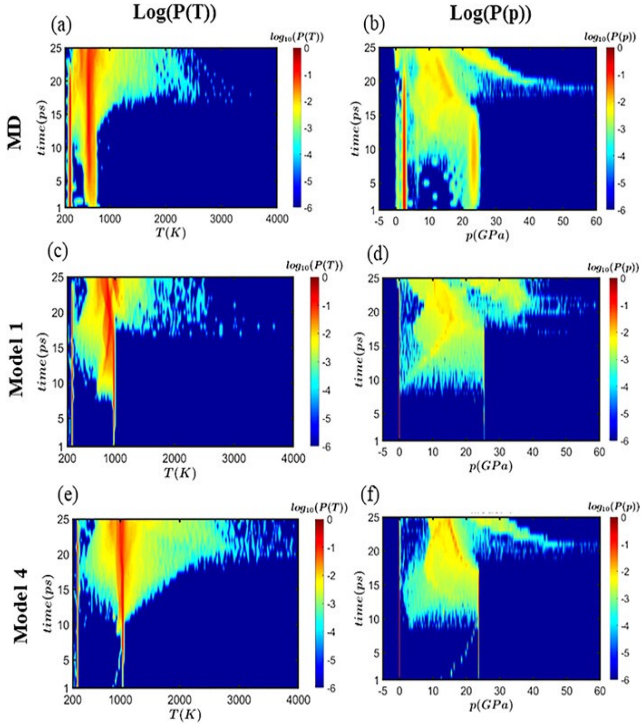

Figure 3.11: (a)–(f) For the 2.0 km s^{-1} impact, time-dependent probability distributions for temperature (left column) and pressure (right) during and after pore collapse, with probabilities shown on a logarithmic scale. The top, middle, and bottom rows correspond to MD, continuum model 1, and continuum model 4, respectively.

of 0.26 GPa, leading to negligible strength effects in the material and therefore a hydrodynamic pore-collapse mode. The misrepresentation of the pore-collapse mechanism by model 1 leads to predictions that are significantly different from MD, with a comparatively intense hotspot (>1000 K) formed when the pore collapses [Fig. 3.12(d)]. By contrast, the MD prediction shows that the highest temperature during pore collapse is ≈700 K and occurs within the shear bands. The time-dependent probability distributions for temperature and pressure predicted by MD and the continuum models are compared in Fig. 3.13. Figures 3.13(c) and 13.3(d) show that model 1 predicts a rapid increase in the temperature and pressure at around 40ps due to the hydrodynamic collapse of the pore, whereas Figs. 3.13(a) and 3.13(b) show that such a sudden increase in the temperature and pressure is absent in MD predictions. It is clear that model 1 leads to significantly different distributions of temperature, pressure, and localized energy for the 0.5 km s^{-1} impact case.

Figures 3.12(e) and 3.12(f) show that the pore-collapse mechanism changes drastically with model 4, which predicts that the pore does not collapse completely for u_p= 0.5 km s^{-1}. The strain/strain-rate hardening in model 4 strengthens het material so that it resists deformation. Figures 3.12(e) and 3.12(f) reveal an increase in temperature in the shear bands on the sides of the pore

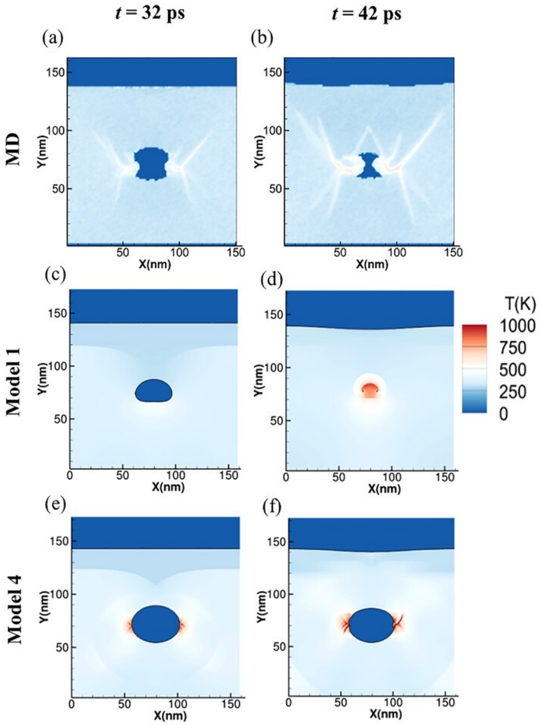

Figure 3.12: (a)–(f) For the 0.5 km s^{-1} impact, contours of temperature at two instants for MD, continuum model 1, and continuum model 4.

due to plastic heating. Comparison of time-dependent probability distributions of temperature in Figs. 3.13(a), 3.13(c), and 3.13(e) reveals that model 4 predicts significantly higher temperatures than MD and model 1. This is due to the greater stiffness of model 4, which leads to increased shear localization and hence higher temperatures in regions of concentrated shear.

The time evolution of pore area predicted by models 1 and 4 at u_p=0.5 km s^{-1} is shown in black in Fig. 3.14. Model 4 predicts that the pore area decreases to a minimum value at $t/t^* \approx$3 that is approximately 60% of its initial value, A_0, and then retracts to approximately $0.8A_0$. The rate of retraction is initially low but increases markedly for times greater than $t/t^* \approx$4.5. The pore never collapses completely, in distinct contrast to MD predictions. The *failure* to collapse is a direct consequence of the interplay among strain/rate hardening and thermal softening in the strength model and the properties of the melting curve, as discussed above. The *retraction* can be explained as follows: When the incident shock reaches the free surface at the top of the sample, it reflects as a rare- faction wave. The rarefaction wave results in tensile stresses along the shock direction that propagate back into the sample, leading to acceleration of the retraction behavior. Another factor contributing to the discrepancy between the results obtained from MD and continuum calculations is the isotropic material description in the continuum models. Obviously, isotropic continuum models cannot be expected to capture robustly the anisotropic material behavior of HMX. For strong shocks e.g., the 2.0 km s^{-1} impact, with the 1.0 km s^{-1} impact serving as an intermediate case the pressure and inertial flow largely overhelm the strength yielding a hydrodynamic-like response even in the MD. Under such conditions, anisotropy and other aspects of the detailed material physics exert relatively minor influences, although their presence is observable in the shear-band patterns and hot-spot shape in the MD results. Consequently, for strong shocks even an isotropic material model for HMX in the continuum calculations yields results that are similar to the MD predictions, *provided that the thermal softening and shear-rate dependencies are represented in the continuum model.* This is an insightful and important finding from our study. By contrast, for weak shocks e.g., the 0.5 km s^{-1}1 impact the mechanism of pore collapse is dominated by the detailed material physics, as is obvious in the MD predictions. An isotropic model cannot possibly capture these subtleties. The time evolution of the scaled pore area for different models are compared in Fig. 3.14 for all three impact speeds. Both models 1 and 4 are in excellent agreement with MD (symbols) for the highest impact speed (up = 2.0 km s^{-1}, blue symbols and curves). Differences among the MD and continuum predictions are noticeable for the intermediate case (u_p=1.0 kms^{-1}, red), with models 1 and 4 predicting, respectively, faster and slower pore collapse compared to MD. The MD and continuum predictions differ significantly for the 0.5 km s^{-1} impact (black). Model 1 predicts a collapse rate that is faster than for MD. Model 4 is stiff relative to MD and, as noted above, does not lead to complete pore closure. Although model 4 yields good agreement with MD for impact speeds of 1.0 and 2.0 km s^{-1}, it does not produce pore-closure results in agreement with MD for the 0.5 km s^{-1} impact case. Further improvements are required to make model 4 uniformly applicable over a range of shock pressures, particularly at the lower shock strengths where the models for the strength of the material play important roles in energy localization.

3.4.3 Discussion

The systematic examination of models and material properties for HMX presented above brings to light several insights and points to directions for future work to refine the currently available models:

1. For the two higher impact velocities (1.0 and 2.0 km s^{-1}) examined in this work, isotropic J2-plasticity models yield pore-collapse dynamics and initial post-collapse hotspots and blast waves in (inert) HMX that are in fairly good agreement with MD predictions. Note that the rate-dependent plasticity model is the same as used by Springer *et al.* [121], which is derived from experimental data of Dick *et al.* [136],[154],[155]. Pore-collapse times, profiles, and temperature and pressure

fields display the effects of shear and plastic deformation in agreement with MD. However, to obtain good agreement in this type of model, proper treatment of the melt curve is crucial: Energy localization occurs due to thermal softening and the resulting concentration of shear in the softened regions; eventually, melting in the shear bands relieves stress and therefore significantly affects the distributions of strain, strain rate, and deviatoric stress in the regions of the material outside of the shear bands. It is found that good agreement with MD is obtained with the (MD-derived) melt temperature model of Kroonblawd and Austin [63] but not with the Kraut–Kennedy model [153].

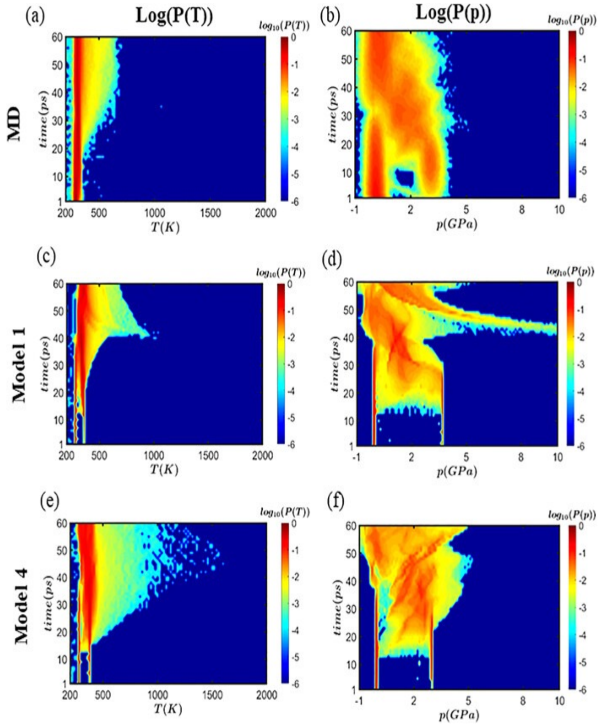

Figure 3.13: (a)–(f) For the 0.5 km s^{-1} impact, time-dependent probability distributions for temperature (left column) and pressure (right) during pore collapse, with probabilities shown on a logarithmic scale. The top, middle, and bottom rows correspond to MD, continuum model 1, and continuum model 4, respectively.

2. The strength model (i.e., the flow stress combined with the melt-temperature model) is found to be dominant in the overall pore-collapse behavior. Other aspects, such as pressure dependence of the shear modulus and (somewhat surprisingly) temperature dependence of the specific heat, have comparatively modest effects on the hotspot physics. A key finding of the study is that a rate-independent plasticity model fails to capture the primary features of pore collapse and the resulting hotspot distribution observed in MD calculations, whereas the rate-dependent model produces void collapse profiles, hotspot distributions, and shear bands that agree with MD results, at least for the higher velocity (shock strength) cases. The computational expense of the rate-dependent model is

nearly the same as the rate-independent (perfectly) plastic model. Therefore, we see no reason for continuum modelers to continue employing the rate-independent models for pore-collapse simulations of HMX.

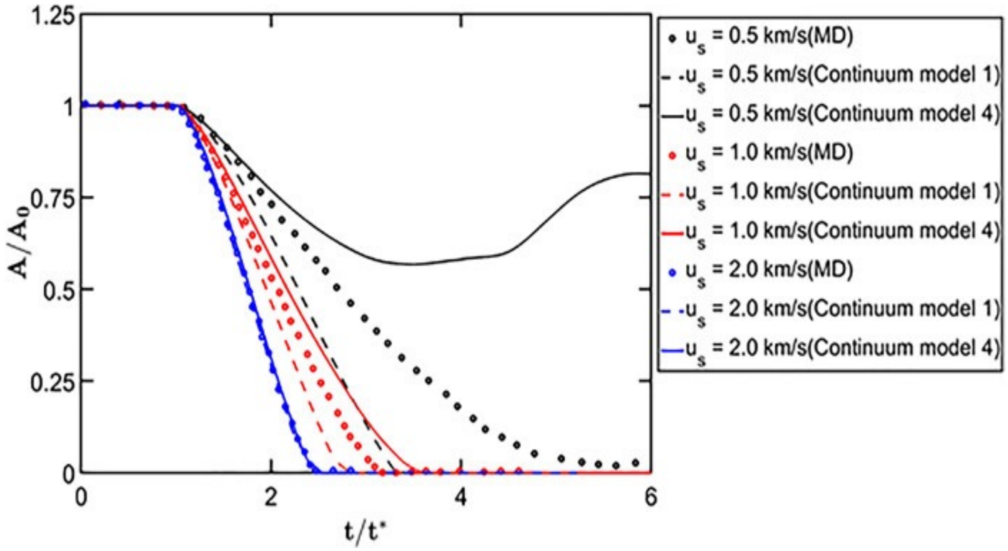

Figure 3.14: Scaled pore area vs scaled time t/t^* calculated using MD (symbols), continuum model 1 (dashed), and continuum model 4 (solid) for three impact speeds. Black: u_p=0.5 km s^{-1}; red: u_p=1.0 km s^{-1}; and blue: u_p=2.0 km s^{-1}

3. The next level of complexity in the treatment of HMX under shock is to incorporate the anisotropic response based on crystal plasticity. This will involve a significant increase in model sophistication and computational effort, as full incorporation of the physics of slip systems (ideally including temperature and pressure effects) and the evolution of the anisotropic elastic and plastic states of the material significantly increases the computational complexity. Such models have been used recently by Austin *et al.* [156],[157], Koslowski and co-workers [18], and Zhang and Oskay [188]. The need for such complexity, particularly under strong-shock conditions, remains to be fully explored. In the interim, the present isotropic J2-plasticity model (specifically, model 4) can be viewed as a compromise between physical fidelity and computational tractability, and the good agreement with MD for higher velocity impacts (1.0 km s^{-1}) encourages the use of the model to produce useful results on hotspot ignition and growth in HMX.

3.5 Conclusion

We have investigated the applicability of Eulerian isotropic J2-plasticity-based models for predicting deformation patterns and energy localization resulting from shock-induced collapse of a 50 nm pore in single-crystal β-HMX (β-octahydro-1,3,5,7-tetranitro-1,3,5,7- tetrazocine) using molecular dynamics (MD) predictions as the basis for assessment. Reverse-ballistic impacts at three impact speeds u_p=0.5, 1.0, and 2.0 km s^{-1} were used to drive the pore collapse, with nearly identical starting system geometries in the continuum and MD simulations. The interval of impact speeds studied was chosen so as to interrogate collapse mechanisms ranging from predominantly visco-plastic to predominantly hydrodynamic. A hierarchy of five isotropic continuum models was studied. By upgrading the models systematically with respect to the fidelity of the underlying physics, sensitivities with respect to the model forms and parameters were identified. Chemical reactivity was ignored, as the focus was on the purely thermo-mechanical response. The ability of the continuum models to produce results in agreement with the "ground truth" MD predictions was assessed both qualitatively and quantitatively by evaluating (1) profiles and modes of pore collapse, (2) temperature and pressure fields during and after pore collapse, (3) locations and strengths of the hot spots and blast waves produced, (4) time evolutions of probability distributions for temperature and pressure in the samples, and (5) evolutions of the pore area with time.

The baseline model (model 1), an elastic-perfectly plastic description, yields hydrodynamic collapse behavior for all three impact speeds, in qualitative disagreement with MD predictions except at the highest impact speed. To the extent that MD provides a reliable benchmark, the use of this kind of continuum description should be abandoned for the purpose of simulating pore collapse in HMX.

Incorporation of rate-dependent plasticity (model 2, which also includes strain hardening and thermal softening in the strength model) leads to extensive shear localization during collapse, in better agreement with MD albeit with significant differences still evident. Replacing the Kraut–Kennedy [153] melt curve, $T_m{=}T_m(p)$, with one reported recently by Kroonblawd and Austin [63] based on MD simulations (model 3), yields a marked difference in the collapse mechanism, particularly for the two weaker shock strengths studied, and much-improved agreement with MD. The Kroonblawd–Austin melt curve [63] exhibits a much steeper pressure dependence than the Kraut–Kennedy model; and this, combined with the rate-dependent strength description, leads to non-hydrodynamic collapse and reduced spatial density of shear banding but considerably higher heating in the shear bands formed.

Replacing the constant shear-modulus value with a pressure-dependent form determined from MD (model 4) has little effect on the pore collapse. Similarly, the use of a constant specific- heat value (model 5) in place of a quantum-like temperature-dependent specific-heat model has a modest effect on the pore-collapse results. The overall pore-collapse mechanisms and hot spot and blast-wave field properties predicted using model 4 yields results in best overall agreement with the MD predictions for all three impact speeds studied. However, the model 4 predictions for u_p=0.5 km s^{-1} are still in significant disagreement with the MD results. This is not surprising, because as the shock strength is decreased crystal anisotropy and other aspects of the crystal mechanics become increasingly important. Additional continuum model refinements, in particular, the incorporation of anisotropic crystal elasticity and plasticity, will be required to achieve high-fidelity agreement between the MD and continuum predictions.

Chapter 4

HEAD-TO-HEAD COMPARISON OF MOLECULAR AND CONTINUUM SIMULATIONS OF SHOCK-INDUCED COLLAPSE OF AN ELONGATED PORE IN AN ENERGETIC MOLECULAR CRYSTAL

4.1 Abstract

Shock-induced collapse of an elongated pore in the energetic crystal β-HMX (β-1,3,5,7-tetranitro-1,3,5,7-tetrazocane) is examined using all-atom molecular dynamics (MD) and continuum mechanics. The continuum simulation employs a recently proposed MD-guided material model for β-HMX. Collapse-induced shear band formation and hotspot-zone properties are calculated using both MD and continuum mechanics, for nearly identical simulation domains and identical impact conditions. The continuum model predicts shear band patterns and pore collapse behavior in good agreement with MD results; shear localization, plastic heating, and hydrodynamic impact-generated temperature rise lead to geometrically complicated hotspot zones in the vicinity of the collapse site. This work demonstrates that for the $\approx$10 GPa shock pressure studied isotropic rate-dependent Johnson-Cook-type elastoplastic models for HMX can provide physically consistent pore-collapse dynamics and hotspot features in comparison to MD, for nontrivial pore shapes. Such physically accurate models are required for reliable predictions of detonation sensitivity and performance for shocked energetic crystals. Opportunities for further model improvement are identified.

4.2 Introduction

The presence of pores and defects in energetic crystals markedly enhances the sensitivity of a heterogeneous energetic material to imposed shock loads [189]. Several mechanisms are responsible for the sensitivity which, in addition to dependence on the underlying molecular structures of the ingredients, stems from energy localization at defects and the formation of hotspots [190],[122]. Collapse of pre-existing pores in the crystal [34],[123],[191],[192],[193], formation of shear bands [90],[104],[194],[195], friction between sliding crystals and other interfaces [196],[197],[198], and plastic dissipation [199],[200],[201] are thought to be the most important mechanisms for hotspot formation. Among these, pore collapse and shear bands predominate at high shock intensities. Pore collapse has been studied by various researchers, providing characterization and quantification of the effects of shock intensity and pore shape for circular/spherical [93],[193],[126] elliptical [6],[202],[203], and arbitrary-shape pores [152],[203],[204]. Continuum models have typically employed isotropic constitutive descriptions, such as elastic-perfectly plastic [126],[203],[204], or rate-dependent Johnson-Cook (JC) J2 plasticity [84],[121],[167], that are calibrated empirically [154],[155] for limited intervals of loading conditions. Calculations with such semi-empirical, isotropic material models have yielded valuable insights and quantitative information on hotspot evolution, elucidating hydrodynamic (jetting) and, for JC-J2 treatments, shear-banding contributions to energy localization. Such calculations are relatively inexpensive from a computational standpoint and can be carried out to times sufficiently long for complete collapse of pores and the onset of sustained chemical reactions [131], including for fields of interacting pores [205] and real microstructures [206]. Energy localization due to shear banding has also been studied using sophisticated, anisotropic crystal plasticity models [156],[207],[208],[209]. However, such detailed models are computationally intensive and it can be challenging to carry calculations through to times long enough to capture reactive heat release from evolving hotspots. It is therefore advantageous to pursue the route of using simple, isotropic JC-J2 plasticity models to study and quantify the evolution of hotspots resulting from collapse, provided that the physical correctness and limits to their reliability can be established.

We recently [84] advanced a molecular dynamics (MD)-guided isotropic JC-J2 material model for the monoclinic energetic crystal β-HMX (β-1,3,5,7-tetranitro-1,3,5,7-tetrazoctane) which, in combination with other MD-derived material submodels (melting temperature [63] and shear modulus [21],[46]), yielded good agreement with MD predictions for pore-collapse dynamics, shear-band patterns, and hotspot-zone properties of initially circular (continuum) or right-cylindrical (MD) pores.

(Henceforth, we use 2D pore-shape descriptors for convenience where the meaning is unambiguous.) Shear-banding phenomena have been studied in the context of collapse of radially symmetric pores using both MD [18],[50],[63],[84],[93] and continuum models [18],[50],[63],[84],[121],[167]. The presence of shear bands during shock-induced collapse of elongated pores has also been observed in MD calculations [6]; however, the emanation of shear bands from, and their interaction with, elongated (crack-like) pores has not yet been examined using continuum models. Here, we apply the recently developed MD-guided JC-J2 model [84] to the case of an elongated pore and show that the model produces material deformation and energy localization in reasonable to good agreement with MD predictions. Mechanisms of collapse and energy localization are identified that are quite distinct from those for collapse of circular pores. Opportunities for further MD-guided continuum model improvements are identified.

4.3 Methods, Models, Analysis, and Computational Details

4.3.1 Methods and Models

An Eulerian multi-material sharp-interface computational approach [159] was used to simulate the continuum shock-induced collapse of a single ellipse-shape pore in an otherwise homogeneous β-HMX crystal. The governing equations and reaction mechanisms for simulating shock deformation of β-HMX have been presented by Rai *et al.* [126]. The MD-guided material model [84] employs a flow rule with yield strength σ_Y given by an isotropic rate-dependent JC model [130] calibrated to flyer-plate experiments due to Dick *et al.* [154]:

$$\sigma_Y = [A + B\varepsilon_p^n][1 + C(ln + \dot{\varepsilon}^*)]\left[1 - \left(\frac{T - T_{ref}}{T_m - T_{ref}}\right)\right]^M \tag{4.1}$$

Here, T is temperature, ε_p is equivalent plastic strain; $\dot{\varepsilon}^*$ is the dimensionless plastic strain rate, obtained by scaling the strain rate $\dot{\varepsilon}$ by the characteristic plastic strain rate $\dot{\varepsilon}_0$=10^{-3} μs^{-1}; and T_{ref}=300 K is the reference temperature. The coefficients A, B, n, C, and M have values of 100 MPa, 100 MPa, 1.086, 0.1, and 3, respectively. The pressure-dependent melting point T_m=$T_m(p)$ comes from MD [63]. The form is

$$T_m = T_{m0}\left(1 + \frac{P - P_{ref}}{a'}\right)^{1/c'} \tag{4.2}$$

where P is pressure, T_{m0}=551 K is the reference melting temperature, P_{ref}=0 GPa is the reference pressure, and and are fitting parameters with values 0.305 GPa and 3.27, respectively. This material model is referred to as “Model 4” in Das *et al.* [84] and yielded the closest agreement to MD simulations for pore collapse among a systematic hierarchy of five continuum models considered by those authors.

The MD simulations were performed using the LAMMPS code [115]. Details of the MD methodology are presented in Das *et al.* [84] so are only briefly described here. We used the all-atom, fully flexible, nonreactive force field originally developed by Smith and Bharadwaj [44], with modest changes due to others [45],[48],[50]. The force field describes covalent bond stretching, angle bending, and improper dihedral distortions as harmonic oscillators. Dihedral terms are described using a truncated cosine series. Non-bonded pair interactions of Buckingham-plus-Coulomb form are included between atoms belonging to different molecules and between atoms separated by three or more covalent bonds within a molecule. A very short-range non-bonded pair repulsion was added as described in previous work [50] to accommodate the short non-covalent interatomic distances sampled in the extreme environment of the collapse zone. LAMMPS input decks capturing the force field implementation and a topology description for one unit cell of β-HMX are available in the supporting information for previous work [21].

4.3.2 Computational Setup and Boundary Conditions

The MD and continuum simulations were performed using a (nearly) identical setup; see Figure 4.1. We consider a block of β-HMX that contains an initially ellipse-shape pore and is subjected to normal-incidence shock loading in a reverse-ballistic configuration wherein the *sample* impacts with velocity $\mathbf{u}_p$ onto a rigid and stationary *piston*. This results in a supported shock wave that initially travels with velocity $\mathbf{u}_w$ in the frame of the stationary piston, anti-parallel to $\mathbf{u}_p$. The shock velocity $\mathbf{u}_s$ in the commonly used moving-piston reference frame is $\mathbf{u}_s$=$\mathbf{u}_w$+$\mathbf{u}_p$. The 3D Cartesian impact velocity vector is $\mathbf{u}_p$=(0, 1.0 km s^{-1}, 0), thus the lead shock propagates through the sample bottom-to-top along $+\hat{\boldsymbol{y}}$. For MD, the monoclinic unit cell for β-HMX (P2$_1$/n space group setting) [210] was replicated in 3D space by factors of 8$\boldsymbol{a}$ x 146$\boldsymbol{b}$ x 198$\boldsymbol{c}$, and $\boldsymbol{a}$, $\boldsymbol{b}$, $\boldsymbol{c}$ are the lattice vectors, yielding a quasi-2D supercell that is approximately 5.3 nm × 301.0 nm × 303.9 nm.

The mapping of the crystal frame to the Cartesian lab frame is $\boldsymbol{a}||\hat{\boldsymbol{x}}$, $\boldsymbol{b}||\hat{\boldsymbol{y}}$ and $\boldsymbol{c}$ in the $+\hat{\boldsymbol{z}}$ half space. The cylinder axis of the pore is parallel to $\boldsymbol{a}$ and the pore extends all the way through the supercell. The system contains 1.8036×10^6 HMX molecules after the pore is created. Molecules belonging to the first three unit-cells at the bottom of the system are assigned to the rigid piston,

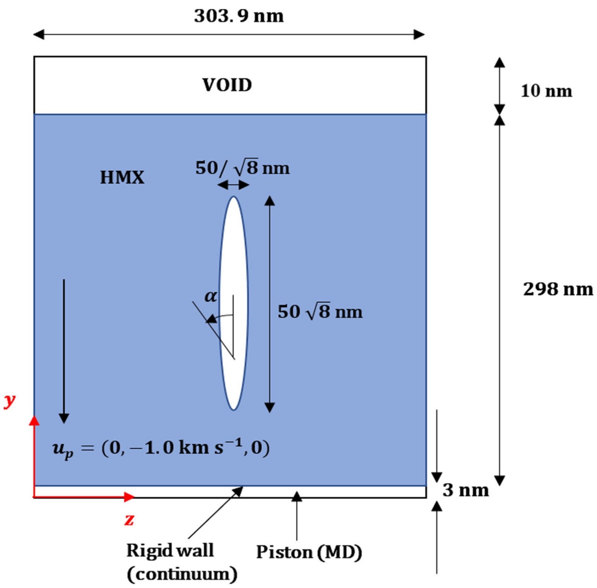

Figure 4.1: Simulation Setup

which is 3.0 nm thick. In crystallographic terms, impact occurs on the (010) surface and the shock direction is [010].

The ellipse-shape pore is aligned with the vertical axis and has a circle-equivalent diameter of 50.0 nm and aspect ratio AR=8.0. The semimajor and semiminor axis lengths are $25\sqrt{8}$ nm and $25/\sqrt{8}$ nm, respectively. The pore is a vacuum and an additional 10.0 nm vacuum region is introduced at the top of the simulation cell to minimize electrostatic interactions across the periodic boundaries in the MD setup.

The MD simulation was performed using 3D periodic boundary conditions and the continuum simulation using reflective boundary conditions on the lateral domain boundaries. The MD shock was simulated in the isochoric-isoenergetic (NVE) ensemble using a 0.1 fs time step and was continued until the sample length, measured along the shock direction [010], increased to 105% of the value at maximum compression, which corresponds to the arrival of the curved lead shock at the free surface. Atomic positions, velocities, and stress-tensor components were recorded at 0.5 ps intervals for subsequent analyses, details for which are described in Das *et al.* [84] and references therein.

The continuum simulation was 2D and employed the plane-strain assumption. The domain is defined in the y–z Cartesian plane, on a rectangular grid that extends from y=3.0 nm to 311.0 nm and z=0 to 303.9 nm. A rigid stationary wall located at y=3.0 nm is used to emulate the piston-sample interface in the MD setup and the region from y=301.0 nm to 311.0 nm is initially vacuum as in the MD case.

A detailed study of the resolution requirements required for grid-independent results for pore collapse was reported by Rai *et al.* [211] and has guided the choice for the grid density used here. A mesh-dependence study for the specific material model used here is provided in the Supporting Information of Das *et al.* [84] and the mesh employed here is the same as in that paper; a baseline grid spacing of 0.175 nm, or ≈40 points across the semiminor axis length of the initial pore. However, with adaptive local mesh refinement (LMR) and three levels of refinement [177], the finest mesh spacing is $0.175/2^3$ nm or 0.021875 nm; that is, approximately 40×2^3=320 grid cells across the initial semi-minor axis length, which is sufficiently refined for numerical convergence in the present simulation.

4.4 Results and Discussion

Figures 4.2(a) and 4.2(b) are, respectively, observations of the MD and continuum simulations 63.0 ps after initiation of the shock. The MD and continuum results depict instantaneous HMX molecular center-of-mass positions and a Schlieren rendering of the mass-density gradient, respectively. Animations of those same quantities are provided in the Supporting Information. The general features of the MD and continuum fields agree. Overall collapse occurs not by nominally radially inward flow toward a common point as is typically the case for circular pores, but by a "pinching shut" mechanism in which flow at the pore surface occurs mainly perpendicular to the pore semi-major axis, with closure occurring sequentially from bottom to top. The continuum model is more resistant to inelastic deformation compared to MD [84], as can be seen by comparing the MD and continuum pore-wall shapes at equivalent times. Convective flow in the cavity region during collapse is more complex in the continuum simulation than for MD; hydrodynamic instabilities are apparent in the pore cavity and adjacent melted regions. The locations at which the collapse-induced shock wave emanating from the pore-closure site interacts with the wave reflected from the free surface are marked by dashed red circles in Figs. 4.2(a) and 4.2(b). This good late-time agreement suggests that the overall shock dynamics is well represented by the continuum model. Figs. 4.2(c) and 4.2(d) present contours of von Mises stress at t=50.0 ps, ≈7 ps after complete pore collapse. Although the magnitude of the von Mises stress in shocked material far from the pore is noticeably higher for MD, the regions of stress relief due to melted zones (in blue) reveal good correspondence between the MD and continuum predictions.

The shear band formation predicted by MD and continuum share similar predominant features. For the MD calculation, three prominent pairs of shear bands, which are largely symmetric about the pore center line, nucleate at locations near the bottom end of the pore. The shear bands denoted

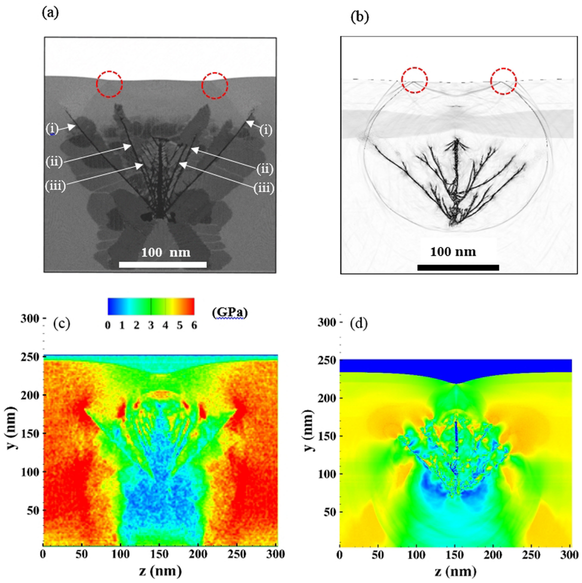

Figure 4.2: Top row: System observations at t=63.0 ps; (a) molecular center-of-mass positions from MD and (b) Schlieren contours of the continuum mass density. Bottom row: local von Mises stresses at t=50.0 ps, for (c) MD and (d) continuum. The color bar located above panel (c) applies to panels (c) and (d).

"(i)" in Fig. 4.2(a) begin as dislocations within ≈4.5 ps of the shock arrival at the pore, growing diagonally toward the free surface at angles $\alpha \approx 45^\circ$ with respect to the lead shock direction and exhibiting local disordering within ≈1 ps of initial dislocation motion past any location along the slip plane. The shear bands labeled "(ii)" and "(iii)" nucleate ≈7.5 ps after shock arrival and propagate toward the free surface at $\alpha \approx 23$, via a kink-mediated mechanism. By the end of the simulation, MD predicts a spatially connected network of shear localization within a region bounded by the second prominent shear bands on either side of the pore center line.

In the continuum simulation [Fig. 4.2(b)], a pair of shear bands nucleates from the bottom tip of the pore within 2.0 ps of lead shock passage. Both nascent bands exhibit complicated branching at very short times, out of which the dominant pair quickly emerges. Subsequent branching (and re-branching) occurs as the growth tips propagate into the material. Later, a second burst of shear bands forms further along the pore, with growth features similar to those for the first group. Close inspection of the continuum pore surface reveals closely spaced shear bands with α approximately ±45° and ±135° that nucleate along the pore surface. The behavior during approximately the first 20% of shock traversal across the pore is particularly interesting: the ±135° shear bands either disappear or are overwhelmed by the second burst of ±45° bands. The final MD and continuum shear-band patterns are qualitatively similar but different in detail. Whereas the nucleation and initial growth of shear bands in MD is mediated by the crystal structure, leading to comparatively straight shear bands, in the continuum case the shear bands are more curved and branched. The perturbations leading to these incipient shear bands are of short wavelength and are certainly influenced by the mesh resolution. However, the shear bands that survive and grow into the larger bands coarsen to achieve spacing similar to those seen in MD; this competition and coarsening of shear bands is aligned with theoretical understanding of instabilities and spacing selection [186],[212],[213],[214].

Figure 4.3 contains snapshots of temperature fields at three instants during and after collapse. The hot spot pattern is significantly different from those seen [202],[203] in calculations for ellipse-shape pores using a rate-independent elastic-perfectly plastic description of HMX which does not admit shear-band formation and leads to effectively hydrodynamic pore collapse, such that the hot spot takes on the shape of the elongated pore albeit with vertical structures superposed along the entire length; cf. Fig. 8 of Rai *et al.* [202]. It is evident to the eye in Fig. 4.3 that MD predicts lower temperatures behind the lead shock in regions far from the hot spot zone, less intense and less localized heating in the cores of the shear bands, and more localized heating in regions of convective flow in the vicinity of the collapsing pore.

In Fig. 4.4 we compare distributions of sample area vs. temperature for MD (black) and continuum mechanics (red), specifically, the area A of the sample occupied by material at temperature T, scaled by the initial area of the HMX sample, A_0 (=298.0 nm × 303.9 nm), plotted on a semi-logarithmic scale. The analysis is for t=50.0 ps, which is approximately 7 ps after pore closure in both simulations. Although the shapes of the curves are similar, the continuum result is shifted toward higher temperatures. This is generally consistent with the results observed in Fig. 4.3.

The differences between the MD and continuum predictions are explained at least in part by the different treatments of specific heat in the two models: It is classical in the MD (i.e., constant) whereas the continuum model employs a temperature-dependent form [20] that is commonly used in continuum modelling of HMX. The temperature-dependent specific heat only approaches the classical value when the temperature reaches a few thousand kelvins. The effect of specific heat on energy localization is complicated, as the temperature appears in the thermal softening term of the strength model [Eq. (1)], which clearly will affect shear-band formation and evolution. Another source of the observed discrepancy is the use of an isotropic continuum elasto-plasticity model for the β-HMX, which does not reflect the underlying anisotropic crystal structure that is inherently present in the MD [50],[84]. Anisotropy and crystal slip systems confer strong directionality to the MD shear bands, whereas the isotropic continuum model allows for branched shear bands that respond to numerical noise, yielding stochastic side-branching similar to other isotropic diffusion-driven instabilities in pattern-forming systems [215],[216],[217]. The effects of crystal anisotropy will be even more apparent for weaker impacts [50],[84]. Further analysis and re-calibration of the model are needed to better align the MD and continuum temperatures and, presumably, the von Mises stress fields.

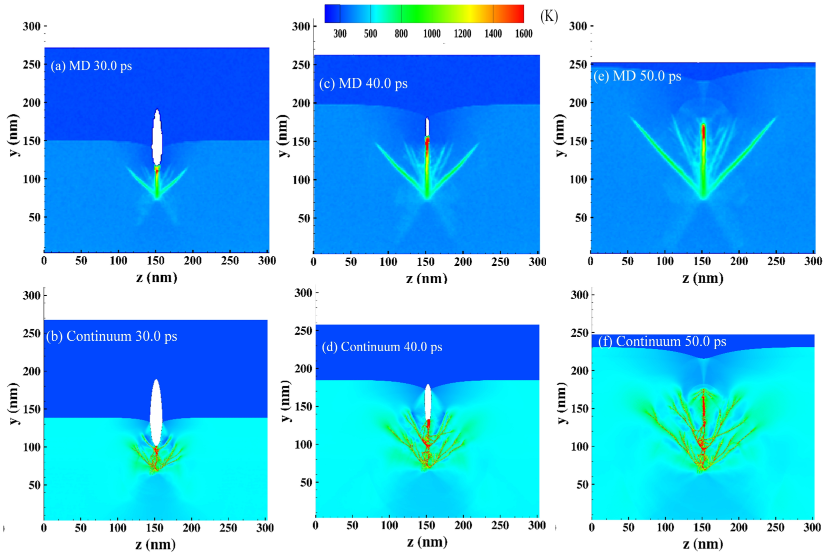

Figure 4.3: Snapshots of temperature fields during pore collapse, at t=30.0, 40.0, and 50.0 ps, for MD [panels (a), (c), and (e)] and continuum mechanics [(b), (d), and (f)].

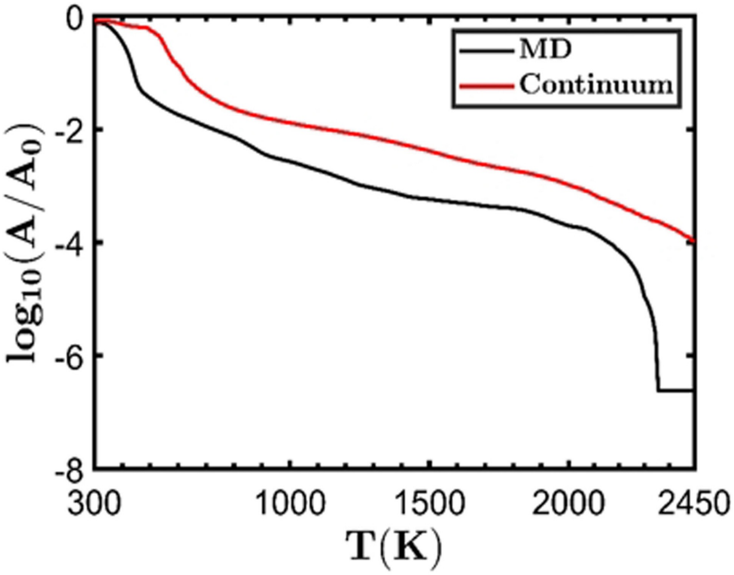

Figure 4.4: Distributions of scaled sample area vs. temperature, at the instant t=50.0 ps.

4.5 Conclusion

Head-to-head MD and continuum simulations of shock-induced collapse of an elongated (crack-like) pore in single-crystal β-HMX were performed, to examine the ability of a recently published continuum material description ("Model 4" from Das *et al.* [84]) to produce physically correct energy localization and deformation response. The continuum model employs an isotropic Johnson-Cook J2 strain-, strain rate-, and temperature-dependent strength model, with MD-informed sub-model parameterization. We find shear-band patterns and pore-collapse behavior in good overall agreement with MD. In contrast to previous continuum calculations of collapse of elongated pores, all of which employed rate-independent descriptions, we find a rich structure of shear bands and associated heated zones, and a "pinching shut" pore-closure mechanism that differs significantly from hydrodynamic-like collapse. This has important implications for the hotspots resulting from the closure of the quite commonly encountered crack-like pores and other extended defects in heterogeneous energetic materials. Although the continuum model predicts shear-band patterns in overall good agreement with MD, details of the shear bands and temperature fields indicate greater intensity of shear in the continuum calculations. Furthermore, the continuum model yields systematically higher temperatures of 'bulk' shock-compressed material, which leads to enhanced thermal softening in the continuum calculations. Thus, although the model produces collapse and localization behaviors that are qualitatively consistent with MD, further development is needed to improve the agreement. This issue will be more prominent for shock intensities lower than the one studied here.

Chapter 5

CONCLUSION AND FUTURE WORK

This thesis focuses on molecular dynamics (MD) simulations of the thermal and mechanical shock response of the energetic organic crystal (β-1,3,5,7-Tetranitro-1,3,5,7-tetraocane) (β-HMX) as predicted using a non-reactive, fully flexible force field. The main focus was to understand the behavior of the material when a shock wave passes through a single pore-type defect in the system. Results from these MD simulations played important roles in determining the physics sub-models used in the continuum scale description and in providing atomic-scale validation for the continuum scale predictions.

Chapter 2 focused on addressing a few important practical aspects that arise when designing an MD simulation. Factors of consideration are; sample thickness, crystal orientation, and robustness of the conclusions that can be drawn from individual large-scale MD simulations. This study was carried out using three different models where models 1 and 2 differed only on the sample thickness and model 2 and 3 were different based only on the crystal orientation in the transverse directions. Further, three different independent realizations were carried out with model 1 to test the robustness of the predictions. All these models were tested at two different impact speeds. Models 1 and 2 revealed that the overall results from the simulations were insensitive to the sample thickness at both impact speeds, while for models 2 and 3, slight differences were observed when comparing the shock profile temperatures, and shock speeds. These differences were significant when the shock strength was low. The independent realizations performed using Model 1 revealed that the three trials were almost identical in temperature and pressure distributions with slight variations in the shear banding across the material, giving confidence that a single simulation is representative of a particular scenario.

Chapter 3 was focused on using MD simulations as the “ground truth” to build a Eulerian isotropic J2-plasticity-based model to predict deformation occurring in pore-collapse shock simulations. Three shock strengths were tested for each among five continuum models. These models were built by updating in a hierachical fasion to better capture the underlying physics. Qualitative and quantitative analysis was done by evaluating (1) pore-collapse profiles, (2) temperature and pressure fields, (3) hot-spot analysis, (4) probability distributions of temperature and pressure, and (5) evolution of pore area. Model 1, which was an elastic-perfectly plastic description, produced results that qualitatively disagreed with the MD prediction for low strength of shock. Model 2, which included rate-dependent plasticity, leads to extensive formation of sheer bands during the collapse. This model was in better agreement with MD when compared to model 1, although significant differences were still evident. In Model 3, the change in melt curve model improved the agreement with MD. Specially for the collapse mechanism and especially for weaker shocks. Replacing the shear modulus with an improved P-dependent model from MD Model 4 had only a slight effect on the overall result. Changing the specific heat value in model 5 demonstrated only a moderate effect for the pore collapse mechanism. Considering the overall behavior of the models, model 4 was chosen to "best" represent MD simulations. However, even this model was significantly in disagreement with MD at the lowest impact speed. Reason for this behaviour is due to dominant effects on the crystal anisotropy and other crystal properties at the low impact speed.

Chapter 4 is a study that builds on Chapter 3. In this study model 4 ("best model") that was discussed above is tested with an elongated pore instead of the circular pore present in chapter 3. This study revealed a pore-collapse mechanism, which we call a "pinching shut" mechanism, that is different to the hydrodynamic pore collapse mechanisms we observe in the circular pore systems. Comparison on the MD simulations with continuum simulations showed that the latter predicts the overall sheer banding in fairly good agreement with MD. However, the details of the continuum shear bands and temperature fields suggest the need for addition of physics in the description.

Understanding shock-induced pore-collapse mechanisms to produce better informed continuum scale models are important to bridge the gap from nano-scale to macro-scale. Chapters in this thesis were focused on designing accurate MD simulations that best represent the pore-collapse mechanism due to a shock wave when passing through a single pore-type defect in the material. These large-scale MD simulations can be used to inform continuum scale simulations on atomic level properties and to build a meso-scale continuum description that captures the pore collapse mechanisms accurately. During the studies it was evident that there are few aspects like differences in bulk temperature, need for incorporation of plasticity and elasticity into the continuum models needs attention to produce high-fidelity agreements between MD and continuum predictions. Future of this study will involve further improvement of the continuum scale description by minimizing the differences we observe when comparison to MD simulations. Achieving this goal will provide the opportunity to bridge data from micro scale to the macro scale with high level of confidence.

Appendix A

APPENDICES

A.0.1 DATA file for β-HMX at 298 K and 1 atm pressure

```
28 atoms
28 bonds
48 angles
40 dihedrals
8 impropers
5 atom types
4 bond types
7 angle types
3 dihedral types
2 improper types
0.000000 6.580590 xlo xhi
0.000000 10.452470 ylo yhi
0.000000 7.596642 zlo zhi
0.000000 -1.159355. 0.000000 xy xz yz
Masses
1 1.0080
2 14.0070
3 14.0070
4 15.9990
5 12.0110
Atoms
```

Atomid	molid	typ	charge	x	y	z
1	1	3	0.056375	-1.17288549	0.25504027	1.55807133
2	1	5	-0.540000	-1.31400150	1.19680782	0.40869935
3	1	3	0.056375	-0.07516914	1.28147282	-0.28791274
4	1	5	-0.540000	0.10696048	0.68777253	-1.65378902
5	1	3	0.056375	1.17288549	-0.25504027	-1.55807133
6	1	5	-0.540000	1.31400150	-1.19680782	-0.40869935
7	1	3	0.056375	0.07516914	-1.28147282	0.28791274
8	1	5	-0.540000	-0.10696048	-0.68777253	1.65378902
9	1	2	0.860625	-2.32056445	0.01463346	2.22657585
10	1	4	-0.458500	-3.32312495	0.62923869	1.81483784
11	1	4	-0.458500	-2.26840735	-0.74839685	3.20426371
12	1	2	0.860625	0.88344681	2.11767042	0.23929423
13	1	4	-0.458500	0.71237343	2.57966960	1.39474352
14	1	4	-0.458500	1.85096127	2.29745291	-0.47327081
15	1	2	0.860625	2.32056445	-0.01463346	-2.22657585
16	1	4	-0.458500	3.32312495	-0.62923869	-1.81483784
17	1	4	-0.458500	2.26840735	0.74839685	-3.20426371
18	1	2	0.860625	-0.88344681	-2.11767042	-0.23929423
19	1	4	-0.458500	-0.71237343	-2.57966960	-1.39474352
20	1	4	-0.458500	-1.85096127	-2.29745291	0.47327081
21	1	1	0.270000	-1.49475684	1.97551683	0.78245415
22	1	1	0.270000	-1.97618565	0.94072230	-0.28867241
24	1	1	0.270000	0.36134313	1.28565381	-2.32457254
25	1	1	0.270000	1.49475684	-1.97551683	-0.78245415
26	1	1	0.270000	1.97618565	-0.94072230	0.28867241
27	1	1	0.270000	0.74951901	-0.24040681	1.94474042
28	1	1	0.270000	-0.36134313	-1.28565381	2.32457254

Bonds

id	typ	atom1	atom2
1	1	9	10
2	1	9	11
3	1	12	13

```
4 1 12 14

5 1 15 16

6 1 15 17

7 1 18 19

8 1 18 20

9 2 1 9

10 2 3 12

11 2 5 15

12 2 7 18

13 3 1 2

14 3 3 2

15 3 3 4

16 3 5 4

17 3 5 6

18 3 7 6

19 3 7 8

20 3 1 8

21 4 2 21

22 4 2 22

23 4 4 23

24 4 4 24

25 4 6 25

26 4 6 26

27 4 8 27

28 4 8 28

Angles

id typ atom1 atom2 atom3

1 1 10 9 11

2 1 13 12 14

3 1 16 15 17

4 1 19 18 20

5 2 10 9 1

6 2 11 9 1
```

7 2 13 12 3

8 2 14 12 3

9 2 16 15 5

10 2 17 15 5

11 2 19 18 7

12 2 20 18 7

13 3 9 1 2

14 3 9 1 8

15 3 12 3 2

16 3 12 3 4

17 3 15 5 4

18 3 15 5 6

19 3 18 7 6

20 3 18 7 8

21 4 2 3 4

22 4 4 5 6

23 4 6 7 8

24 4 8 1 2

25 5 1 2 21

26 5 1 2 22

27 5 1 8 27

28 5 1 8 28

29 5 3 2 21

30 5 3 2 22

31 5 3 4 23

32 5 3 4 24

33 5 5 4 23

34 5 5 4 24

35 5 5 6 25

36 5 5 6 26

37 5 7 6 25

38 5 7 6 26

39 5 7 8 27

40 5 7 8 28

41 6 21 2 22

42 6 23 4 24

43 6 25 6 26

44 6 27 8 28

45 7 1 2 3

46 7 3 4 5

47 7 5 6 7

48 7 7 8 1

Dihedrals

id typ atom1 atom2 atom3 atom4

1 1 10 9 1 2

2 1 10 9 1 8

3 1 11 9 1 2

4 1 11 9 1 8

5 1 13 12 3 4

6 1 13 12 3 2

7 1 14 12 3 4

8 1 14 12 3 2

9 1 16 15 5 4

10 1 16 15 5 6

11 1 17 15 5 4

12 1 17 15 5 6

13 1 19 18 7 8

14 1 19 18 7 6

15 1 20 18 7 8

16 1 20 18 7 6

17 2 21 2 1 8

18 2 21 2 3 4

19 2 22 2 1 8

20 2 22 2 3 4

21 2 23 4 3 2

22 2 23 4 5 6

23 2 24 4 3 2

24 2 24 4 5 6

25 2 25 6 5 4

26 2 25 6 7 8

27 2 26 6 5 4

28 2 26 6 7 8

29 2 27 8 7 6

30 2 27 8 1 2

31 2 28 8 7 6

33 3 2 1 8 7

34 3 2 3 4 5

35 3 4 3 2 1

36 3 4 5 6 7

37 3 6 5 4 3

38 3 6 7 8 1

39 3 8 7 6 5

40 3 8 1 2 3

Impropers

id typ atom1 atom2 atom3 atom4

1 1 1 8 2 9

2 1 3 2 4 12

3 1 5 4 6 15

4 1 7 6 8 18

5 2 9 10 11 1

6 2 12 13 14 3

7 2 15 16 17 5

8 2 18 19 20 7

A.0.2 Supporting information for Molecular Dynamics-guided Material Model for the Simulation of Shock-induced Pore Collapse in β-1,3,5,7-tetranitro-1,3,5,7-tetrazocane (β-HMX)

Justification for use of a pressure-dependent but not temperature-dependent shear modulus in models 4 and 5

In continuum Models 4 and 5, the constant value of the shear modulus G used in Models 1-3 is replaced by a pressure-dependent form. Ideally, temperature dependence would also be included but at the time that the study was performed we only had values for G=G(P) on the room-temperature isotherm. Since then, G-values on additional isotherms have become available. We have captured the relevant results from Ref. [21] in the table just below.

P (GPa)	T = 300 K	500 K	700 K	900 K	1100 K
0	7.4	6.2	4.7	melts	melts
5	16.9	15.6	14.7	13.5	12.6
10	23.6	22.5	21.2	19.6	17.6
20	34.1	33.0	31.9	30.6	29.1
30	42.3	41.2	40.0	38.7	37.3

Table A.1: $P-$ and $T-$dependent shear moduli from Ref [21], in GPa Values shown are Voigt-Reuss-Hill averages.

From the table, one can see that except at the lowest pressure for which melting occurs at the highest temperatures, accompanied by the expected decrease of G toward zero relative G values increase much more with increasing pressure than they decrease with increasing temperature on the intervals studied. For example: the four boldface entries in the table show that the quotient G(30 PGa)/G(5 GPa) is 2.5 at 300 K and 3.0 at 1100 K; whereas G(300 K)/G(1100 K) is 1.3 at 5 GPa and 1.1 at 30 GPa. That is, G stiffens by approximately 250% -300% between 0 and 30 GPa, but softens by only approximately 12%-25% between 300 K and 1100 K.

Therefore, although temperature dependence should be included for the sake of completeness, the fact that it was not included should not significantly affect our results or conclusions. This is further supported by results in the main article where it is shown that use of the pressure-dependent G in Model 4 only marginally alters the pressure and temperature distributions compared to predictions for Model 3, which uses a constant G; cf. Figs. 3.4-3.6 in the main article. Because G is weakly dependent on temperature compared to pressure, and the pressure dependence was shown to have minimal effect on the predictions, we would not expect incorporation of the temperature dependence to have a significant effect.

A study of mesh-size sensitivity, using model 4 as an example

The incipience of the shear bands at a free surface is an instability phenomenon. As such, it is certainly mesh dependent. However, the final shear-band pattern exhibited can be shown to converge for sufficiently fine meshes. A study of mesh-size sensitivity on the features of the shock-induced pore collapse reported in the main article was performed, for the case of a 1.0 km s^{-1} impact, using Model 4 as a specific case. The results are shown in Figs. A.1 and A.2 below.

Five different mesh resolutions were used, corresponding to 50, 100, 200, 400, and 800 mesh points across the 50 nm initial pore diameter. (Note: The simulations reported in the main article used 400 points across the diameter.) Temperature contours obtained using these mesh sizes, 35 ps after the impact between the HMX sample and the rigid wall at the bottom, are compared in Fig. A2S1. The progression from panels (a) to (e) corresponds to increasing mesh resolution. Qualitative comparisons among the results reveal that the mesh resolutions corresponding to 50 and 100 grid points across the pore diameter [panels (a) and (b)] fail to predict the shape of the shear bands seen in the higher resolution calculations. The overall distribution of the shear bands starts to emerge at a mesh resolution of 200 points [panel (c)], but clearly is not converged. By contrast, panels (e) and (f), corresponding to 400 and 800 points, respectively, reveal little difference in results for those two resolutions. For a quantitative comparison, Fig. A.2 contains normalized distributions of temperature in the samples for the different mesh resolutions, at the same instant studied in Fig. A.1. Figure A.2 shows that all five mesh resolutions yield similar distributions of temperature up to ≈600 K, which is close to the bulk temperature in the shocked samples. By contrast, for $T > 600$ K the temperature distributions for mesh resolutions of 50, 100, and 200 points differ significantly from those obtained using 400 and 800 points. However, the results for 400 and 800 points are quite similar for temperatures extending to ≈2000 K. Although the fine-scale details of the shear bands formed will surely be grid-dependent and sensitive to noise, the results in Figs. A.1 and A.2 suggest that the grid resolution used in the main article is sufficient to achieve practically meaningful predictions.

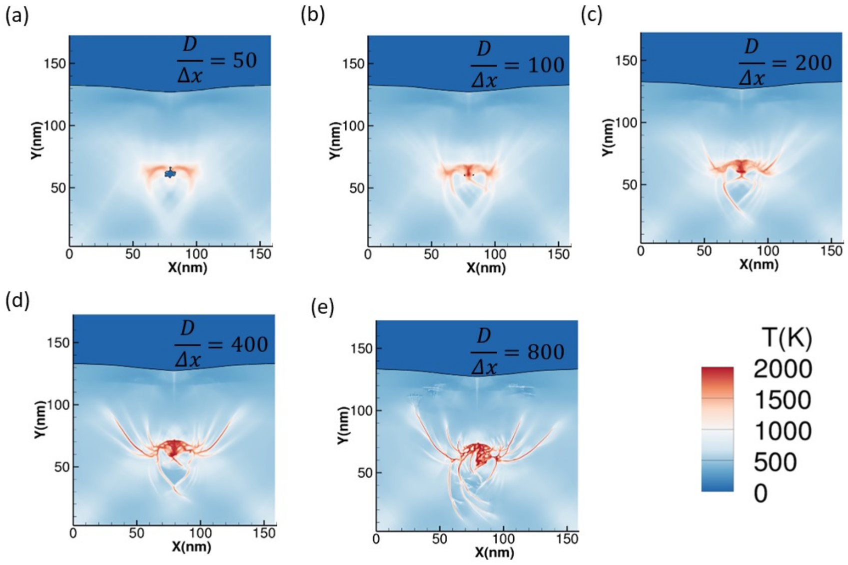

Figure A.1: For the 1.0 kms^{-1} impact, contours of temperature at $t = 35$ ps computed for Model 4, using five different grid resolutions, $\frac{D}{\Delta x}$ (a) 50 grid points across the initial pore diameter; (b) 100 points; (c) 200 points: (d) 400 points: and (e) 800 points.

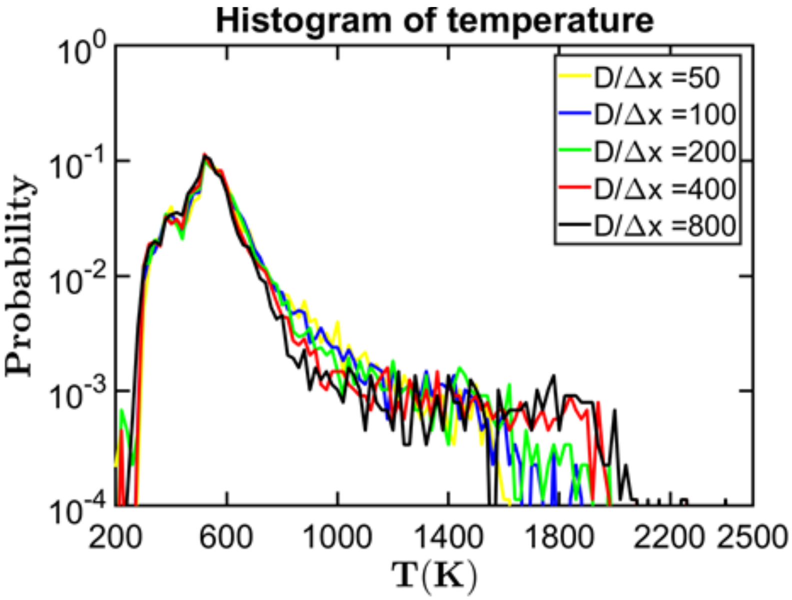

Figure A.2: As in Fig. A.1, but showing normalized distribution functions for temperature.

BIBLIOGRAPHY

[1] J. P. Agrawal, *High energy materials: propellants, explosives and pyrotechnics* (John Wiley & Sons, 2010).

[2] F. Jiao, Y. Xiong, H. Li, and C. Zhang, “Alleviating the energy & safety contradiction to construct new low sensitivity and highly energetic materials through crystal engineering”, CrystEngComm **20**, 1757–1768 (2018).

[3] L. E. Fried, “The reactivity of energetic materials at extreme conditions”, Reviews in computational chemistry, 159–190 (2007).

[4] Q.-L. Yan and S. Zeman, “Theoretical evaluation of sensitivity and thermal stability for high explosives based on quantum chemistry methods: a brief review”, International Journal of Quantum Chemistry **113**, 1049–1061 (2013).

[5] Y. Horie, “Hot spots, high explosives ignition, and material microstructure”, in Materials science forum, Vol. 767 (Citeseer, 2014), pp. 3–12.

[6] C. Li, B. W. Hamilton, and A. Strachan, “Hotspot formation due to shock-induced pore collapse in 1, 3, 5, 7-tetranitro-1, 3, 5, 7-tetrazoctane (hmx): role of pore shape and shock strength in collapse mechanism and temperature”, Journal of Applied Physics **127**, 175902 (2020).

[7] C. D. Molek, E. J. Welle, J. O. Mares Jr, J. Vitarelli, D. Barrett Hardin, and M. Stuthers, “Impact of void structure on initiation sensitivity”, Propellants, Explosives, Pyrotechnics **45**, 236–242 (2020).

[8] C. A. Duarte, A. Hamed, J. D. Drake, C. J. Sorensen, S. F. Son, W. W. Chen, and M. Koslowski, “Void collapse in shocked-hmx single crystals: simulations and experiments”, Propellants, Explosives, Pyrotechnics **45**, 243–253 (2020).

[9] S. Roy, Y. T. Nguyen, C. Neal, S. Baek, and H. Udaykumar, “Meso-scale simulation of energetic materials. i. a method for generating synthetic microstructures using deep feature representations”, Journal of Applied Physics **131**, 055904 (2022).

[10] M. Baer, "Modeling heterogeneous energetic materials at the mesoscale", Thermochimica acta **384**, 351–367 (2002).

[11] L. Verstraete, *Accidental discoveries: from laughing gas to dynamite* (FriesenPress, 2016).

[12] S. Meyers and E. S. Shanley, "Industrial explosives-a brief history of their development and use", Journal of Hazardous Materials **23**, 183–201 (1990).

[13] R. V. Tsyshevsky, O. Sharia, and M. M. Kuklja, "Molecular theory of detonation initiation: insight from first principles modeling of the decomposition mechanisms of organic nitro energetic materials", Molecules **21**, 236 (2016).

[14] J. Zhang, T. L. Jackson, J. D. Buckmaster, and J. B. Freund, "Numerical modeling of shock-to-detonation transition in energetic materials", Combustion and Flame **159**, 1769–1778 (2012).

[15] D. Badgujar, M. Talawar, S. Asthana, and P. Mahulikar, "Advances in science and technology of modern energetic materials: an overview", Journal of Hazardous Materials **151**, 289–305 (2008).

[16] T. Varghese, *The chemistry and technology of solid rocket propellants (a treatise on solid propellants)*, Vol. 1 (Allied Publishers, 2017).

[17] L. Vargas, J. Caltagirone, and S. R. I. S. A. TX, "Evaluation of pyrotechnic fire suppression system for six pyrotechnic compositions", US Army Armament Research and Development Center, Dover, NJ (1985).

[18] C. A. Duarte, C. Li, B. W. Hamilton, A. Strachan, and M. Koslowski, "Continuum and molecular dynamics simulations of pore collapse in shocked β-tetramethylene tetranitramine (β-hmx) single crystals", Journal of Applied Physics **129**, 015904 (2021).

[19] H. G. Gallagher, J. N. Sherwood, and R. M. Vrcelj, "Growth and dislocation studies of β-hmx", Chemistry Central Journal **8**, 1–11 (2014).

[20] R. Menikoff and T. D. Sewell, "Constituent properties of hmx needed for mesoscale simulations", Combustion theory and modelling **6**, 103 (2002).

[21] A. Pereverzev and T. Sewell, "Elastic coefficients of β-hmx as functions of pressure and temperature from molecular dynamics", Crystals **10**, 1123 (2020).

[22] P. C. Myint and A. L. Nichols III, "Thermodynamics of hmx polymorphs and hmx/rdx mixtures", Industrial & Engineering Chemistry Research **56**, 387–403 (2017).

[23] E. A. Zhurova, V. V. Zhurov, and A. A. Pinkerton, "Structure and bonding in β-hmx-characterization of a trans-annular n n interaction", Journal of the American Chemical Society **129**, 13887–13893 (2007).

[24] T. D. Sewell, R. Menikoff, D. Bedrov, and G. D. Smith, “A molecular dynamics simulation study of elastic properties of hmx”, The Journal of chemical physics **119**, 7417–7426 (2003).

[25] P. Soni, C. Sarkar, R. Tewari, and T. Sharma, “Hmx polymorphs: gamma to beta phase transformation”, Journal of Energetic Materials **29**, 261–279 (2011).

[26] J. M. Zaug, R. A. Austin, M. R. Armstrong, J. C. Crowhurst, N. Goldman, L. Ferranti, C. K. Saw, R. A. Swan, R. Gross, and L. E. Fried, “Ultrafast dynamic response of single-crystal β-hmx (octahydro-1, 3, 5, 7-tetranitro-1, 3, 5, 7-tetrazocine)”, Journal of Applied Physics **123**, 205902 (2018).

[27] G.-F. Ji, H.-M. Xiao, and H.-S. Dong, “High level calculations on structure and properties of crystalline beta-hmx”, ACTA CHIMICA SINICA-CHINESE EDITION- **60**, 194–199 (2002).

[28] A. Pereverzev and T. Sewell, “Thermal conductivity of β-hmx from equilibrium molecular dynamics simulations”, arXiv preprint arXiv:2110.08914 (2021).

[29] J. D. Quansah, X. Zhang, Q. Wasiullah, and Q. Yan, “Mechanical and thermophysical properties of energetic crystals: evaluation methods and recent achievements”, FirePhysChem (2022).

[30] B. P. Johnson, X. Zhou, H. Ihara, and D. D. Dlott, “Observing hot spot formation in individual explosive crystals under shock compression”, The Journal of Physical Chemistry A **124**, 4646–4653 (2020).

[31] N. Bourne, “On the laser ignition and initiation of explosives”, Proceedings of the Royal Society of London. Series A: Mathematical, Physical and Engineering Sciences **457**, 1401–1426 (2001).

[32] D. D. Dlott, “New developments in the physical chemistry of shock compression”, Annual review of physical chemistry **62**, 575–597 (2011).

[33] M. A. Price, “A study of shock initiation experiments for the explosive pbx 9502 using three reactive burn models”, in Aip conference proceedings, Vol. 2272, 1 (AIP Publishing LLC, 2020), p. 070039.

[34] W. P. Bassett, B. P. Johnson, N. K. Neelakantan, K. S. Suslick, and D. D. Dlott, “Shock initiation of explosives: high temperature hot spots explained”, Applied Physics Letters **111**, 061902 (2017).

[35] Y. Wei, C. Miller, D. Olsen, and M. Zhou, “Prediction of probabilistic shock initiation thresholds of energetic materials through evolution of thermal-mechanical dissipation and reactive heating”, Journal of Applied Mechanics **88** (2021).

[36] A. Pal and C. R. Picu, “Non-schmid effect of pressure on plastic deformation in molecular crystal hmx”, Journal of Applied Physics **125**, 215111 (2019).

[37] Y. Liu, Z. Duan, Z. Zhang, Z. Ou, and F. Huang, “A mesoscopic reaction rate model for shock initiation of multi-component pbx explosives”, Journal of Hazardous Materials **317**, 44–51 (2016).

[38] D. Bedrov, G. D. Smith, and T. D. Sewell, “Thermal conductivity of liquid octahydro-1, 3, 5, 7-tetranitro-1, 3, 5, 7-tetrazocine (hmx) from molecular dynamics simulations”, Chemical Physics Letters **324**, 64–68 (2000).

[39] I. B. Zeldovich, Y. P. Raizer, and W. D. Hayes, *Physics of shock waves and high-temperature hydrodynamic phenomena*, Vol. 1 (Academic Press New York, 1966).

[40] D. J. Benson, “Computational methods in lagrangian and eulerian hydrocodes”, Computer methods in Applied mechanics and Engineering **99**, 235–394 (1992).

[41] W. F. Van Gunsteren and H. J. Berendsen, “Computer simulation of molecular dynamics: methodology, applications, and perspectives in chemistry”, Angewandte Chemie International Edition in English **29**, 992–1023 (1990).

[42] K. Binder, J. Horbach, W. Kob, W. Paul, and F. Varnik, “Molecular dynamics simulations”, Journal of Physics: Condensed Matter **16**, S429 (2004).

[43] M. González, “Force fields and molecular dynamics simulations”, École thématique de la Société Française de la Neutronique **12**, 169–200 (2011).

[44] G. D. Smith and R. K. Bharadwaj, “Quantum chemistry based force field for simulations of hmx”, The Journal of Physical Chemistry B **103**, 3570–3575 (1999).

[45] D. Bedrov, C. Ayyagari, G. D. Smith, T. D. Sewell, R. Menikoff, and J. M. Zaug, “Molecular dynamics simulations of hmx crystal polymorphs using a flexible molecule force field”, Journal of Computer-Aided Materials Design **8**, 77–85 (2001).

[46] N. Mathew and T. Sewell, “Pressure-dependent elastic coefficients of β-hmx from molecular simulations”, Propellants, Explosives, Pyrotechnics **43**, 223–227 (2018).

[47] D. Bedrov, G. D. Smith, and T. D. Sewell, “Temperature-dependent shear viscosity coefficient of octahydro-1, 3, 5, 7-tetranitro-1, 3, 5, 7-tetrazocine (hmx): a molecular dynamics simulation study”, The Journal of chemical physics **112**, 7203–7208 (2000).

[48] M. P. Kroonblawd, N. Mathew, S. Jiang, and T. D. Sewell, “A generalized crystal-cutting method for modeling arbitrarily oriented crystals in 3d periodic simulation cells with applications to crystal–crystal interfaces”, Computer Physics Communications **207**, 232–242 (2016).

[49]R. Chitsazi, M. P. Kroonblawd, A. Pereverzev, and T. Sewell, “A molecular dynamics simulation study of thermal conductivity anisotropy in β-octahydro-1, 3, 5, 7-tetranitro-1, 3, 5, 7-tetrazocine (β-hmx)”, Modelling and Simulation in Materials Science and Engineering **28**, 025008 (2020).

[50]P. Zhao, S. Lee, T. Sewell, and H. Udaykumar, “Tandem molecular dynamics and continuum studies of shock-induced pore collapse in tatb”, Propellants, Explosives, Pyrotechnics **45**, 196–222 (2020).

[51]R. Hockney and J. Eastwood, “Computer simulations using particles (bristol: adam hilger)”, (1988).

[52]S. Gill, “A process for the step-by-step integration of differential equations in an automatic digital computing machine”, in Mathematical proceedings of the cambridge philosophical society, Vol. 47, 1 (Cambridge University Press, 1951), pp. 96–108.

[53]L. Verlet, “Computer” experiments” on classical fluids. i. thermodynamical properties of lennard-jones molecules”, Physical review **159**, 98 (1967).

[54]W. C. Swope, H. C. Andersen, P. H. Berens, and K. R. Wilson, “A computer simulation method for the calculation of equilibrium constants for the formation of physical clusters of molecules: application to small water clusters”, The Journal of chemical physics **76**, 637–649 (1982).

[55]S. Plimpton, “Fast parallel algorithms for short-range molecular dynamics”, Journal of computational physics **117**, 1–19 (1995).

[56]A. Stukowski, “Visualization and analysis of atomistic simulation data with ovito–the open visualization tool”, Modelling and simulation in materials science and engineering **18**, 015012 (2009).

[57]B. Olinger, B. Roof, and H. Cady, “The linear and volume compression of β-hmx and rdx actes du symp”, Int. sur le Comportement des Milieux Denses Sous Hautes Pressions Dynamiques, 3–8 (1978).

[58]J. C. Gump and S. M. Peiris, “Isothermal equations of state of beta octahydro-1, 3, 5, 7-tetranitro-1, 3, 5, 7-tetrazocine at high temperatures”, Journal of applied physics **97**, 053513 (2005).

[59]M. Budzevich, A. Landerville, M. Conroy, Y. Lin, I. Oleynik, and C. White, “Hydrostatic and uniaxial compression studies of 1, 3, 5-triamino-2, 4, 6-trinitrobenzene using density functional theory with van der waals correction”, Journal of Applied Physics **107**, 113524 (2010).

[60] N. Mathew, M. P. Kroonblawd, T. Sewell, and D. L. Thompson, "Predicted melt curve and liquid-state transport properties of tatb from molecular dynamics simulations", Molecular Simulation **44**, 613–622 (2018).

[61] B. A. Steele, S. M. Clarke, M. P. Kroonblawd, I.-F. W. Kuo, P. F. Pagoria, S. N. Tkachev, J. S. Smith, S. Bastea, L. E. Fried, J. M. Zaug, et al., "Pressure-induced phase transition in 1, 3, 5-triamino-2, 4, 6-trinitrobenzene (tatb)", Applied Physics Letters **114**, 191901 (2019).

[62] B. A. Steele, E. Stavrou, V. B. Prakapenka, M. P. Kroonblawd, and I.-F. W. Kuo, "High-pressure equation of state of 1, 3, 5-triamino-2, 4, 6-trinitrobenzene: insights into the monoclinic phase transition, hydrogen bonding, and anharmonicity", The Journal of Physical Chemistry A **124**, 10580–10591 (2020).

[63] M. P. Kroonblawd and R. A. Austin, "Sensitivity of pore collapse heating to the melting temperature and shear viscosity of hmx", Mechanics of Materials **152**, 103644 (2021).

[64] R. Perriot and M. J. Cawkwell, "Thermal conductivity tensor of β-1, 3, 5, 7-tetranitro-1, 3, 5, 7-tetrazoctane (β-hmx) as a function of pressure and temperature", Journal of Applied Physics **130**, 145106 (2021).

[65] M. P. Kroonblawd and T. D. Sewell, "Theoretical determination of anisotropic thermal conductivity for crystalline 1, 3, 5-triamino-2, 4, 6-trinitrobenzene (tatb)", The Journal of chemical physics **139**, 074503 (2013).

[66] M. P. Kroonblawd and T. D. Sewell, "Theoretical determination of anisotropic thermal conductivity for initially defect-free and defective tatb single crystals", The Journal of Chemical Physics **141**, 184501 (2014).

[67] M. P. Kroonblawd and T. D. Sewell, "Predicted anisotropic thermal conductivity for crystalline 1, 3, 5-triamino-2, 4, 6-trinitobenzene (tatb): temperature and pressure dependence and sensitivity to intramolecular force field terms", Propellants, Explosives, Pyrotechnics **41**, 502–513 (2016).

[68] N. Mathew and T. D. Sewell, "Generalized stacking fault energies in the basal plane of triclinic molecular crystal 1, 3, 5-triamino-2, 4, 6-trinitrobenzene (tatb)", Philosophical Magazine **95**, 424–440 (2015).

[69] N. S. Weingarten and R. C. Sausa, "Nanomechanics of rdx single crystals by force–displacement measurements and molecular dynamics simulations", The Journal of Physical Chemistry A **119**, 9338–9351 (2015).

[70] N. Mathew and T. D. Sewell, "Nanoindentation of the triclinic molecular crystal 1, 3, 5-triamino-2, 4, 6-trinitrobenzene: a molecular dynamics study", The Journal of Physical Chemistry C **120**, 8266–8277 (2016).

[71] P. Lafourcade, C. Denoual, and J.-B. Maillet, "Dislocation core structure at finite temperature inferred by molecular dynamics simulations for 1, 3, 5-triamino-2, 4, 6-trinitrobenzene single crystal", The Journal of Physical Chemistry C **121**, 7442–7449 (2017).

[72] P. Lafourcade, C. Denoual, and J.-B. Maillet, "Irreversible deformation mechanisms for 1, 3, 5-triamino-2, 4, 6-trinitrobenzene single crystal through molecular dynamics simulations", The Journal of Physical Chemistry C **122**, 14954–14964 (2018).

[73] M. Khan, A. Pal, and C. R. Picu, "Dislocation mobility and critical stresses at finite temperatures in molecular crystal cyclotetramethylene tetranitramine (β-hmx)", Modelling and Simulation in Materials Science and Engineering **26**, 085009 (2018).

[74] P. Lafourcade, C. Denoual, and J.-B. Maillet, "Mesoscopic constitutive law with nonlinear elasticity and phase transformation for the twinning-buckling of tatb under dynamic loading", Physical Review Materials **3**, 053610 (2019).

[75] M. Khan and C. R. Picu, "Dislocation cross slip in molecular crystal cyclotetramethylene tetranitramine (β-hmx)", Journal of Applied Physics **126**, 155105 (2019).

[76] M. Khan and C. R. Picu, "Shear localization in molecular crystal cyclotetramethylene-tetranitramine (β-hmx): constitutive behavior of the shear band", Journal of Applied Physics **128**, 105902 (2020).

[77] M. Khan and C. R. Picu, "Dislocation energy and line tension in molecular crystal cyclotetramethylene tetranitramine (β-hmx)", Journal of Applied Physics **127**, 055108 (2020).

[78] L. Zhang, S. V. Zybin, A. C. Van Duin, S. Dasgupta, W. A. Goddard III, and E. M. Kober, "Carbon cluster formation during thermal decomposition of octahydro-1, 3, 5, 7-tetranitro-1, 3, 5, 7-tetrazocine and 1, 3, 5-triamino-2, 4, 6-trinitrobenzene high explosives from reaxff reactive molecular dynamics simulations", The Journal of Physical Chemistry A **113**, 10619–10640 (2009).

[79] M. R. Manaa, E. J. Reed, L. E. Fried, and N. Goldman, "Nitrogen-rich heterocycles as reactivity retardants in shocked insensitive explosives", Journal of the American Chemical Society **131**, 5483–5487 (2009).

[80] M. A. Wood, D. E. Kittell, C. D. Yarrington, and A. P. Thompson, "Multiscale modeling of shock wave localization in porous energetic material", Physical Review B **97**, 014109 (2018).

[81] M. N. Sakano, A. Hamed, E. M. Kober, N. Grilli, B. W. Hamilton, M. M. Islam, M. Koslowski, and A. Strachan, "Unsupervised learning-based multiscale model of thermochemistry in 1, 3, 5-trinitro-1, 3, 5-triazinane (rdx)", The Journal of Physical Chemistry A **124**, 9141–9155 (2020).

[82] B. W. Hamilton, B. A. Steele, M. N. Sakano, M. P. Kroonblawd, I.-F. W. Kuo, and A. Strachan, "Predicted reaction mechanisms, product speciation, kinetics, and detonation properties of the insensitive explosive 2, 6-diamino-3, 5-dinitropyrazine-1-oxide (llm-105)", The Journal of Physical Chemistry A **125**, 1766–1777 (2021).

[83] J. Brahmbhatt, X. Bidault, and S. Chaudhuri, "Quantifying surface free energy of molecular crystal β-hmx using non-equilibrium molecular dynamics methods", Journal of Applied Physics **130**, 135105 (2021).

[84] P. Das, P. Zhao, D. Perera, T. Sewell, and H. Udaykumar, "Molecular dynamics-guided material model for the simulation of shock-induced pore collapse in β-octahydro-1, 3, 5, 7-tetranitro-1, 3, 5, 7-tetrazocine (β-hmx)", Journal of Applied Physics **130**, 085901 (2021).

[85] M. P. Kroonblawd, B. A. Steele, M. D. Nelms, L. E. Fried, and R. A. Austin, "Anisotropic strength behavior of single-crystal tatb", Modelling and Simulation in Materials Science and Engineering **30**, 014004 (2021).

[86] J. E. Reaugh, *Grain-scale dynamics in explosives*, tech. rep. (Lawrence Livermore National Lab., CA (US), 2002).

[87] M. Cawkwell, T. D. Sewell, L. Zheng, and D. L. Thompson, "Shock-induced shear bands in an energetic molecular crystal: application of shock-front absorbing boundary conditions to molecular dynamics simulations", Physical Review B **78**, 014107 (2008).

[88] M. Cawkwell, K. Ramos, D. Hooks, and T. D. Sewell, "Homogeneous dislocation nucleation in cyclotrimethylene trinitramine under shock loading", Journal of Applied Physics **107**, 063512 (2010).

[89] E. J. Reed, L. E. Fried, and J. Joannopoulos, "A method for tractable dynamical studies of single and double shock compression", Physical review letters **90**, 235503 (2003).

[90] M. P. Kroonblawd and L. E. Fried, "High explosive ignition through chemically activated nanoscale shear bands", Physical Review Letters **124**, 206002 (2020).

[91] M. P. Kroonblawd, T. D. Sewell, and J.-B. Maillet, “Characteristics of energy exchange between inter-and intramolecular degrees of freedom in crystalline 1, 3, 5-triamino-2, 4, 6-trinitrobenzene (tatb) with implications for coarse-grained simulations of shock waves in polyatomic molecular crystals”, The Journal of Chemical Physics **144**, 064501 (2016).

[92] R. M. Eason and T. D. Sewell, “Shock-induced inelastic deformation in oriented crystalline pentaerythritol tetranitrate”, The Journal of Physical Chemistry C **116**, 2226–2239 (2012).

[93] R. M. Eason and T. D. Sewell, “Molecular dynamics simulations of the collapse of a cylindrical pore in the energetic material α-rdx”, Journal of Dynamic Behavior of Materials **1**, 423–438 (2015).

[94] M. P. Kroonblawd and T. D. Sewell, “Anisotropic relaxation of idealized hot spots in crystalline 1, 3, 5-triamino-2, 4, 6-trinitrobenzene (tatb)”, The Journal of Physical Chemistry C **120**, 17214–17223 (2016).

[95] N. N. Vlassis, P. Zhao, R. Ma, T. Sewell, and W. Sun, “Md-inferred neural network monoclinic finite-strain hyperelasticity models for \beta$-hmx : sobolevtrainingandvalidationagainstphysicalconstraints$”, arXiv preprint arXiv:2112.02077 (2021).

[96] M. P. Kroonblawd, B. W. Hamilton, and A. Strachan, “Fourier-like thermal relaxation of nanoscale explosive hot spots”, The Journal of Physical Chemistry C **125**, 20570–20582 (2021).

[97] A. Pereverzev and T. D. Sewell, “Terahertz normal mode relaxation in pentaerythritol tetranitrate”, The Journal of chemical physics **134**, 014513 (2011).

[98] A. Pereverzev and T. D. Sewell, “A theoretical study of the relaxation of a phenyl group chemisorbed to an rdx freestanding thin film”, The Journal of Chemical Physics **145**, 054503 (2016).

[99] G. Kumar, F. G. VanGessel, L. B. Munday, and P. W. Chung, “3-phonon scattering pathways for vibrational energy transfer in crystalline rdx”, The Journal of Physical Chemistry A **125**, 7723–7734 (2021).

[100] D. E. Hooks, K. J. Ramos, and A. R. Martinez, “Elastic-plastic shock wave profiles in oriented single crystals of cyclotrimethylene trinitramine (rdx) at 2.25 gpa”, Journal of applied physics **100**, 024908 (2006).

[101] L. He, T. D. Sewell, and D. L. Thompson, “Molecular dynamics simulations of shock waves in oriented nitromethane single crystals”, The Journal of chemical physics **134**, 124506 (2011).

[102] L. He, T. D. Sewell, and D. L. Thompson, “Molecular dynamics simulations of shock waves in oriented nitromethane single crystals: plane-specific effects”, The Journal of Chemical Physics **136**, 034501 (2012).

[103] R. Dawes, A. Siavosh-Haghighi, T. D. Sewell, and D. L. Thompson, “Shock-induced melting of (100)-oriented nitromethane: energy partitioning and vibrational mode heating”, The Journal of chemical physics **131**, 224513 (2009).

[104] P. Zhao, M. P. Kroonblawd, N. Mathew, and T. Sewell, “Strongly anisotropic thermomechanical response to shock wave loading in oriented samples of the triclinic molecular crystal 1, 3, 5-triamino-2, 4, 6-trinitrobenzene”, The Journal of Physical Chemistry C **125**, 22747–22765 (2021).

[105] Y. Long, Y. Liu, F. Nie, and J. Chen, “Theoretical study of impacting and desensitizing for hmx–graphite mixture explosive”, Shock Waves **22**, 605–614 (2012).

[106] Y. Long and J. Chen, “A molecular dynamics study of the early-time mechanical heating in shock-loaded octahydro-1, 3, 5, 7-tetranitro-1, 3, 5, 7-tetrazocine-based explosives”, Journal of Applied Physics **116**, 033516 (2014).

[107] S. Jiang, T. D. Sewell, and D. L. Thompson, “Molecular dynamics simulations of shock wave propagation through the crystal–melt interface of (100)-oriented nitromethane”, The Journal of Physical Chemistry C **120**, 22989–23000 (2016).

[108] C. Li, M. N. Sakano, and A. Strachan, “Shock-induced hotspot formation in amorphous and crystalline 1, 3, 5, 7-tetranitro-1, 3, 5, 7-tetrazoctane (hmx): a molecular dynamics comparative study”, Journal of Applied Physics **130**, 055902 (2021).

[109] E. Jaramillo, T. D. Sewell, and A. Strachan, “Atomic-level view of inelastic deformation in a shock loaded molecular crystal”, Physical Review B **76**, 064112 (2007).

[110] X. Bidault and N. Pineau, “Granularity impact on hotspot formation and local chemistry in shocked nanostructured rdx”, The Journal of Chemical Physics **149**, 224703 (2018).

[111] M. D. Nelms, M. P. Kroonblawd, and R. A. Austin, “Pore collapse in single-crystal tatb under shock compression”, in Aip conference proceedings, Vol. 2272, 1 (AIP Publishing LLC, 2020), p. 050001.

[112] M. P. Kroonblawd and N. Goldman, “Mechanochemical formation of heterogeneous diamond structures during rapid uniaxial compression in graphite”, Physical Review B **97**, 184106 (2018).

[113] R. Perriot, C. F. Negre, S. D. McGrane, and M. J. Cawkwell, “Density functional tight binding calculations for the simulation of shocked nitromethane with latte-lammps”, in Aip conference proceedings, Vol. 1979, 1 (AIP Publishing LLC, 2018), p. 050014.

[114] A. Pal and C. R. Picu, “Peierls–nabarro stresses of dislocations in monoclinic cyclotetramethylene tetranitramine (β-hmx)”, Modelling and Simulation in Materials Science and Engineering **26**, 045005 (2018).

[115] A. P. Thompson, H. M. Aktulga, R. Berger, D. S. Bolintineanu, W. M. Brown, P. S. Crozier, P. J. in’t Veld, A. Kohlmeyer, S. G. Moore, T. D. Nguyen, et al., “Lammps-a flexible simulation tool for particle-based materials modeling at the atomic, meso, and continuum scales”, Computer Physics Communications **271**, 108171 (2022).

[116] S. Nosé, “A unified formulation of the constant temperature molecular dynamics methods”, The Journal of chemical physics **81**, 511–519 (1984).

[117] W. G. Hoover, “Canonical dynamics: equilibrium phase-space distributions”, Physical review A **31**, 1695 (1985).

[118] P. Zhao, D. Perera, and T. Sewell, “Molecular dynamics predictions of shock-induced pore collapse in (010)-oriented β-hmx: effects of sample thickness and transverse orientation, and run-to-run variability among statistically equivalent samples”, Propellants, Explosives, Pyrotechnics, e202200030 (2022).

[119] Y. T. Nguyen, D. Perera, P. Zhao, T. Sewell, and H. Udaykumar, “Head-to-head comparison of molecular and continuum simulations of shock-induced collapse of an elongated pore in an energetic molecular crystal”, Propellants, Explosives, Pyrotechnics, e202200016 (2022).

[120] T. D. Sewell and R. Menikoff, “Complete equation of state for β-hmx and implications for initiation”, in Aip conference proceedings, Vol. 706, 1 (American Institute of Physics, 2004), pp. 157–162.

[121] H. K. Springer, S. Bastea, A. L. Nichols III, C. M. Tarver, and J. E. Reaugh, “Modeling the effects of shock pressure and pore morphology on hot spot mechanisms in hmx”, Propellants, Explosives, Pyrotechnics **43**, 805–817 (2018).

[122] J. E. Field, N. Bourne, S. Palmer, and S. Walley, “Hot-spot ignition mechanisms for explosives and propellants”, Philosophical Transactions of the Royal Society of London. Series A: Physical and Engineering Sciences **339**, 269–283 (1992).

[123] R. Menikoff, “Pore collapse and hot spots in hmx”, in Aip conference proceedings, Vol. 706, 1 (American Institute of Physics, 2004), pp. 393–396.

[124] A. Nichols III and C. Tarver, *Twelfth international symposium on detonation*, 2002.

[125] H. Udaykumar, O. Sen, S. Lee, and N. K. Rai, “Unified approach for meso-informed burn models in shocked energetic materials”, Journal of propulsion and power **36**, 655–667 (2020).

[126] N. K. Rai and H. Udaykumar, “Three-dimensional simulations of void collapse in energetic materials”, Physical Review Fluids **3**, 033201 (2018).

[127] T. L. Jackson and J. Zhang, “Density-based kinetics for mesoscale simulations of detonation initiation in energetic materials”, Combustion Theory and Modelling **21**, 749–769 (2017).

[128] W. L. Perry, B. Clements, X. Ma, and J. T. Mang, “Relating microstructure, temperature, and chemistry to explosive ignition and shock sensitivity”, Combustion and flame **190**, 171–176 (2018).

[129] T. L. Jackson, J. D. Buckmaster, J. Zhang, and M. J. Anderson, “Pore collapse in an energetic material from the micro-scale to the macro-scale”, Combustion Theory and Modelling **19**, 347–381 (2015).

[130] H. Springer, C. Tarver, and S. Bastea, “Effects of high shock pressures and pore morphology on hot spot mechanisms in hmx”, in Aip conference proceedings, Vol. 1793, 1 (AIP Publishing LLC, 2017), p. 080002.

[131] S. Roy, N. Rai, O. Sen, D. Hardin, A. Diggs, and H. Udaykumar, “Modeling mesoscale energy localization in shocked hmx, part ii: training machine-learned surrogate models for void shape and void–void interaction effects”, Shock Waves **30**, 349–371 (2020).

[132] N. Rai and H. Udaykumar, “Void collapse generated meso-scale energy localization in shocked energetic materials: non-dimensional parameters, regimes, and criticality of hotspots”, Physics of Fluids **31**, 016103 (2019).

[133] P. W. Cooper and S. R. Kurowski, *Introduction to the technology of explosives* (John Wiley & Sons, 1997).

[134] H. H. Cady, *Studies on the polymorphs of hmx*, Vol. 2652 (Los Alamos Scientific Laboratory of the University of California, 1962).

[135] J. Akhavan, *The chemistry of explosives 4e* (Royal Society of Chemistry, 2022).

[136] J. F. Baytos, *Lasl explosive property data*, Vol. 4 (Univ of California Press, 1980).

[137] S. Palmer and J. Field, “The deformation and fracture of β-hmx”, Proceedings of the Royal Society of London. A. Mathematical and Physical Sciences **383**, 399–407 (1982).

[138] M. Donna, “Hanson-parr & tmothy, p”, Parr. Thermal properties measurements of solid rocket propellants oxidizers and binder materials as a function of temperature.. I Energetic Mater **17**, 1–47 (1999).

[139] C.-S. Yoo and H. Cynn, “Equation of state, phase transition, decomposition of β-hmx (octahydro-1, 3, 5, 7-tetranitro-1, 3, 5, 7-tetrazocine) at high pressures”, The Journal of Chemical Physics **111**, 10229–10235 (1999).

[140] H. Dong, R. Hu, P. Yao, and X. Zhang, “Thermograms of energetic materials”, National Defense Industry Press, Beijing, 276 (2002).

[141] N. D. Parab, Z. A. Roberts, M. H. Harr, J. O. Mares, A. D. Casey, I. E. Gunduz, M. Hudspeth, B. Claus, T. Sun, K. Fezzaa, et al., “High speed x-ray phase contrast imaging of energetic composites under dynamic compression”, Applied Physics Letters **109**, 131903 (2016).

[142] B. M. Dobratz, *Properties of chemical explosives and explosive simulants*, tech. rep. (comp. and ed.; California Univ., Livermore (USA). Lawrence Livermore Lab., 1972).

[143] K. Lynch, A. Thompson, and A. Strachan, “Coarse grain modeling of spall failure in molecular crystals: role of intra-molecular degrees of freedom”, Modelling and Simulation in Materials Science and Engineering **17**, 015007 (2008).

[144] T. D. Sewell, “Monte carlo calculations of the hydrostatic compression of hexahydro-1, 3, 5-trinitro-1, 3, 5-triazine and β-octahydro-1, 3, 5, 7-tetranitro-1, 3, 5, 7-tetrazocine”, Journal of applied physics **83**, 4142–4145 (1998).

[145] J. Chen, Y. Long, Y. Liu, F. Nie, and J. Sun, “The first-principle study on the equation of state of hmx under high pressure”, Science China Physics, Mechanics and Astronomy **54**, 831–835 (2011).

[146] H.-L. Cui, G.-F. Ji, J.-J. Zhao, F. Zhao, X.-R. Chen, Q.-M. Zhang, and D.-Q. Wei, “Ab initio and molecular dynamics studies of solid β-hmx: effects of hydrostatic pressure and high temperature”, Molecular Simulation **36**, 670–681 (2010).

[147] J. J. Xiao, W. R. Wang, J. Chen, G. F. Ji, W. Zhu, and H. M. Xiao, “Study on structure, sensitivity and mechanical properties of hmx and hmx-based pbxs with molecular dynamics simulation”, Computational and Theoretical Chemistry **999**, 21–27 (2012).

[148] T. Zhou, S. V. Zybin, Y. Liu, F. Huang, and W. A. Goddard III, "Anisotropic shock sensitivity for β-octahydro-1, 3, 5, 7-tetranitro-1, 3, 5, 7-tetrazocine energetic material under compressive-shear loading from reaxff-lg reactive dynamics simulations", Journal of Applied Physics **111**, 124904 (2012).

[149] Y. Long and J. Chen, "Systematic study of the reaction kinetics for hmx", The Journal of Physical Chemistry A **119**, 4073–4082 (2015).

[150] S. Jiang, J. Tao, T. D. Sewell, and Z. Chen, "Hierarchical multiscale simulations of crystalline β-octahydro-1, 3, 5, 7-tetranitro-1, 3, 5, 7-tetrazocine (β-hmx): generalized interpolation material point method simulations of brittle fracture using an elastodamage model derived from molecular dynamics", International Journal of Damage Mechanics **26**, 293–313 (2017).

[151] B. Tanasoiu and M. Koslowski, "A parametric study of the dynamic failure of energetic composites", Journal of Applied Physics **122**, 125103 (2017).

[152] L. Tran and H. Udaykumar, "Simulation of void collapse in an energetic material, part i: inert case", Journal of propulsion and power **22**, 947–958 (2006).

[153] R. Menikoff and T. Sewell, *Combust. theory modell*, 2002.

[154] J. J. Dick, A. R. Martinez, and R. S. Hixson, *Plane impact response of pbx 9501 and its components below 2 gpa*, tech. rep. (Los Alamos National Lab.(LANL), Los Alamos, NM (United States), 1998).

[155] K. Kline, Y. Horie, J. Dick, and W. Wang, "Impact response of pbx 9501 below 2 gpa", in Aip conference proceedings, Vol. 620, 1 (American Institute of Physics, 2002), pp. 411–414.

[156] R. A. Austin, N. R. Barton, J. E. Reaugh, and L. E. Fried, "Direct numerical simulation of shear localization and decomposition reactions in shock-loaded hmx crystal", Journal of Applied Physics **117**, 185902 (2015).

[157] R. Austin, N. Barton, W. Howard, and L. Fried, "Modeling pore collapse and chemical reactions in shock-loaded hmx crystals", in Journal of physics: conference series, Vol. 500, 5 (IOP Publishing, 2014), p. 052002.

[158] A. Nassar, N. K. Rai, O. Sen, and H. Udaykumar, "Modeling mesoscale energy localization in shocked hmx, part i: machine-learned surrogate models for the effects of loading and void sizes", Shock Waves **29**, 537–558 (2019).

[159] A. Kapahi, J. Mousel, S. Sambasivan, and H. Udaykumar, "Parallel, sharp interface eulerian approach to high-speed multi-material flows", Computers & Fluids **83**, 144–156 (2013).

[160] S. Nemat-Nasser, *Plasticity: a treatise on finite deformation of heterogeneous inelastic materials* (Cambridge University Press, 2004).

[161] A. Dhiman, A. Olokun, and V. Tomar, "Microscale analysis of stress wave propagation through plastic bonded explosives under micro-sphere shock impact", Journal of Dynamic Behavior of Materials **7**, 294–306 (2021).

[162] R. Hu, C. Prakash, V. Tomar, M. Harr, I. E. Gunduz, and C. Oskay, "Experimentally-validated mesoscale modeling of the coupled mechanical–thermal response of ap–htpb energetic material under dynamic loading", International Journal of Fracture **203**, 277–298 (2017).

[163] J. Kimberley, L. Lamberson, and S. Mates, *Dynamic behavior of materials, volume* (Springer, 2018).

[164] W. P. Bassett and D. D. Dlott, "Shock initiation of explosives: temperature spikes and growth spurts", Applied Physics Letters **109**, 091903 (2016).

[165] D. D. Dlott, "Shock compression dynamics under a microscope", in Aip conference proceedings, Vol. 1793, 1 (AIP Publishing LLC, 2017), p. 020001.

[166] A. Olokun, B. Li, C. Prakash, Z. Men, D. D. Dlott, and V. Tomar, "Examination of local microscale-microsecond temperature rise in hmx-htpb energetic material under impact loading", JOM **71**, 3531–3535 (2019).

[167] N. K. Rai, E. M. Escauriza, D. E. Eakins, and H. Udaykumar, "Mechanics of shock induced pore collapse in poly (methyl methacrylate)(pmma): comparison of simulations and experiments", Journal of the Mechanics and Physics of Solids **143**, 104075 (2020).

[168] M. Cawkwell and V. Manner, "Ranking the drop-weight impact sensitivity of common explosives using arrhenius chemical rates computed from quantum molecular dynamics simulations", The Journal of Physical Chemistry A **124**, 74–81 (2019).

[169] S. Sambasivan, A. Kapahi, and H. Udaykumar, "Simulation of high speed impact, penetration and fragmentation problems on locally refined cartesian grids", Journal of Computational Physics **235**, 334–370 (2013).

[170] P. Das, N. K. Rai, and H. Udaykumar, "A levelset-based sharp-interface modified ghost fluid method for high-speed multiphase flows and multi-material hypervelocity impact", Immersed Boundary Method: Development and Applications, 187–226 (2020).

[171] A. Kapahi, S. Sambasivan, and H. Udaykumar, "A three-dimensional sharp interface cartesian grid method for solving high speed multi-material impact, penetration and fragmentation problems", Journal of Computational Physics **241**, 308–332 (2013).

[172] J. A. Sethian and P. Smereka, "Level set methods for fluid interfaces", Annual review of fluid mechanics **35**, 341–372 (2003).

[173] F. D. Murnaghan, "The compressibility of media under extreme pressures", Proceedings of the National Academy of Sciences **30**, 244–247 (1944).

[174] L. L. Stevens, N. Velisavljevic, D. E. Hooks, and D. M. Dattelbaum, "Hydrostatic compression curve for triamino-trinitrobenzene determined to 13.0 gpa with powder x-ray diffraction", Propellants, Explosives, Pyrotechnics: An International Journal Dealing with Scientific and Technological Aspects of Energetic Materials **33**, 286–295 (2008).

[175] R. Gustavsen, S. Sheffield, and R. Alcon, "Measurements of shock initiation in the tri-amino-tri-nitro-benzene based explosive pbx 9502: wave forms from embedded gauges and comparison of four different material lots", Journal of applied physics **99**, 114907 (2006).

[176] F. Najjar, W. Howard, and L. Fried, "Grain-scale simulations of hot-spot initiation for shocked tatb", in Aip conference proceedings, Vol. 1195, 1 (American Institute of Physics, 2009), pp. 49–52.

[177] S. K. Sambasivan and H. UdayKumar, "Sharp interface simulations with local mesh refinement for multi-material dynamics in strongly shocked flows", Computers & Fluids **39**, 1456–1479 (2010).

[178] C. S. Desai, *Constitutive laws for engineering materials: theory and applications: proceedings of the second international conference on constitutive laws for engineering materials–theory and applications, held january 5-8, 1987, in tucson, arizona, usa*, Vol. 2 (Elsevier Publishing Company, 1987).

[179] V. Kechin, "Thermodynamically based melting-curve equation", Journal of Physics: Condensed Matter **7**, 531 (1995).

[180] A. Lopato and P. Utkin, "Numerical study of detonation wave propagation in the variable cross-section channel using unstructured computational grids", Journal of Combustion **2018** (2018).

[181] S. Gottlieb and C.-W. Shu, "Total variation diminishing runge-kutta schemes", Mathematics of computation **67**, 73–85 (1998).

[182] R. P. Fedkiw, T. Aslam, B. Merriman, and S. Osher, “A non-oscillatory eulerian approach to interfaces in multimaterial flows (the ghost fluid method)”, Journal of computational physics **152**, 457–492 (1999).

[183] J. W. Eastwood, R. W. Hockney, and D. Lawrence, “P3m3dp—the three-dimensional periodic particle-particle/particle-mesh program”, Computer Physics Communications **19**, 215–261 (1980).

[184] A. Siavosh-Haghighi, R. Dawes, T. D. Sewell, and D. L. Thompson, “Shock-induced melting of (100)-oriented nitromethane: structural relaxation”, The Journal of chemical physics **131**, 064503 (2009).

[185] S. B. s J-F, “Interaction of weak shock waves with cylindrical and spherical gas ingomogeneties”, Journal of Fluid Mechanics **181**, 41–76 (1987).

[186] T. Wright and H. Ockendon, “A scaling law for the effect of inertia on the formation of adiabatic shear bands”, International journal of plasticity **12**, 927–934 (1996).

[187] D. Grady and M. Kipp, “The growth of unstable thermoplastic shear with application to steady-wave shock compression in solids”, Journal of the Mechanics and Physics of Solids **35**, 95–119 (1987).

[188] X. Zhang and C. Oskay, “Plastic dissipation sensitivity to mechanical properties in polycrystalline β-hmx subjected to impact loading”, Mechanics of Materials **138**, 103079 (2019).

[189] R. Menikoff, *Granular explosives and initiation sensitivity*, tech. rep. (Los Alamos National Lab.(LANL), Los Alamos, NM (United States), 1999).

[190] C. Handley, B. Lambourn, N. Whitworth, H. James, and W. Belfield, “Understanding the shock and detonation response of high explosives at the continuum and meso scales”, Applied Physics Reviews **5**, 011303 (2018).

[191] N. Bourne and J. Field, “Shock-induced collapse of single cavities in liquids”, Journal of Fluid Mechanics **244**, 225–240 (1992).

[192] R. B. Frey, *Cavity collapse in energetic materials.* Tech. rep. (ARMY BALLISTIC RESEARCH LAB ABERDEEN PROVING GROUND MD, 1986).

[193] R. Menikoff, “Compaction wave profiles in granular hmx”, in Aip conference proceedings, Vol. 620, 1 (American Institute of Physics, 2002), pp. 979–982.

[194] Y. Partom and E. Hanina, “Calibration of macroscopic impact ignition model from simulation of shear band formation on the mesoscale”, in Aip conference proceedings, Vol. 1979, 1 (AIP Publishing LLC, 2018), p. 150031.

[195] R. B. Frey, *The initiation of explosive charges by rapid shear*, tech. rep. (ARMY BALLISTIC RESEARCH LAB ABERDEEN PROVING GROUND MD, 1980).

[196] F. P. Bowden and O. Gurton, "Initiation of solid explosives by impact and friction: the influence of grit", Proceedings of the Royal Society of London. Series A. Mathematical and Physical Sciences **198**, 337–349 (1949).

[197] G. R. Parker, M. D. Holmes, E. M. Heatwole, R. M. Broilo, M. N. Pederson, and P. M. Dickson, "Direct observation of frictional ignition in dropped hmx-based polymer-bonded explosives", Combustion and Flame **221**, 180–193 (2020).

[198] P. Peterson, G. Avilucea, R. Bishop, and J. Sanchez, "Individual contributions of friction and impact on non-shock initiation of high explosives", in Aip conference proceedings, Vol. 955, 1 (American Institute of Physics, 2007), pp. 983–986.

[199] B. Khasainov, A. Borisov, B. Ermolaev, and A. Korotkov, "Two-phase visco-plastic model of shock initiation of detonation in high density pressed explosives", in Proc. seventh symp. on detonation (1982), pp. 435–447.

[200] E. Matheson, D. Drumheller, and M. Baer, "An internal damage model for viscoelastic-viscoplastic energetic materials", in Aip conference proceedings, Vol. 505, 1 (American Institute of Physics, 2000), pp. 691–694.

[201] R. Winter and J. E. Field, "The role of localized plastic flow in the impact initiation of explosives", Proceedings of the Royal Society of London. A. Mathematical and Physical Sciences **343**, 399–413 (1975).

[202] N. K. Rai, M. J. Schmidt, and H. Udaykumar, "Collapse of elongated voids in porous energetic materials: effects of void orientation and aspect ratio on initiation", Physical review fluids **2**, 043201 (2017).

[203] G. A. Levesque and P. Vitello, "The effect of pore morphology on hot spot temperature", Propellants, Explosives, Pyrotechnics **40**, 303–308 (2015).

[204] A. Kapila, D. Schwendeman, J. Gambino, and W. Henshaw, "A numerical study of the dynamics of detonation initiated by cavity collapse", Shock Waves **25**, 545–572 (2015).

[205] S. Roy, O. Sen, N. Rai, M. Moon, E. Welle, C. Molek, K. Choi, and H. Udaykumar, "Structure–property–performance linkages for heterogenous energetic materials through multi-scale modeling", Multiscale and Multidisciplinary Modeling, Experiments and Design **3**, 265–293 (2020).

[206]N. K. Rai and H. Udaykumar, “Mesoscale simulation of reactive pressed energetic materials under shock loading”, Journal of Applied Physics **118**, 245905 (2015).

[207]N. R. Barton, N. W. Winter, and J. E. Reaugh, “Defect evolution and pore collapse in crystalline energetic materials”, Modelling and Simulation in Materials Science and Engineering **17**, 035003 (2009).

[208]F. Addessio, D. Luscher, M. Cawkwell, and K. Ramos, “A single-crystal model for the high-strain rate deformation of cyclotrimethylene trinitramine including phase transformations and plastic slip”, Journal of Applied Physics **121**, 185902 (2017).

[209]D. J. Luscher, F. L. Addessio, M. J. Cawkwell, and K. J. Ramos, “A dislocation density-based continuum model of the anisotropic shock response of single crystal α-cyclotrimethylene trinitramine”, Journal of the Mechanics and Physics of Solids **98**, 63–86 (2017).

[210]H. H. Cady, A. C. Larson, and D. T. Cromer, “The crystal structure of α-hmx and a refinement of the structure of β-hmx”, Acta crystallographica **16**, 617–623 (1963).

[211]N. K. Rai, M. J. Schmidt, and H. Udaykumar, “High-resolution simulations of cylindrical void collapse in energetic materials: effect of primary and secondary collapse on initiation thresholds”, Physical Review Fluids **2**, 043202 (2017).

[212]V. Nesterenko, M. Meyers, and T. Wright, “Self-organization in the initiation of adiabatic shear bands”, Acta materialia **46**, 327–340 (1998).

[213]M. Meyers, Q. Xue, and V. Nesterenko, “Evolution in the patterning of adiabatic shear bands”, in Aip conference proceedings, Vol. 620, 1 (American Institute of Physics, 2002), pp. 567–570.

[214]M. MA, Q. Xue, Y. Xu, and V. Nesterenko, “Microstructural evolution and self-organization of shear bands”, in Impact engineering and application: proceedings of the 4th international symposium on impact engineering, 16-18 july 2001, kumamoto, japan (Elsevier Science, 2001), p. 123.

[215]T. C. Halsey, “Diffusion-limited aggregation: a model for pattern formation”, Physics Today **53**, 36–41 (2000).

[216]I. N. Motoike, “Simple modeling of branching pattern formation in a reaction diffusion system with cellular automaton”, Journal of the Physical Society of Japan **76**, 034002 (2007).

[217]S. K. Sarkar, “Saffman-taylor instability and pattern formation in diffusion-limited aggregation”, Physical Review A **32**, 3114 (1985).